

# Exploring the determinants of chloride homeostasis in neurons using biophysical models



Presented by:  
**Kira M. Düsterwald**  
DSTKIR002

Supervised by:  
**Dr Joseph V. Raimondo**

Submitted to the Department of Human Biology at the Faculty of Health Sciences of the University of Cape Town in fulfilment of the academic requirements for a Masters of Medical Science in Neuroscience (Physiology)

October 20, 2018

# Anti-Plagiarism Declaration

1. I know that plagiarism is wrong. Plagiarism is to use another's work and pretend that it is one's own.
2. I have used the Journal of Physiology convention for citation and referencing. Each contribution to, and quotation in, this report from the work(s) of other people has been attributed, and has been cited and referenced.
3. This report is my own work.
4. I have not allowed, and will not allow, anyone to copy my work with the intention of passing it off as their own work or part thereof.

**October 20, 2018**



Kira Michaela Düsterwald

# Acknowledgements

Completing this thesis has taught me a great deal, not least about the many people who care about my well-being and support me in my endeavours.

That I enrolled for a Masters degree at all is largely because of the work of Arieh Katz in developing clinician-scientists at the University of Cape Town. Congratulations, Professor, on the number of us who you have enabled to pursue interests in the basic sciences.

Alan Kay set off the spark for the main modelling choices. He is always willing to discuss the details of how cells ought to work, the history behind each theory, and the quirks of the important people in the field. Alan, thank you for engaging with us from the very start.

My project has earned the interest and help of my fellow lab members, whose friendly presence in the office is always welcome. Christopher Currin's programming know-how has greatly improved my own coding; he helped with the backbone of the multi-compartment set-up. Richard Burman was responsible for the experiments in the Discussion and conducted the KCC2 meta-analysis with me — his own brand of humour always mixed in.

To the Zinn family and especially to Michael, thank you for providing me with optimum writing conditions over the last few weeks (and especially for the use of the rondavel in the middle of the Limpopo bush!). I am grateful that your embracing of my need to work included the enforcement of much-needed coffee and wildlife breaks.

To Yashodhan, my clinical partner, thank you for putting up with regular changes to our clinical schedule while still listening to me ramble about my thesis (with questions!).

Thank you to all the other friends and colleagues who asked me to explain what I am doing until they understood it, too. Only through turning a project that I began part-time into a proper second degree have I been lucky enough to spend time with my 2017 isiCNI and Mandela Rhodes Foundation peers and mentors. One of the core members of the isiCNI team, Tim Vogels, hosted me in Oxford and encouraged my interest in the field right when I entered into the computational neuroscience world. Thank you, Tim. The scholars from both programmes have inspired me to keep striving, but also to look at the broader perspective of my work in the African context. I am excited to see what the future brings for these communities.

Then to Joe, thank you so much for taking me on as a student in spite of my concurrent commitments and last-minute requests for meetings. I am incredibly grateful to have had a supervisor willing to tell me with great care and detail when I can improve, when I need to do more, and when I am doing well. You continue to make science very exciting.

Finally, to my dad, mom, and brothers — my home base. Dad, thank you for the many car journeys, your practical advice, and for always being ready with a specially-brewed cup of coffee. Mom, you were a fantastic, thorough proofreader, but you also pushed me to finish this thesis when it was time for it to be done. Your enthusiasm, motivation and academic anecdotes were essential to the writing process. Thomas and Carl, you are a great technical team. Thank you, thank you, thank you; love to you all.

# Abstract

Fast synaptic inhibition in the nervous system depends on the transmembrane flux of  $\text{Cl}^-$  ions via activated GABA<sub>A</sub> and glycine receptors. As a result, changes to the neuronal driving force for  $\text{Cl}^-$  are thought to play pivotal roles in many physiological and pathological brain processes. Established theories regarding the determinants of  $\text{Cl}^-$  driving force have recently been questioned based on new experimental data. However, it is experimentally difficult to distinguish the respective contributions of the multiple, dynamically interacting mechanisms which may be important in  $\text{Cl}^-$  homeostasis. Here I present biophysical models of  $\text{Cl}^-$  homeostasis using the pump-leak formulation. By means of numerical and novel analytic solutions, I demonstrate that the  $\text{Na}^+/\text{K}^+$ -ATPase, ion conductances, impermeant anions, electrodiffusion, water fluxes and cation-chloride cotransporters (CCCs) play roles in setting the  $\text{Cl}^-$  driving force. Importantly, I show that while impermeant anions can contribute to setting  $[\text{Cl}^-]_i$  in neurons, they have a negligible effect on the driving force for  $\text{Cl}^-$  locally and cell-wide. In contrast, I demonstrate that CCCs are well-suited for modulating  $\text{Cl}^-$  driving force and hence inhibitory signalling in neurons. This prediction is supported by a meta-analysis of multiple experimental studies, which demonstrates a strong correlation between the expression of the cation-chloride cotransporter KCC2 and intracellular  $\text{Cl}^-$  concentration. My findings reconcile recent experimental findings and provide a framework for understanding the interplay of different chloride regulatory processes in neurons.

# Contents

<b>1</b>	<b>Introduction</b>	<b>1</b>
1.1	Cellular homeostasis and ionic regulation in neurons . . . . .	1
1.1.1	Neural signalling requires ionic flux . . . . .	1
1.1.2	Electrochemical ionic flux and the Nernst potential . . . . .	1
1.1.3	The cellular electric field and membrane potential . . . . .	2
1.1.4	Application of electrochemical equilibria and the ionic driving force .	3
1.1.5	The $\text{Na}^+/\text{K}^+$ -ATPase establishes the cellular membrane potential and volume using the pump-leak mechanism . . . . .	4
1.2	GABA <sub>A</sub> receptors mediate inhibitory signalling via chloride . . . . .	4
1.2.1	The chloride driving force determines GABA <sub>A</sub> neurotransmission .	4
1.2.2	The importance of chloride concentration in GABA <sub>A</sub> receptor signalling	5
1.3	Cation-chloride cotransporters . . . . .	8
1.3.1	Types of cation-chloride cotransporters . . . . .	8
1.3.2	Pharmacological evidence for the role of CCCs in setting the chloride driving force . . . . .	10
1.3.3	Evidence from comparative disease models for the role of CCCs in setting the internal chloride concentration . . . . .	10
1.4	The impermeant anion hypothesis of chloride regulation . . . . .	12
1.4.1	Experimental evidence for the role of impermeant anions in setting the chloride gradient . . . . .	12
1.4.2	Cellular regulation of volume and osmolarity . . . . .	13
1.4.3	Local regulation of chloride concentration . . . . .	15
1.5	Aim and objectives . . . . .	16
1.5.1	Aim . . . . .	16
1.5.2	Objectives . . . . .	16
<b>2</b>	<b>Methods</b>	<b>17</b>
2.1	Single compartment model . . . . .	17
2.1.1	Membrane potential . . . . .	19
2.1.2	$\text{Na}^+/\text{K}^+$ -ATPase . . . . .	19
2.1.3	KCC2 . . . . .	20
2.1.4	Permeable ion concentrations . . . . .	20
2.1.5	Volume . . . . .	22
2.1.6	Anion flux . . . . .	23
2.2	Multi-compartment model . . . . .	23
2.2.1	Electrodiffusion . . . . .	23
2.2.2	GABA <sub>A</sub> receptors . . . . .	24
2.3	Systematic review . . . . .	25

<b>3 Results</b>	<b>27</b>
3.1 A single compartment model using the pump-leak formulation is suitable to test chloride homeostatic mechanisms . . . . .	27
3.1.1 The pump-leak model demonstrates the importance of the $\text{Na}^+/\text{K}^+$ -ATPase in ionic homeostasis . . . . .	28
3.1.2 An analytical solution can evaluate steady state conditions of the pump-leak model . . . . .	31
3.2 Chloride cotransport modulates chloride driving force . . . . .	33
3.2.1 Membrane chloride conductance affects steady-state intracellular chloride concentration only in the presence of active cation-chloride cotransport . . . . .	33
3.2.2 Cation-chloride cotransport sets the chloride reversal and driving force for transmembrane chloride flux . . . . .	35
3.3 Impermeant anions can only drive shifts in chloride driving force when average impermeant anion charge or osmolarity is altered, and even then the shifts are negligible . . . . .	38
3.3.1 Altering the concentration of intracellular or extracellular impermeant anions, without changing the average charge of impermeant anions, does not affect the steady state gradient or driving force for chloride . . . . .	38
3.3.2 Changing the average charge of impermeant anions can drive substantial shifts in the reversal potential for chloride, but has negligible effects on chloride driving force . . . . .	40
3.3.3 Impermeant anions drive small shifts in chloride driving force by modifying the $\text{Na}^+/\text{K}^+$ -ATPase pump rate under conditions of active chloride cotransport . . . . .	44
3.4 A multi-compartment model shows that local differences in chloride driving force can be achieved with cation-chloride cotransport by restricting chloride diffusion, but not with impermeant anions, which cause local swelling . . . . .	48
3.4.1 Changes in cation-chloride cotransport activity generate local differences in chloride reversal and driving force, which depend on cytoplasmic diffusion rates . . . . .	48
3.4.2 Local impermeant anions do not appreciably affect the local driving force for chloride . . . . .	48
3.4.3 Addition of local impermeant anions generates volume changes and can model the growth of neuronal processes . . . . .	51
3.4.4 Local driving force differences modulate the post-synaptic potential when $\text{GABA}_A$ receptors are activated at a synapse . . . . .	53
<b>4 Discussion</b>	<b>55</b>
4.1 My computational models provide novel insights into the relative importance of different cellular mechanisms underlying chloride homeostasis in neurons . . . . .	55
4.2 My model confirms the roles of fundamental cellular mechanisms in chloride homeostasis . . . . .	56
4.2.1 The $\text{Na}^+/\text{K}^+$ -ATPase . . . . .	56
4.2.2 Passive ionic conductances . . . . .	56
4.3 Cation-chloride cotransporters can modulate changes in chloride driving force in my biophysical model . . . . .	58
4.3.1 KCC2 activity modulates chloride driving force specifically, in agreement with experimental evidence . . . . .	58

4.3.2	KCC2 can mediate volume shifts without explicitly cotransporting water . . . . .	58
4.3.3	KCC2 can only modulate local differences in chloride driving force under conditions of constrained electrodiffusion . . . . .	59
4.4	Impermeant anions cannot appreciably modify the chloride driving force . .	59
4.4.1	Even under conditions of osmotic strain, impermeant anion concentration changes do not appreciably modify chloride driving force . .	59
4.4.2	Modification of impermeant anions' average charge can cause shifts in the chloride gradient, but cannot significantly shift the chloride driving force . . . . .	60
4.4.3	Impermeant anion-driven shifts in chloride homeostasis are secondary to alterations to active ionic transport kinetics . . . . .	61
4.4.4	Outlook for future evaluation of impermeant anions' role in chloride homeostasis . . . . .	63
4.5	Conclusion . . . . .	63
	<b>References</b>	<b>64</b>

# List of Figures

1.1	The response of the membrane potential to GABA <sub>AR</sub> activation depends on the intracellular chloride concentration and chloride driving force. . . . .	6
1.2	Important transporters in chloride homeostasis and mechanisms of increasing intracellular chloride concentration. . . . .	9
1.3	Proposition for the central role of impermeant anions in setting the chloride gradient and driving force. . . . .	14
3.1	A biophysical model of ion dynamics based on the pump-leak mechanism demonstrates the importance of the sodium-potassium ATPase for setting transmembrane ion gradients including chloride. . . . .	28
3.2	Membrane chloride conductance affects steady-state intracellular chloride concentration only in the presence of active cation-chloride cotransport. . .	34
3.3	Cation-chloride cotransport sets the chloride reversal and driving force for transmembrane chloride flux. . . . .	36
3.4	Adding intracellular or extracellular impermeant anions, without changing the average charge of impermeant anions, does not affect the steady state gradient or driving force for chloride. . . . .	41
3.5	Adjusting the average charge of impermeant anions shifts the chloride reversal potential with negligible effects on the driving force for chloride. . . . .	42
3.6	Impermeant anions drive small shifts in chloride driving force by modifying the Na <sup>+</sup> /K <sup>+</sup> -ATPase pump rate under conditions of active chloride cotransport.	44
3.7	Alternative ATPase and KCC2 models with different kinetics have similar properties to my model's ATPase when impermeant anions in the cell are changed, and are also dependent on the pump rate. . . . .	47
3.8	Local changes in KCC2 activity generate local differences in chloride reversal and driving force only under conditions of constrained chloride diffusion. .	49
3.9	Local changes in impermeant anions do not establish the local driving force for chloride. . . . .	50
3.10	Addition of impermeant anions could be a mechanism of dendritic growth. .	52
3.11	Local modification of dendritic KCC2 activity and not impermeant anions affects somatic IPSP amplitude in a multi-compartment model employing electrodiffusion. . . . .	54
4.1	Experimental evidence confirms the role of CCCs but not impermeant anions in setting the chloride driving force. . . . .	57
4.2	The respective influences of cation-chloride cotransporters and impermeant anions on chloride homeostasis — three possible cellular arrangements that all result in inhibitory GABA signalling. . . . .	62

# List of Tables

1.1	Changes in the activity of cation-chloride cotransporters in different disease models are associated with changes in intracellular chloride concentration. . . . .	11
2.1	Constants, default parameters and usual steady state values for variables used in the biophysical models. . . . .	18
2.2	Conductance values from computational models of neurons in the literature.	21
2.3	Scoring system used to weight studies for the least squares regression meta-analysis in Figure 3C. . . . .	26
3.1	Data from studies included in the meta-analysis and compared using statistical regression, which show that changes in the activity of KCC2 are associated with changes in Cl <sup>-</sup> driving force and intracellular Cl <sup>-</sup> concentration, but static V <sub>m</sub> . . . . .	39

# List of Abbreviations and Symbols

$A_m$	membrane area scaling parameter — surface area divided by cell volume
$BDNF$	brain-derived neurotrophic factor
$Ca^{2+}$	calcium ion
$CCC$	cation-chloride cotransporter
$ChR2$	channelrhodopsin-2
$Cl^-$	chloride ion
$CO_2$	carbon dioxide
$C_m$	membrane capacitance
$\Delta$	delta, meaning colloquially difference between or change
$DF$	driving force of an ion, that is difference between the membrane potential and the ion's Nernst potential
$\frac{d}{dt}$	derivative over time $t$
$dt$	size of time step in seconds
$D_{ion}$	diffusion constant through aqueous medium
$d_x$	size of (diffusion) distance step
$E_{ion}$	reversal or electrochemical equilibrium potential of an ion
$E_{GABA}$	reversal or electrochemical equilibrium potential through type A $\gamma$ -aminobutyric acid receptors
$F$	the Faraday constant, $96485.3329 \text{ s}\cdot\text{A}\cdot\text{mol}^{-1}$
$g_r$	conductance through receptor $r$ (or of ion $r$ through the membrane)
$GABA_ARs$	type A $\gamma$ -aminobutyric acid receptors
$GAD2+$	glutamate decarboxylase 2
$GHK$	Goldman-Hodgkin-Katz (equation)
$HCO_3^-$	bicarbonate ion
$H_p$	hydrostatic pressure
$H_2O$	water
$I$	current in amperes
$[ion_r]_i$	concentration of ion $r$ in the intracellular compartment
$[ion_r]_o$	concentration of ion $r$ in the extracellular compartment
$IPSP$	inhibitory post-synaptic potential
$J_R$	flux through transporter $R$
$K^+$	potassium ion
$KCC2$	type 2 potassium chloride cotransporter

$k_m$	membrane tension
$l$	length
$\ln$	natural logarithm
$\mu_r$	ion mobility constant for ion $r$
$n$	number of moles $r$
$N_A$	Avogadro's constant for the number of molecules in a mole, $6.02214086 \cdot 10^{23} \text{ mol}^{-1}$
$N_{H_p}/osmo_p$	difference between intracellular and extracellular osmolarity
$Na^+$	sodium ion
$Na^+/K^+$ -ATPase	sodium potassium ATPase pump
$NKCC1$	type 1 sodium potassium chloride cotransporter
$NPE$	Nernst-Planck Equation
$P$	membrane pump rate constant
$P_{mr}$	membrane permeability constant of ion $r$
$\pi$	the constant pi, 3.14159265359
$\Pi_i/\Pi_o$	intracellular/extracellular osmolarity
$p_w$	osmotic permeability of a membrane
$q$	charge in coulombs
$r$	radius
$r_t$	fraction of bound GABA <sub>A</sub> receptors at time $t$ (in relation to a synaptic pulse)
$R$	the gas constant, $8.3144598 \text{ J} \cdot \text{mol}^{-1} \cdot \text{K}^{-1}$
$R_r$	resistance through receptor $r$ (or of ion $r$ through the membrane)
$RT\text{-}PCR$	reverse transcriptase polymerase chain reaction
$SA$	surface area
$t$	time
$T$	temperature in degrees Kelvin (generally room temperature, $298.15 \text{ }^\circ\text{K}$ )
$V_m$	membrane potential (in mV)
$v_w$	partial molar volume of water
$w$	volume
$X^z$	group of impermeant anions with average charge $z$
$z_r$	valence of ion $r$
$Zn^{2+}$	zinc ion



# Chapter 1

## Introduction

### 1.1 Cellular homeostasis and ionic regulation in neurons

#### 1.1.1 Neural signalling requires ionic flux

The fascinating and complex behaviours exhibited by animals are secondary to neural activity based on the passage of information between neurons, or neurotransmission. Neurons in the brain communicate with one another via synaptic signalling, which relies on the activation of receptor proteins that permit rapid transmembrane fluxes of ions carrying charge.

The magnitude and direction of the electrical signals elicited when neurotransmitters bind to receptor molecules and cause ionic flux determines the effect of neurotransmission on the post-synaptic membrane — excitation by increasing (depolarising) the membrane potential or inhibition by decreasing (hyperpolarising) the membrane potential. Changes to the potentials activated via synaptic signalling can have deleterious outcomes in the nervous system, which relies on both inhibition and excitation to bring about its effects. It is therefore important to understand the mechanisms underlying ionic flux and homeostasis in neurons.

#### 1.1.2 Electrochemical ionic flux and the Nernst potential

To investigate what properties underlie ionic steady states, it is necessary to understand the key components that make up a cell. Defined simply, a *cell* is a collection of molecules, ions and substrates in solution surrounded by a selectively-permeable membrane. The membrane ‘barrier’ forms a compartment and separates the cell’s contents from the extracellular fluid environment.

*Diffusion* is the process which describes the net movement of ions or molecules from a region of high concentration to a region of low concentration. If a membrane is permeable to certain ions or molecules, these ions will tend to diffuse across the membrane down concentration gradients. *Osmosis* is the result of the diffusion of solvent molecules

(e.g. water) across a semi-permeable membrane until there is an equal concentration of solutes on either side (*osmoneutrality*). In addition, for a charged molecule on either side of a membrane, electric forces based on surrounding charges create *drift*, flux based on an electrical field (Ohm's law for drift). Therefore ions will also tend to move across the cell membrane according to the electrical potential across it. Ohm's law for drift ensures that the intracellular and extracellular environments are *electroneutral*, with the sum of charges in each nearly equal.

The combined flux of a charged molecule is inclusive of forces because of diffusion and drift — an *electrochemical potential*. The *Nernst-Planck equation* (1.1), or NPE, accurately describes this flux. It can be derived using the Einstein Relation, which states that the two fluxes of diffusion and drift are additive in the same medium, with diffusion calculated via Fick's Law and drift via Ohm's Law (Gray and Wu, 1997). Here the NPE is written in terms of current (rate of charge) rather than as a flux (rate of flow of molecules):

$$I = -\frac{\mu z^2}{N_A} F[C] \frac{dV}{dx} - \frac{\mu z}{N_A} RT \frac{d[C]}{dx} \quad (1.1)$$

In (1.1),  $I$  is the current (equal to the molecular flux multiplied by the valence of the charged molecules and  $F$ , the Faraday constant),  $[C]$  the ionic concentration,  $z$  the molecules' valence,  $\mu$  ionic mobility,  $V$  voltage,  $x$  the distance between the potentials,  $T$  the temperature,  $R$  the gas constant and  $N_A$  Avogadro's constant.

At an ion's steady state, the sum of fluxes will be zero. Assuming zero net flux in (1.1), one can derive the *reversal* or *Nernst potential* for an ion (Equation 1.2), which is commonly used in neuroscience:

$$E_C = \frac{RT}{zF} \ln \left( \frac{[C]_o}{[C]_i} \right) \quad (1.2)$$

where  $[C]_i$  is the ionic concentration inside the cell and  $[C]_o$  its concentration outside. The reversal or Nernst potential  $E_C$  of an ion  $C$  is the membrane voltage which exactly counterbalances the tendency for the ion to move down its electrochemical gradient across the membrane – i.e. the ion's net flux is zero (Coombs et al., 1955). The Nernst Equation therefore tells one at which membrane voltage ( $V_m$ ) an ion is at equilibrium.

### 1.1.3 The cellular electric field and membrane potential

Cell membranes are comprised of two electrically insulated components (the phospholipid bilayer) on either side of which water, a conductor, flows. This arrangement allows for charge to be separated or stored across the membrane, giving cell membranes the properties of a capacitor. Cells are often modelled using electrical circuits. In the equivalent circuit model, batteries represent channel or ionic reversal potentials, resistors represent resistance through channels and capacitors represent the membrane capacitance  $C_m$ .

The membrane capacitance allows for charge separation across the membrane. The collection of charged molecules creates an electrical field with the positive direction pointing

from the inside to the outside of the cell. This electric field sets up the cell's *membrane potential* ( $V_m$ ), an electrical potential inclusive of all charged objects.

To evaluate the membrane potential  $V_m$  of a modelled cell, one must use one of two approaches. Either, the sum of the currents through each component in the circuit is zeroed, i.e. setting  $\sum I_{capacitance} + I_{ion} = 0$ ,  $V_m$  is solved for in  $C_m \frac{dV_m}{dt} + \sum I_{ion} = 0$  ('charge sum' approach), or the charge difference  $q$  across the membrane because of individual ions is calculated, noting that  $C = \frac{q}{V}$  and assuming that the extracellular charges sum to 0, i.e.  $V_m = \frac{F \cdot \text{volume} \cdot (\sum z \cdot [\text{ion}^z]_i)}{C_m \cdot \text{area}}$  ('charge difference' approach). While the charge sum approach is the traditional strategy used in most models in the literature, the charge difference approach has the advantage of not requiring any initialisation values. Both approaches compute the same values for  $V_m$  provided the initial  $V_m$  for the charge sum approach is set equal to the charge difference equation (Fraser and Huang, 2004).

#### 1.1.4 Application of electrochemical equilibria and the ionic driving force

The Nernst-Planck equation is often simplified so that it can be applied efficiently in models to accurately quantify electrochemical ionic current  $I_{ion}$  across the cellular membrane. The constant field and Ohmic equations can be derived from the NPE. The constant field equation is given by (1.3), where  $P_m$  is the membrane permeability constant of the ion  $C$ , and  $\xi = \frac{zFV}{RT}$ :

$$I_{ion} = P_m z F \xi \left[ \frac{[C]_i e^\xi - [C]_o}{e^\xi - 1} \right] \quad (1.3)$$

The equivalent circuit equation (or 'Ohmic' equation, because it uses Ohm's law,  $I = \frac{1}{R}V = gV$ , where  $R$  is resistance and  $g$  conductance, the inverse of resistance) is given by:

$$I_{ion} = g(V_m - E_{ion}) \quad (1.4)$$

These equations can be modified to capture flux and the reversal potential when multiple ions are involved, for example through a selective receptor. Usually, the receptor will allow only some ions passage across the membrane when it is open or activated, and hence it creates a local area of restricted electrochemical potentials. These generalisations will be introduced in Section 1.2.1.

The Ohmic equation illustrates the important concept of the ionic *driving force*. In (1.4), the magnitude of  $I_{ion}$  is increased by larger differences between  $V_m$  and the ion's Nernst potential. This difference ( $V_m - E_{ion}$ ) is known as the driving force for the movement of the ion. It is the ionic driving force across a post-synaptic receptor that determines both the direction and magnitude of ionic flux when that receptor is activated by a neurotransmitter and opens. It therefore determines the type of response (depolarising or hyperpolarising) created by a synaptic input onto a neuron — the vital consequence of ionic homeostasis.

### 1.1.5 The $\text{Na}^+/\text{K}^+$ -ATPase establishes the cellular membrane potential and volume using the pump-leak mechanism

At steady state, the net transmembrane flux of an ion ought to be near zero. The implications when setting Equation 1.4 equal to 0 are striking: ionic reversal potentials tend towards  $V_m$  when only a ‘passive’ cellular set-up is used, and ions have a negligible driving force. Particular mechanisms actively distributing ions are necessary to move  $E_{ion}$  away from  $V_m$  and to maintain a non-zero driving force (Savtchenko et al., 2017).

Active mechanisms include pumps that use an energy source to shunt ions across the membrane against their electrochemical gradient. The sodium/potassium-ATPase ( $\text{Na}^+/\text{K}^+$ -ATPase) pump is an example of a prominent active ionic transport mechanism, and is responsible for the resting membrane potential in most animal cells, as well as the  $\text{Na}^+$  and  $\text{K}^+$  reversal potentials (Tosteson and Hoffman, 1960; Dierkes et al., 2006). The ATPase moves 3  $\text{Na}^+$  ions out to the extracellular environment for every 2  $\text{K}^+$  ions brought into the cell by employing the energy substrate adenosine triphosphate (ATP). Reversal potentials, once established by active mechanisms (e.g. the  $\text{Na}^+/\text{K}^+$ -ATPase), can be made available as energy sources for the coupled transport of other ions.

Along with its contribution to the cell’s electrical stability, the ATPase pump’s actions play a critical role in determining cellular osmolarity and volume (Tosteson and Hoffman, 1960; Armstrong, 2003; Liang et al., 2007; Kay, 2017). This is because impermeant molecules such as nucleic acids and proteins cannot cross the cell membrane and yet are still osmotically active. When the cell has only passive electrochemical mechanisms available, this results in the ‘Gibbs-Donnan’ effect (Hill, 1956): an uneven distribution of charged particles across the membrane which is osmotically unstable. Without the rigid cell walls present in plant cells, animal cells without active transporters would swell indefinitely. The  $\text{Na}^+/\text{K}^+$ -ATPase stabilises the cell volume by pumping ions across the membrane and allowing them to leak passively in a way which sets the intracellular osmolarity to that of the extracellular space (the ‘pump-leak’ mechanism) (Kay, 2017). The most important attributes of the pump-leak mechanism are active extrusion of  $\text{Na}^+$  (by the ATPase) combined with a low  $\text{Na}^+$  permeability, which renders  $\text{Na}^+$  ‘functionally impermeable.’ Hence, cells are able to reach osmotic equilibrium by broadly matching the concentration of impermeant anions with the concentration of externally restricted  $\text{Na}^+$ .

## 1.2 GABA<sub>A</sub> receptors mediate inhibitory signalling via chloride

### 1.2.1 The chloride driving force determines GABA<sub>A</sub> neurotransmission

This thesis is primarily focused on inhibitory synaptic signalling. Fast synaptic inhibition in the mature nervous system is mediated by both glycine receptors and type A  $\gamma$ -aminobutyric acid receptors (GABA<sub>AR</sub>s) (Krnjević and Schwartz, 1967; Werman et al., 1968). GABA<sub>AR</sub>s

are generally activated when bound by the neurotransmitter GABA. The effect of GABA binding to its receptor is based on the GABA driving force, the difference between the resting membrane potential  $V_m$  and the GABA reversal potential  $E_{GABA}$ , which is in turn set by the ions permeable through GABA<sub>A</sub>Rs. Ion gradients determine the outcome of neural signalling.

In a receptor permeable to several ion species such as the GABA<sub>A</sub>R, the reversal potentials of individual ions and their relative permeability through the receptor determine the receptor's reversal potential, as explained in Section 1.1.4. GABA<sub>A</sub>Rs are primarily permeable to chloride ( $Cl^-$ ). Bicarbonate ( $HCO_3^-$ ) ions also permeate, but to a much lesser degree (Bormann et al., 1987). The Goldman-Hodgkin-Katz equation (1.5) (Fig. 1.1 E), derived from the constant field equation, is classically employed to describe the reversal potential of GABA<sub>A</sub>Rs,  $E_{GABA}$  (Goldman, 1943; Hodgkin and Katz, 1949):

$$E_{GABA} = \frac{RT}{F} \ln \left( \frac{4[Cl^-]_{in} + [HCO_3^-]_{in}}{4[Cl^-]_{out} + [HCO_3^-]_{out}} \right) \quad (1.5)$$

An alternative formulation, based on the Ohmic approach (1.4), calculates  $E_{GABA}$  based on the ratio of the reversal potentials of  $Cl^-$  and  $HCO_3^-$ :  $E_{GABA} = \frac{4}{5}E_{Cl} + \frac{1}{5}E_{HCO_3}$  (Fig. 1.1 F). The current through the GABA<sub>A</sub>R when it is activated can therefore be written:

$$I_{GABA} = g_{GABA} \left( V_m - \left( \frac{4}{5}E_{Cl} + \frac{1}{5}E_{HCO_3} \right) \right) \quad (1.6)$$

$$= \frac{4}{5}g_{GABA}(V_m - E_{Cl}) + \frac{1}{5}g_{GABA}(V_m - E_{HCO_3}) \quad (1.7)$$

The contributions of both ions to  $E_{GABA}$  mean that  $E_{GABA}$  (typically  $-75$  mV) is much closer to the  $Cl^-$  reversal ( $-85$  mV) than the more positive  $HCO_3^-$  reversal ( $-20$  mV). Because of the weighting, shifts to transmembrane chloride gradients should have larger effects on  $E_{GABA}$  than shifts to transmembrane bicarbonate gradients. The bicarbonate gradient is also kept relatively stable by carbonic anhydrase, which is a catalyst in the reaction of  $H_2O$  and  $CO_2$  to replenish  $HCO_3^-$  (Kaila, 1994; Staley et al., 1995). Therefore the  $Cl^-$  driving force (the difference between the membrane potential  $V_m$  and  $E_{Cl}$ ) can be used as an approximation for the GABA<sub>A</sub>R driving force.

### 1.2.2 The importance of chloride concentration in GABA<sub>A</sub> receptor signalling

Because the magnitude and direction of the post-synaptic potential generated when GABA binds to its receptor is dependent on the  $Cl^-$  driving force, the efficiency of inhibition via GABA<sub>A</sub>Rs varies. There are two mechanisms through which GABA<sub>A</sub>Rs can inhibit target neurons (Fig. 1.1). Naturally, directly hyperpolarising the membrane (shifting the membrane potential negatively) is inhibitory (Fig. 1.1 B). In addition, and counter-intuitively, depolarising the membrane (a positive shift) and 'shunting' excitatory inputs is also an effective method of inhibition (Fig. 1.1 C). Shunting inhibition reduces local membrane re-

sistivity or electrical impedance (the ability of the neuron to oppose ionic flux). This short-circuits the system by allowing current to flow along an unintended path of low impedance and prevents the summation of excitatory post-synaptic potentials from nearby synapses (Andersen et al., 1980; Staley and Mody, 1992; Kaila, 1994). The more depolarising the GABA<sub>AR</sub> reversal potential, the lower the efficacy of GABAergic inhibition is through either of these mechanisms, and the chance of disinhibition increases (Fig. 1.1 D).

A curiosity in the types of GABA<sub>AR</sub>-mediated membrane polarisations is the ‘biphasic’ response, which describes the  $V_m$  shift of an initial hyperpolarisation followed by a depolarisation (Fig. 1.1 G). It occurs only under certain conditions, when there is intense activation of GABA<sub>AR</sub>s which overwhelm Cl<sup>-</sup> regulatory mechanisms but not the stability of  $E_{HCO_3}$  (Staley et al., 1995; Kaila et al., 1997; Perkins, 1999). As a result, during continued GABA<sub>AR</sub> activation,  $E_{GABA}$  becomes depolarised because it shifts towards  $E_{HCO_3}$ . This again illustrates the importance of Cl<sup>-</sup> fluctuations in determining GABA<sub>AR</sub> signalling: it is the disruption of Cl<sup>-</sup> homeostasis which enables the biphasic response.

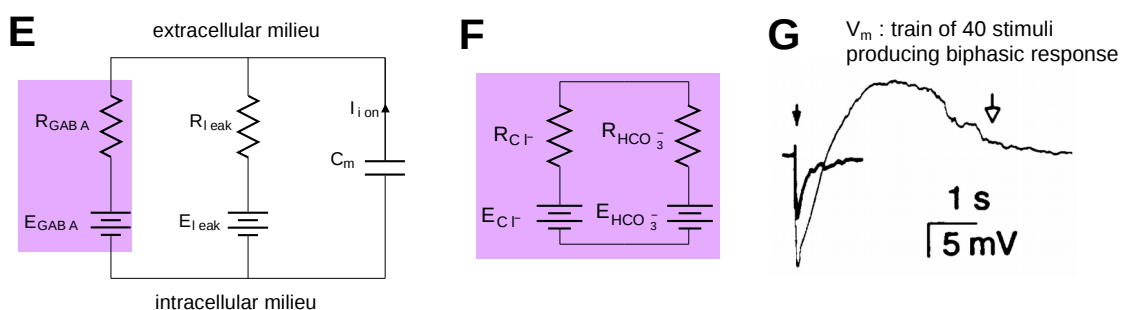
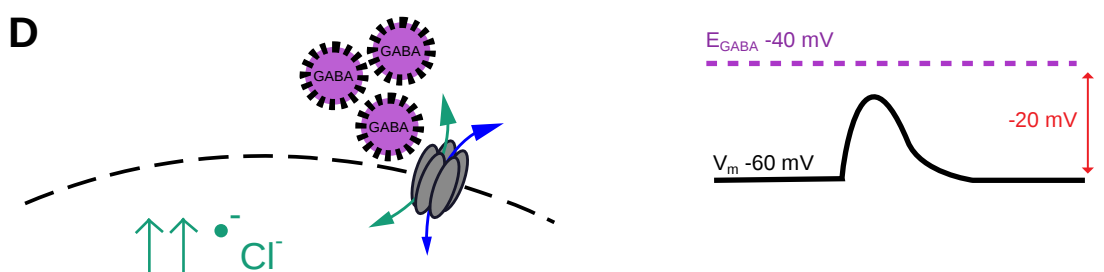
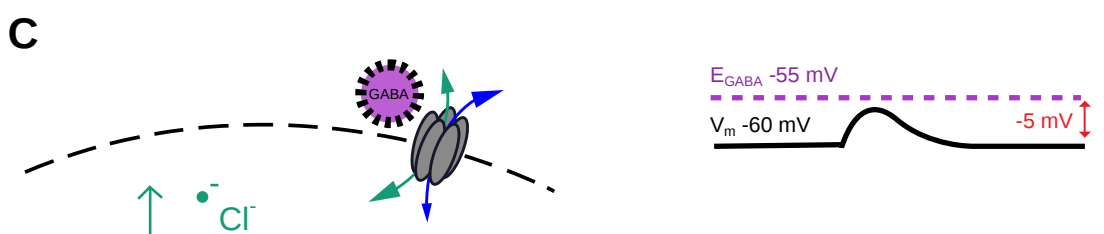
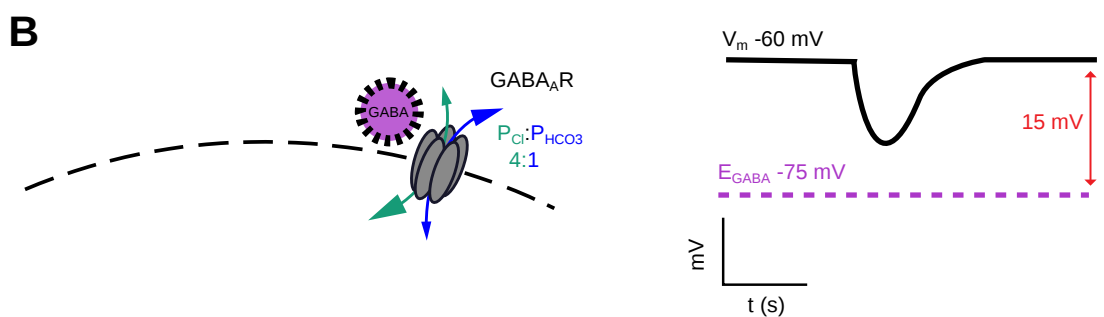
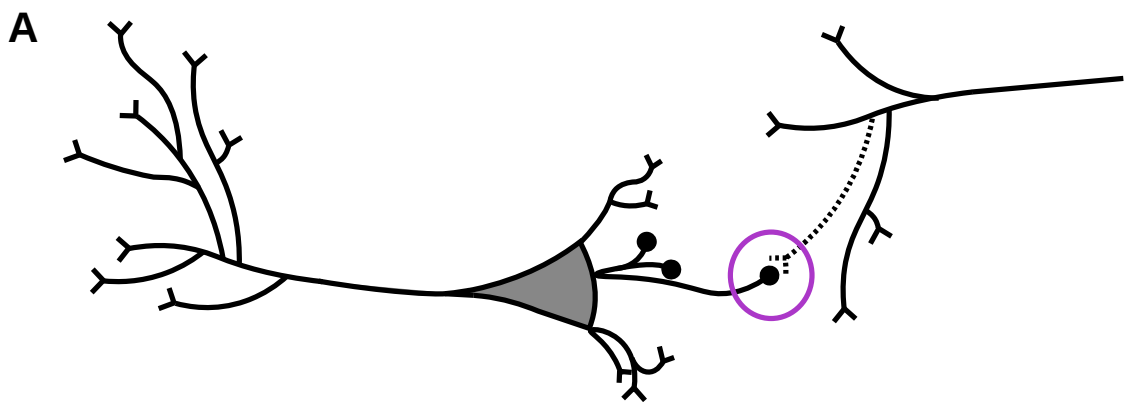
Shifts in the Cl<sup>-</sup> driving force are often associated with changes in  $E_{Cl}$  only, since  $V_m$  is set by all cellular charges. From the Nernst Equation (1.2),  $E_{Cl}$  shifts can involve changes to the extracellular chloride concentration [Cl<sup>-</sup>]<sub>o</sub>, or the intracellular concentration [Cl<sup>-</sup>]<sub>i</sub>. In the large volume of the extracellular environment, and because extracellular chloride concentrations are larger than intracellular concentrations, changes to [Cl<sup>-</sup>]<sub>o</sub> tend to have a small effect on  $E_{Cl}$ , so that the physiologically relevant parameter is [Cl<sup>-</sup>]<sub>i</sub>.

When [Cl<sup>-</sup>]<sub>i</sub> is increased in mature neurons, as has been shown in many disease and hyperexcitable network states (Kaila et al., 1997; Rivera et al., 2002; Price et al., 2009; Tyzio et al., 2014; Ellender et al., 2014),  $E_{GABA}$  shifts positively and thus the effect of GABA<sub>AR</sub> activation tends towards disinhibition. Figure 1.1 D shows that if intracellular chloride is very high, and the GABA<sub>AR</sub> reversal potential is more positive than the action potential threshold, GABA can cease to mediate inhibition.

Alterations in the Cl<sup>-</sup> driving force and the shift to disinhibition is undesirable because

---

**Figure 1.1 (facing page):** The response of the membrane potential to GABA<sub>AR</sub> activation depends on the intracellular chloride concentration (green) and chloride driving force (red arrows). (A) Synaptic contacts confer signalling from the pre-synaptic nerve ending to the post-synaptic dendrite via neurotransmitters. (B) At low intracellular chloride concentrations, GABA is inhibitory and causes hyperpolarisation of the membrane potential ( $V_m$ ). This is because when GABA binds to the GABA<sub>AR</sub>, the predominant flux through the receptor is carried by Cl<sup>-</sup> ions flowing down their electrochemical gradient into the cell, based on the Cl<sup>-</sup> driving force. The membrane potential is driven towards the more negative  $E_{GABA}$ . (C) At raised intracellular chloride concentrations, GABA<sub>AR</sub> activation causes chloride ions to flow out of the cell and the membrane to depolarise.  $V_m$  is driven towards a more positive  $E_{GABA}$ . The depolarisation can still be inhibitory via ‘shunting’ inhibition. (D) At even higher intracellular chloride concentrations and therefore reversal potential  $E_{GABA}$ , GABA<sub>AR</sub> activation causes a larger depolarisation that can become excitatory. (E) The equivalent circuit model using a combined Goldman-Hodgkin-Katz equation for  $E_{GABA}$ . (F) Substitution of the GABA leak for an approach using the  $E_{Cl}$  and  $E_{HCO_3}$  potentials, which can model the biphasic GABA activation in G. (G) Experimental example of biphasic response from Staley et al. (1995): bold trace, the usual hyperpolarising  $V_m$  response to a single GABA<sub>A</sub> stimulus; lighter trace, the response to a train of 40 GABA<sub>A</sub> stimuli at 200 Hz.



it can cause widespread pathology, excitatory activity and cellular death (Wake et al., 2007; Ellender et al., 2014). The active mechanisms determining  $\text{Cl}^-$  driving force — i.e. the separation of  $E_{\text{Cl}}$  from  $V_m$  — are therefore of considerable interest. In this thesis, I aimed to explore the cellular mechanisms underlying the establishment of  $\text{Cl}^-$  driving force in neurons using computational models based on biophysical features. Because the principles outlined above set up the basis of the cell, the first objective in this thesis was to develop the theoretical and computational tools to model basic biophysical cellular features important for ion homeostasis in cells.

## 1.3 Cation-chloride cotransporters

As discussed above, to separate  $E_{\text{Cl}}$  from the membrane potential ( $V_m$ ), as we know occurs in cells like neurons (Thompson et al., 1988), it is necessary for active regulation to modulate  $\text{Cl}^-$  steady states. Ionic transport is a form of active regulation. For over 30 years, transmembrane transporters called the cation-chloride cotransporters (CCCs) have been thought to be the main mechanism for distributing  $\text{Cl}^-$ . These transporters utilise the gradient of positively charged ions (cations) to modulate  $\text{Cl}^-$  co-flux in the same direction across the cell membrane, so that electroneutral transport occurs.

### 1.3.1 Types of cation-chloride cotransporters

In immature neurons,  $[\text{Cl}^-]_i$  is high and, where present,  $\text{GABA}_{\text{A}}\text{Rs}$  are thought to be depolarising and shunting (Ben-Ari (2002)). However, most mature neurons have a low  $[\text{Cl}^-]_i$  and therefore  $\text{GABA}_{\text{A}}\text{Rs}$  in mature neurons mediate inhibitory transmission (Kaila et al., 2014) (Fig. 1.1 B). The current dogma supports the idea that the change in activity of two particular CCCs is responsible for the active shift to low concentrations in mature neurons (Ben-Ari, 2002; Blaeser et al., 2009; Kaila et al., 2014). Their activity is illustrated with the  $\text{GABA}_{\text{A}}\text{R}$  and  $\text{Na}^+/\text{K}^+$ -ATPase, which maintains the potassium gradient, in Figure 1.2 A.

The type 2  $\text{K}-\text{Cl}$  cotransporter (KCC2) is thought to be the more important CCC and  $\text{Cl}^-$  regulator expressed in mature neurons (Rivera et al., 1999; Williams et al., 1999; DeFazio et al., 2000; Kaila et al., 2014). KCC2 uses the potassium gradient to drive  $\text{Cl}^-$  to exit the cell thus decreasing  $[\text{Cl}^-]_i$  (Payne, 1997; Thompson et al., 1988). KCC2 transporters are progressively upregulated in neurons over development (Rivera et al., 1999; Ganguly et al., 2001; Stein et al., 2004; Dzhala et al., 2005; Uvarov et al., 2006; Hyde et al., 2011). By reducing intracellular chloride following chloride-loading induced by  $\text{GABA}_{\text{A}}\text{R}$  inhibition (Fig. 1.2 B), chloride extrusion in mature neurons also allows serial  $\text{GABA}_{\text{A}}\text{R}$  signals in the same neuron to remain inhibitory (Payne, 1997; Pellegrino et al., 2011).

Type 1  $\text{Na}^+-\text{K}^+-\text{Cl}^-$  cotransporters (NKCC1) utilise the sodium gradient to facilitate  $\text{Cl}^-$  uptake. NKCC1 expression is typically high in immature neurons (Balakrishnan et al., 2003; Pfeffer et al., 2009). Here, the cotransporter is postulated to cause high enough  $[\text{Cl}^-]_i$  that  $\text{GABA}_{\text{A}}\text{R}$ -mediated synaptic transmission is depolarising (Ganguly et al., 2001; Ben-Ari,

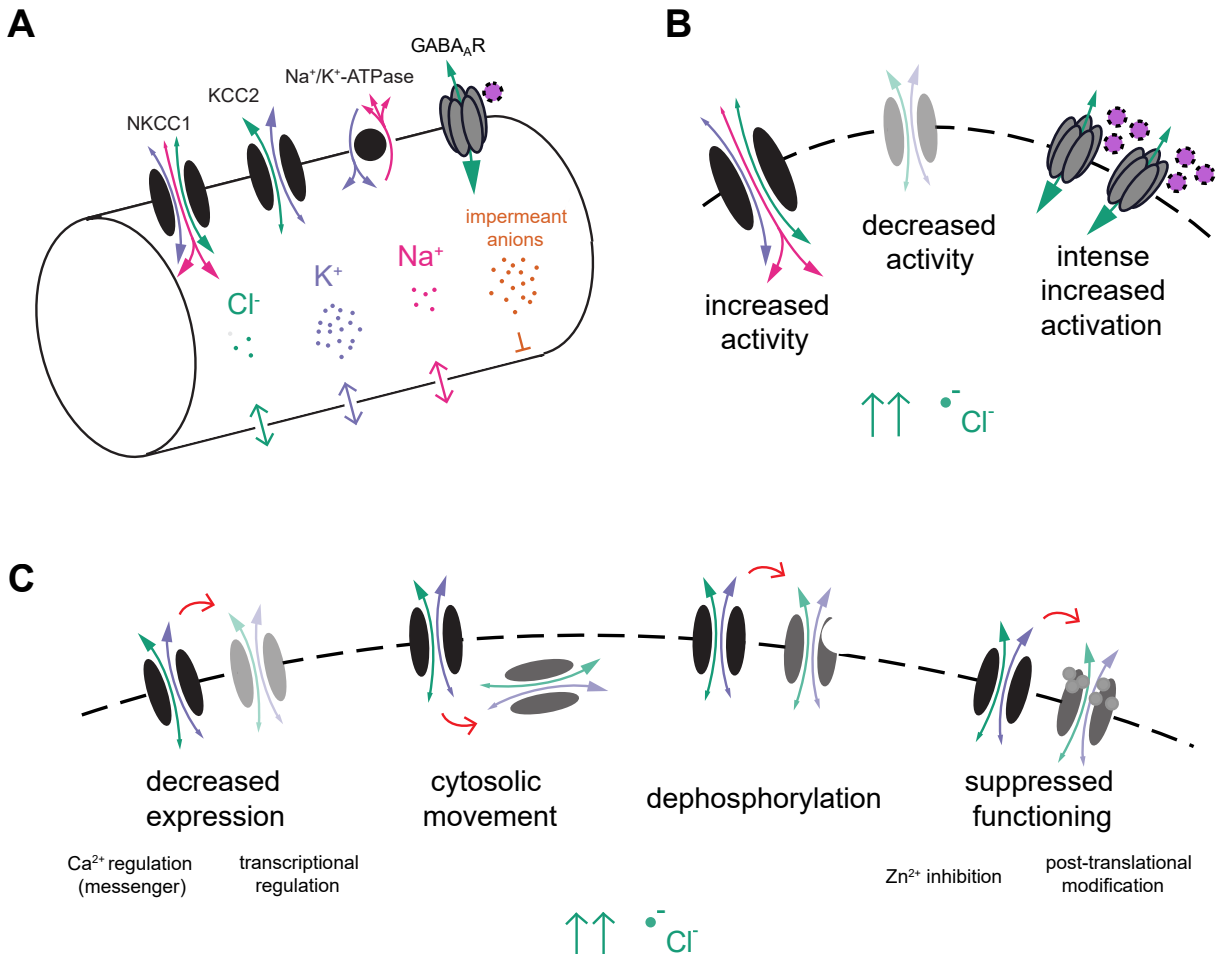


**Figure 1.2:** Important transporters in chloride homeostasis and mechanisms of increasing intracellular chloride concentration. (A) A neuronal membrane including depictions of the sodium-potassium ATPase, KCC2, NKCC1 and GABA<sub>A</sub> receptor, as well as indications of the normal flux of ions ( $\text{Cl}^-$ , green;  $\text{K}^+$ , purple;  $\text{Na}^+$ , pink) through each. Impermeant ions are included in orange. (B) Broadly, states of increased  $[\text{Cl}^-]_i$  are secondary to changes in the activity of the cation-chloride cotransporters KCC2 and NKCC1, or over short periods of time from intense activation of GABA<sub>A</sub>Rs which overwhelms usual rectification mechanisms. (C) Mechanisms that diminish KCC2 activity. KCC2 activity may be reduced following decreased expression of the cotransporter, which can be mediated through transcriptional regulation and regulation of secondary messengers like  $\text{Ca}^{2+}$ , internalisation or cytosolic movement of the cotransporter from the membrane, dephosphorylation, and suppression of KCC2 functioning via direct inhibition or post-translational modifications.

2002; Pfeffer et al., 2009), although this result has recently been questioned on the basis of differences between *in vitro* and *in vivo* experiments (Valeeva et al., 2016). Depolarising GABA<sub>A</sub>R-mediated transmission may enable a threshold of disinhibition that encourages the creation of synapses and general activity without causing cell death (as would be the case for glutamatergic excitation) (Pfeffer et al., 2009). NKCC1 is progressively downregulated during development (Dzhala et al., 2005). As a result, NKCC1 is thought to have a limited role in mature neuronal chloride homeostasis.

Other CCCs are not contributory in neurons. For example, KCC1 is expressed non-specifically in mammalian cells, and is not likely to mediate chloride regulation in the nervous system because it has a low affinity for both K<sup>+</sup> and Cl<sup>-</sup> (Gillen et al., 1996).

### **1.3.2 Pharmacological evidence for the role of CCCs in setting the chloride driving force**

Studies which have inhibited CCCs using pharmacological agents have observed changes to E<sub>Cl</sub> or E<sub>GABA</sub> that are consistent with the dogma that CCCs establish the Cl<sup>-</sup> driving force. Specifically, blocking KCC2 may cause an increase in [Cl<sup>-</sup>]<sub>i</sub> in mature neurons (Barmashenko et al., 2011; Di Angelantonio et al., 2014; Tang et al., 2015), and blocking NKCC1 either no change (normal mature neurons) or a decrease in [Cl<sup>-</sup>]<sub>i</sub> (Friauf et al., 2008; Hewitt et al., 2009; Barmashenko et al., 2011; Chen et al., 2014; Tyzio et al., 2014; MacKenzie and Maguire, 2015). Importantly, in several studies, using the non-selective CCC blocker furosemide depolarised E<sub>GABA</sub> to levels near that of V<sub>m</sub>, supporting the role of the transporter in establishing Cl<sup>-</sup> driving force (Thompson and Gähwiler, 1989; Pathak et al., 2007; Lee et al., 2011).

### **1.3.3 Evidence from comparative disease models for the role of CCCs in setting the internal chloride concentration**

Changes in the expression or activity of CCCs that correspond with expected shifts in the Cl<sup>-</sup> gradient have been reported in numerous disease states, providing further evidence for the role of CCCs in Cl<sup>-</sup> regulation (Table 3.1). Downregulation of KCC2 and upregulation of NKCC1 can cause accumulation of intracellular chloride, or Cl<sup>-</sup> loading (Fig. 1.2 B). Often these CCC-to-[Cl<sup>-</sup>]<sub>i</sub> associations are confirmed via quantification of altered transporter expression levels, but other mechanisms can also result in CCC activity shifts. They include phosphorylation status (Balakrishnan et al., 2003; Wake et al., 2007; MacKenzie and Maguire, 2015; Alessi et al., 2014), intracellular calcium accumulation (Hewitt et al., 2009; Fiumelli et al., 2005) and changes in the localisation (or expression on the surface of the membrane) of CCCs (Wake et al., 2007; Tyzio et al., 2014; MacKenzie and Maguire, 2015) (Fig. 1.2 C).

Contradictory results have recently also been reported, in which blocking KCC2, NKCC1 or both did not result in shifts in [Cl<sup>-</sup>]<sub>i</sub> (Glykys et al., 2014). These findings have prompted a re-evaluation of the mechanisms underlying chloride homeostasis, including the controversial

Disease or model	Study	$\Delta[\text{Cl}^-]_i$	$\Delta\text{KCC2}$	$\Delta\text{NKCC1}$	Mechanism for changes in CCCs
Epilepsy (excitation)	Barmashenko et al. (2011)	↑	↓	↑	Not explored
	Bragin et al. (2010)	↑	↓	↑	Not explored
	Lee et al. (2011)	↑	↓	None	Dephosphorylation
	Pathak et al. (2007)	↑	↓	None	Not explored
Glioma or peri-glioma	Campbell et al. (2015)	↑	↓	None	KCC2 dephosphorylation
	Conti et al. (2011)	↑	↑	↑	$\text{Zn}^{2+}$ inhibition of KCC2 activity
	Di Angelantonio et al. (2014)	↑	↓	Unknown	$\uparrow [\text{Zn}^{2+}]_i$
	Pallud et al. (2014)	↑	↓	↑	Cytosolic movement
Stress	Galeffi et al. (2004)	↑	↓	None	Not explored
	MacKenzie and Maguire (2015)	↑	↓	Functional*	Dephosphorylation
Neuropathic pain	Chen et al. (2014)	↑	None	Functional*	Disrupted micro-tubule dynamics, dynein
	Coull et al. (2003)	↑	↓	Unknown	Not explored
	Ferrini et al. (2013)	↑	↓	Unknown	BDNF release by microglia
	Tang et al. (2015)	↑	↓	None	Not explored
Nociception	Funk et al. (2008)	↑	↓	↑	Phosphorylation
Substrate knockouts	Lagostena et al. (2010)	↑	↓	None	Nerve growth factor depletion
	Mahadevan et al. (2015)	↑	↓	Unknown	Neto2-knockout; ↓ phosphorylation
Hypothyroidism	Friauf et al. (2008)	↑	Unknown	Functional*	Post-translational modifications
Autism	Tyzio et al. (2014)	↑	↓	Functional*	Post-translational modifications
Δ regions	Klein et al. (2018)	↑	↓	Unknown	Baseline expression levels

**Table 1.1:** Changes in the activity of cation-chloride cotransporters in different disease models are associated with changes in intracellular chloride concentration. For each study, grouped by disease, the shift in  $[\text{Cl}^-]_i$  (on the basis of  $E_{\text{GABA}}$ ,  $E_{\text{Cl}}$  or via direct imaging), change in KCC2 expression, change in NKCC1 expression and possible mechanism(s) underlying the changes was extracted. \* Functional confirmation of  $\Delta\text{NKCC1}$  was determined by the presence of  $[\text{Cl}^-]_i$  recovery with the application of bumetanide (a NKCC1 inhibitor).

impermeant anion hypothesis (see the following section). Therefore, the second objective of my thesis was to use computational methods to explore the role of CCCs in establishing the transmembrane concentration gradient and driving force for  $\text{Cl}^-$  in neurons.

## 1.4 The impermeant anion hypothesis of chloride regulation

Recently, it has been suggested that impermeant anions, and not CCCs, establish the transmembrane gradient and driving force for  $\text{Cl}^-$  in neurons (Fig. 1.3). This impermeant anion hypothesis suggests that chloride equilibria are determined only by the electrochemical action on chloride ions by anions that are not permeable to the cell membrane (Fig. 1.3). It hypothesises that cation-chloride cotransporters regulate another aspect of the cell, osmolarity and therefore cellular volume, without affecting the chloride gradient (Delpire and Staley, 2014; Glykys et al., 2014; Glykys et al., 2017).

The premise in the paper proposing the alternative is that the cumulative intracellular concentration of negative ion species should be constant, i.e.  $[\text{X}^-]_i + [\text{Cl}^-]_i$  is constant, where X represents anions other than chloride (Glykys et al., 2014). In the impermeant anion hypothesis, changes to impermeant anions are the primary mediators of changes to the  $\text{Cl}^-$  gradient, which is set by the Donnan Equilibrium, with passive channels allowing for the chloride flux that maintains the equilibrium.

Implications of the alternative hypothesis are far-reaching. It potentially explains common pathophysiology, such as the shift from cytotoxic oedema to seizure-like states, by providing a mechanism that influences both cellular volume and inhibition (Glykys et al., 2014). This would link  $\text{Cl}^-$  modification to disease processes involving protein and volume flux, like stroke, meningitis and traumatic brain injury (Glykys et al., 2017). The proposers of the impermeant anion hypothesis suggest that potential treatment avenues for these diseases could be influenced greatly, by shifting focus from manipulation of transporters and ion channels to the targetting of impermeant anions.

Theoretical constraints based on thermodynamic principles have been posed in refutation (Voipio et al., 2014; Kaila et al., 2014). These opponents to the impermeant anion hypothesis claim that impermeant anions exert an equal but opposite effect on cations as they do on anions such as  $\text{Cl}^-$ , and therefore cannot affect the overall electrochemical gradient of an ion.

### 1.4.1 Experimental evidence for the role of impermeant anions in setting the chloride gradient

Recent experimental data from the Staley laboratory has demonstrated that modification of impermeant anions was more likely to cause consistent intracellular chloride shifts than CCCs (Glykys et al., 2014). However, the evidence has not been replicated and is controversial, since the use of chloride-sensing fluorescent dyes vulnerable to pH change may have introduced inaccuracy (Pellegrino et al., 2011; Bertolini et al., 2012; Arosio and Ratto, 2014;

Luhmann et al., 2014). Klein et al. (2018) repeated similar experiments by modifying extracellular impermeant anions, but found that altering extracellular impermeants only affected  $E_{\text{GABA}}$  modestly when compared to KCC2's role. In both cases, there were no comments on how anions influenced other cellular parameters, in particular  $\text{Cl}^-$  driving force, the most important measurement in  $\text{Cl}^-$  regulation since it sets inhibitory synaptic signalling.

There is a lack of research regarding possible mechanisms, scenarios and rationales underpinning impermeant anion-driven  $\text{Cl}^-$  regulation. However, it is known that chronic disease is often characterised by morphological and environmental changes, such as microglial activation (Coull et al., 2003) and cell swelling (Chen et al., 1999; Cesetti et al., 2011), which could conceivably result in changes to intra- and extra-cellular protein matrices. These in turn could result in modulation of impermeant anion concentrations.

Additional experimental evidence for the impermeant anion hypothesis is limited because the effects of impermeant anion manipulation are difficult to measure. For greatest value and impact, experimental avenues could be informed by theoretical predictions — so far, no models exist that fully describe the role of impermeant anions in  $\text{Cl}^-$  homeostasis. Therefore, the third objective of my thesis was to use biophysical models to investigate the influence of impermeant anions on  $\text{Cl}^-$  concentration and driving force.

#### 1.4.2 Cellular regulation of volume and osmolarity

If impermeant anions were the only mechanism setting the chloride gradient, it is implied that CCCs and KCC2 in particular should not affect  $E_{\text{Cl}}$ . According to the impermeant anion hypothesis, KCC2 transports water as well as ions, and functions as an osmotic regulator rather than a chloride regulator (Delpire and Staley, 2014).

Neurons do not have aquaporins (water channels) and are therefore thought to have a reduced capacity to regulate cell volume changes (Andrew et al., 2007). Because water movement is known to occur with changes in ion concentrations, it has been proposed that CCCs cotransport a fixed ratio of water molecules along with cations and  $\text{Cl}^-$  (MacAulay et al., 2004; Steffensen et al., 2018). This may link GABA<sub>A</sub>R activation to osmotic regulation in the brain (Cesetti et al., 2011). Therefore, it is suggested that changes in  $\text{Cl}^-$  homeostasis in neurons are based on water-ion flux, and CCCs do not function to maintain the chloride gradient but rather to determine the osmotic set-point by responding to transmembrane water concentration differences.

This theory comes with many caveats. Although there is some recent experimental data supporting CCC-mediated water transport (Steffensen et al., 2018), there is no definitive thermodynamic evidence for the theory's extension to the idea that water itself can cause a gradient that provides the energetic basis of ionic cotransport. Instead, water may be cotransported as a byproduct of normal CCC activity. In addition, even if CCCs are significant water transporters, the natural cell membrane has some permeability to water (Hernández and Cristina, 1998) and can also counter osmotic pressures through membrane conformation (stretching or shrinking) as well as via the cytoskeletal elements which can

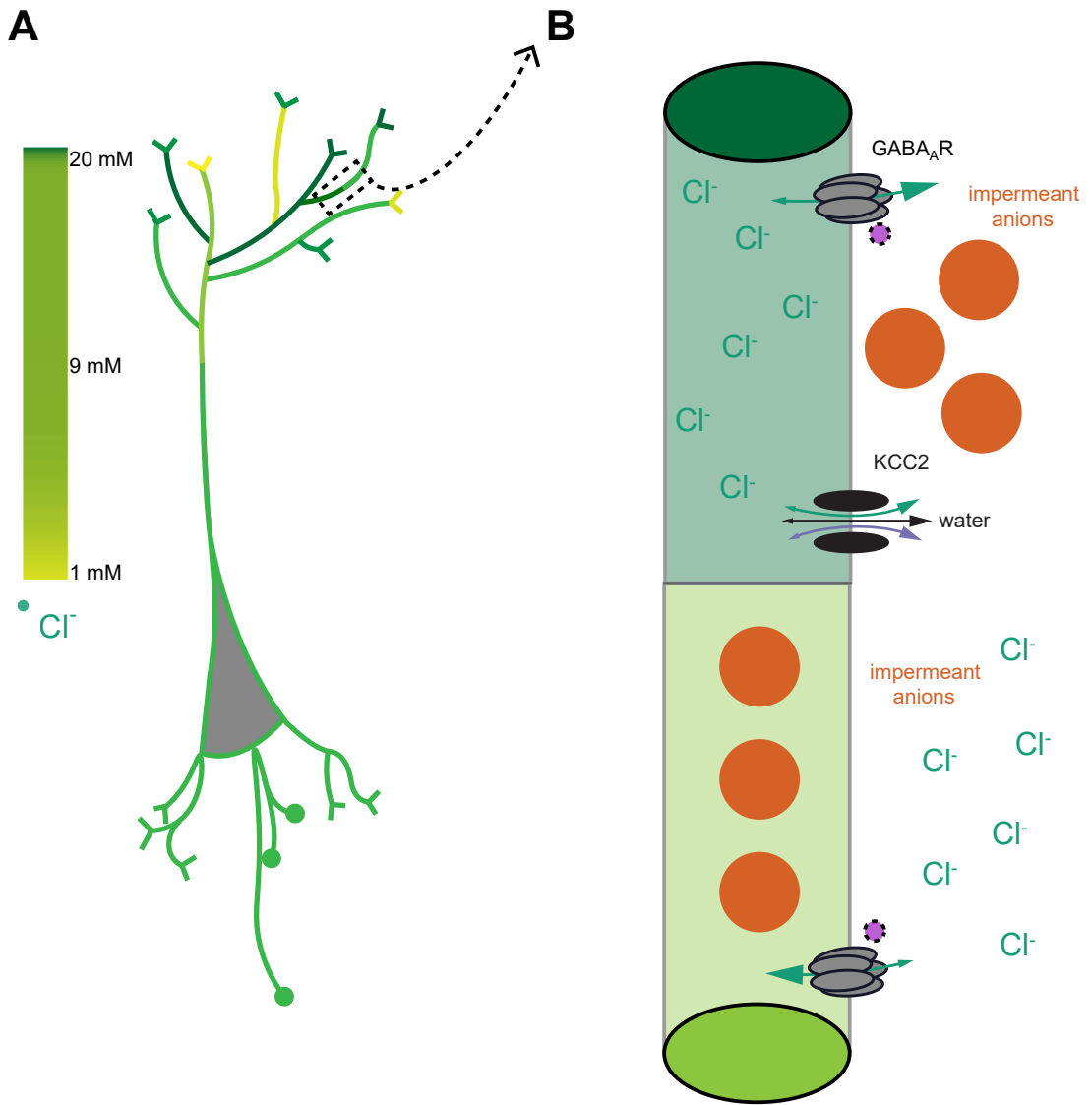


**Figure 1.3:** Proposition for the central role of impermeant anions in setting the chloride gradient and driving force. (A) In the Glykys et al. (2014) paradigm, it is suggested that  $[Cl^-]_i$  can vary in different sub-cellular locations secondary to the placement of immobile, impermeant anions. Varying  $[Cl^-]_i$  in green (left bar) corresponds with the neuron's dendritic  $[Cl^-]_i$  differentiation. (B) Taking a closer view at an area in which  $[Cl^-]_i$  changes in A, it is proposed that impermeant anions set  $[Cl^-]_i$  and therefore the driving force and response to GABAergic activation, while KCC2 transporters may rectify acute currents and regulate water flux, without affecting stable  $[Cl^-]_i$ . Top, high  $[Cl^-]_i$  is suggested to be caused by local, relatively high extracellular concentrations of impermeant, immobile anions, which repel  $Cl^-$  so that the local charge balance is maintained. This results in GABAergic shifts to disinhibition ( $Cl^-$  exits the cell on GABA<sub>AR</sub> activation). KCC2 is argued not to affect the baseline  $Cl^-$  concentration. Bottom, low  $[Cl^-]_i$  is postulated to be caused by local, relatively high intracellular concentrations of impermeant, immobile anions. This is suggested to maintain inhibitory GABAergic signalling.

act as a ‘sponge’ (Dai et al., 1998; Sachs and Sivaselvan, 2015).

One would need to compare the efficacies of osmotic mechanisms to truly understand what role CCCs might play in volume homeostasis. Furthermore, because they are osmotically active, changes in impermeant anions may also influence cell volume and osmotic homeostasis. Regardless of the mechanism, cellular volume shifts interact with ionic homeostasis, since increasing volume dilutes concentration. Therefore, the fourth objective of my thesis was to consider osmolarity and volume constraints in the context of  $\text{Cl}^-$  homeostasis.

#### 1.4.3 Local regulation of chloride concentration

Extending the role of impermeant anions, it has been postulated that impermeant anions are able to mediate local differences in  $[\text{Cl}^-]_i$  because they can act as immobile electrostatic components inside or outside a specific area of the cell, influencing the local distribution of surrounding ions like  $\text{Cl}^-$  (Glykys et al., 2014). There is some evidence that  $\text{Cl}^-$  can be held at different local, sub-cellular levels within domains of a cell (Szabadics et al., 2006; Glickfeld et al., 2009; Woodruff et al., 2009; Zhang et al., 2013; Mohapatra et al., 2016), and it is possible that spatial differences in intracellular and extracellular structures could lead to differences in the electric field and hence in the cellular membrane potential, distortions which are invisible during patch-clamping (Savtchenko et al., 2017). Whether this results in distinct local  $\text{Cl}^-$  driving forces — a combination of both  $V_m$  and  $E_{\text{Cl}}$  — has implications for the passage of inhibitory signals (Fig. 1.3 A and B).

Electrodiffusion, the movement of ions through a fluid medium via diffusive and electric forces, is an important determinant of local phenomena. Classically, Rall’s cable theory is a method that incorporates the passage of electric current in branching neurite structures via passive electrical ‘cable’ properties (Gray and Wu, 1997). However, the Nernst-Planck equation (1.1) is widely considered a more accurate method for calculating ion concentrations and membrane potential in neurites, since it also includes diffusion: substantial differences in outcomes have been noted when comparing these equations in small structures like dendrites and dendritic spines (Qian and Sejnowski, 1989; Qian and Sejnowski, 1990; Savtchenko et al., 2017). These variations bring home the importance of understanding the influence of electrodiffusion on cellular homeostasis.

Whether impermeant anions, which once immobile no longer contribute active energy to the system, can modify local  $[\text{Cl}^-]_i$  and  $\text{Cl}^-$  driving force has caused some debate because of the thermodynamic requirement that creating ‘perpetual ionic motion’ would require an energy source (Kaila et al., 2014). With electrodiffusion considered, it has been argued that the ‘repelling’ action of impermeant anions on  $\text{Cl}^-$  can occur only immediately around an impermeant molecule with high charge density, while the driving force nearby remains unperturbed (Savtchenko et al., 2017). In contrast, differential subcellular expression levels of CCCs use the energy source of the  $\text{K}^+$  gradient to drive activity, and therefore could in theory drive local differences in  $\text{Cl}^-$  that are actively maintained.

Because the role of mechanisms of  $\text{Cl}^-$  homeostasis in driving local  $\text{Cl}^-$  driving force

differences is unclear, the fifth objective of my thesis was to model electrodiffusion across multiple cellular compartments. I hoped to compare spatial influences on  $\text{Cl}^-$ . Objective six was to extend a multi-compartment representation of electrodiffusion to include GABA<sub>A</sub>Rs, since the influence of local  $\text{Cl}^-$  driving force changes on post-synaptic potentials should provide the final link in my thesis to show how driving forces and the mechanisms setting them might affect fast inhibitory signalling.

## 1.5 Aim and objectives

### 1.5.1 Aim

The overall aim of my thesis was to use computational models based on biophysical first principles to investigate the relative importance of different cellular mechanisms for determining  $\text{Cl}^-$  concentration and  $\text{Cl}^-$  driving force in neurons.

### 1.5.2 Objectives

The contributing objectives were to:

1. Develop the theoretical and computational tools to model ion homeostasis in cells, including passive ion conductances, cation-chloride cotransport, impermeant anions, water movement and volume changes.
2. Determine the role of CCCs in establishing  $\text{Cl}^-$  concentration and driving force in the model.
3. Investigate whether and how alterations in impermeant anions influence  $\text{Cl}^-$  concentration and driving force in the model.
4. Probe the role of osmolarity and water transport for  $\text{Cl}^-$  homeostasis in the model.
5. Incorporate electrodiffusion into my model to determine whether alterations to impermeant anions or CCCs can mediate local differences in  $\text{Cl}^-$  concentration and the  $\text{Cl}^-$  driving force.
6. Observe whether effects on  $\text{Cl}^-$  driving force have relevance for synaptic neurotransmission by comparing GABA<sub>A</sub>R post-synaptic potentials in the model.
7. Continuously compare simulation results to theoretical predictions and available experimental evidence to evaluate their validity.

# Chapter 2

## Methods

### 2.1 Single compartment model

The single compartment model consisted of a cylindrical semi-permeable membrane separating the extracellular solution from the intracellular milieu with variable cellular volume. The extracellular ionic concentrations were assumed constant (Table 2.1). Permeable ions in the model were  $K^+$ ,  $Na^+$  and  $Cl^-$  with their usual charges, while impermeant anions X were assumed to be a heterogenous group of impermeant chemical species with average intracellular charge  $z$  and extracellular charge -1.  $z$  was chosen on the basis of known resting intracellular ion concentrations and osmolarity  $\Pi$  (Lodish et al., 2009; Raimondo et al., 2015). Bicarbonate ions were not included in my model as they were assumed to be important in acute depolarising effects (via GABA<sub>AR</sub>s) rather than chronic shifts in  $Cl^-$  driving force, which was the focus for this thesis (Staley and Proctor, 1999).

The single compartment model included ionic leak currents for the permeable ions, the  $Na^+/K^+$ -ATPase and a cation-chloride cotransporter, the  $K^+-Cl^-$  cotransporter KCC2. KCC2 rather than NKCC1 is thought to be the most active CCC in mature neurons (Ben-Ari, 2002), and so to maintain conceptual simplicity NKCC1 was not included. Therefore, it was assumed that the effect sizes secondary to KCC2 manipulation could broadly be expected from other CCCs, although in directions reasonable for the specific symporter. Cell volume ( $w$ ) change was based on osmotic water flux and incorporated a membrane surface area scaling mechanism. The constants and default parameters for the model are presented in Table 2.1.

An analytical solution to the model at steady state was derived using standard techniques as described in Section (3.1.2). The numerical model was initialised assuming conditions close to electroneutrality and an osmotic equilibrium between the intracellular and extracellular compartments. A forward Euler approach was used to update variables at each time step ( $dt$ ) of 1 ms. Using a smaller  $dt$  did not influence the results. Code was written in Python 2 and is available on GitHub (<https://github.com/kiradust/model-of-neuronal-chloride-homeostasis>).

	<b>Value</b>	<b>Description</b>
<b>Constants</b>		
F	96485.33 C/mol	Faraday constant
R	8.31446 J/(mol·K)	Universal gas constant
T	310.15 K	Absolute temperature (37°C)
<b>Parameters</b>		
$C_m$	2 $\mu\text{F}/\text{cm}^2$	Membrane capacitance (Qian and Sejnowski, 1989)
$g_{\text{Na}}$	20 $\mu\text{S}/\text{cm}^2$	$\text{Na}^+$ leak conductance (Kager et al., 2000)
$g_{\text{K}}$	70 $\mu\text{S}/\text{cm}^2$	$\text{K}^+$ leak conductance (Kager et al., 2000)
$g_{\text{Cl}}$	20 $\mu\text{S}/\text{cm}^2$	$\text{Cl}^-$ leak conductance (Kager et al., 2000)
$g_{\text{KCC2}}$	20 $\mu\text{S}/\text{cm}^2$	KCC2 conductance (per ion) (Doyon et al., 2016)
$v_w$	0.018 $\text{dm}^3/\text{mol}$	Partial molar volume of water (Hernández and Cristina, 1998)
$p_w$	0.018 $\text{dm}/\text{s}$	Osmotic permeability (Hernández and Cristina, 1998)
$k_m$	25 N/dm	Variable for membrane tension (higher than reported in Dai et al. (1998); used here to accentuate differences in osmolarity)
P	0.1 C/( $\text{dm}^2 \cdot \text{s}$ )	Default pump rate constant (fitted)
$[\text{Na}^+]_o$	145 mM	Extracellular $\text{Na}^+$ concentration
$[\text{K}^+]_o$	3.5 mM	Extracellular $\text{K}^+$ concentration
$[\text{Cl}^-]_o$	119 mM	Extracellular $\text{Cl}^-$ concentration
$[\text{X}^-]_o$	29.5 mM	Extracellular impermeant anion (X) concentration (all extracellular concentrations as in Lodish et al. (2009); Raimondo et al. (2015))
$D_{\text{Na}}$	$1.33 \times 10^{-7} \text{ dm}^2/\text{s}$	$\text{Na}^+$ diffusion constant (Hille, 2001)
$D_{\text{K}}$	$1.96 \times 10^{-7} \text{ dm}^2/\text{s}$	$\text{K}^+$ diffusion constant (Hille, 2001)
$D_{\text{Cl}}$	$2.03 \times 10^{-7} \text{ dm}^2/\text{s}$	$\text{Cl}^-$ diffusion constant (Hille, 2001)
$g_{\text{synapse}}$	1 nS	Conductance of GABAergic synapses
$\text{GABA}_{\text{max}}$	1 mM	Saturating concentration of GABA molecules
$\alpha$ and $\beta$	$0.5 \text{ ms}^{-1}\text{mM}^{-1}$ and $0.1 \text{ ms}^{-1}$ respectively	Forward and backward rate constants for GABA binding (GABAergic synapse parameters all given by Destexhe et al. (1994))
<b>Variables</b>		
<i>(default steady state)</i>		
$V_m$	-72.6 mV	Membrane potential
$[\text{Na}^+]_i$	14.0 mM	Intracellular $\text{Na}^+$ concentration
$[\text{K}^+]_i$	122.9 mM	Intracellular $\text{K}^+$ concentration
$[\text{Cl}^-]_i$	5.2 mM	Intracellular $\text{Cl}^-$ concentration
$[\text{Na}^+]_i$	14.0 mM	Intracellular $\text{Na}^+$ concentration
$[\text{X}^-]_i$	154.9 mM	Intracellular impermeant anion (X) concentration
$z$	-0.85	Average charge of intracellular X (all intracellular concentrations and $V_m$ as in Lodish et al. (2009); Raimondo et al. (2015))

**Table 2.1:** Constants, default parameters and usual steady state values for variables used in the biophysical model.

### 2.1.1 Membrane potential

The membrane potential  $V_m$  was based on the ‘Charge Difference’ approach of Fraser and Huang (2004) as follows:

$$V_m = \frac{F([Na^+]_i + [K^+]_i + [Cl^-]_i + z[X^z]_i)}{C_m A_m} \quad (2.1)$$

where  $F$  is Faraday’s constant,  $C_m$  is the unit membrane capacitance and  $A_m$  is calculated as the ratio of the surface area (of the cylinder) to cell volume. The term in brackets is the sum of all ionic charges within the cell. This approach has the advantage that the initial voltage can be calculated without needing to assume a steady state as is required for by the derivative-based equivalent circuit or ‘Charge Sum’ equation (Fraser and Huang, 2004).

### 2.1.2 $Na^+/K^+$ -ATPase

$Na^+$  and  $K^+$  are transported actively by the  $Na^+/K^+$ -ATPase. In this model, an ATPase pump rate  $J_p$  was approximated by a cubic function dependent on the transmembrane sodium gradient, following Keener and Sneyd (2009):

$$J_p = P \left( \frac{[Na^+]_i}{[Na^+]_o} \right)^3 \quad (2.2)$$

where  $P$  is the pump rate constant and was fitted to produce ideal values for the intracellular ionic concentrations and membrane potential. Because it is a function of the sodium gradient,  $J_p$  decreases as  $[Na^+]_i$  depletes. Equation 2.2 has been shown to be similar to more accurate kinetic models reliant on both the  $Na^+$  gradient and ATP concentration (Keener and Sneyd, 2009). To further support the use of this formulation, I compared it to results employed using the less accurate linear formulation of the pump rate from Keener and Sneyd (2009),  $J_p = P \left( \frac{[Na^+]_i}{[Na^+]_o} \right)$ , as well a model by Hamada et al. (2003), based on experimental evidence fitted by Hill equations such that  $J_p = Q_{scale} \left( \frac{1.62}{1 + \left( \frac{6.7mM}{[Na^+]_i} \right)^3} + \frac{1.0}{1 + \left( \frac{67.6mM}{[Na^+]_i} \right)^3} \right)$ .  $Q_{scale}$  was set such that the same default steady state concentration of  $Na^+$  ions (and indeed of all ions) was achieved using any model.

To switch the ATPase pump on or off (Fig. 3.1 C),  $P$  was decreased / increased exponentially over 10-20 minutes, consistent with previous reports of the dynamics of inhibition of the ATPase by ouabain and in turn the inhibition of ouabain’s effects by potassium canrenoate (Baker and Willis, 1972; Yeh and Lazzara, 1973). The ATPase pumps 2  $K^+$  ions into the cell for every 3  $Na^+$  ions out; these constants were multiplied by  $J_p$  for each respective ion.

### 2.1.3 KCC2

$K^+$  and  $Cl^-$  concentrations were altered by flux through the type 2 K-Cl cotransporter (KCC2),  $J_{KCC2}$  (Doyon et al., 2016):

$$J_{KCC2} = g_{KCC2}(E_K - E_{Cl}) \quad (2.3)$$

where  $g_{KCC2}$  is a fixed conductance and  $E_K$  and  $E_{Cl}$  are the Nernst potentials for  $K^+$  and  $Cl^-$  respectively.  $J_{KCC2}$  is 0 when  $E_K = E_{Cl}$ . When KCC2 ‘strength’ was increased in the model (Fig. 3.3 B, 3.8 and 3.11 B), it was carried out by increasing  $g_{KCC2}$  in Equation 2.3. While the transporter is strictly electroneutral, I formulated  $g_{KCC2}$  as a conductance because  $J_{KCC2}$  was calculated as the flux per  $K^+$  or  $Cl^-$  ionic component.

As for the  $Na^+/K^+$ -ATPase, to support the principles behind the use of a formulation capturing the features of the KCC2 transporter as opposed to any particular model’s advantages, I compared my formulation to models from other sources:

- Raimondo et al. (2012) created a model derived using Michaelis-Menton kinetics and experiments, and incorporated new experimental values:  $J_{KCC2} = J_{scale} \cdot V_{max} \cdot \frac{[Cl^-]_i}{15mM + [Cl^-]_i} \left( \ln \frac{[K^+]_o \cdot [Cl^-]_o}{[K^+]_i \cdot [Cl^-]_i} \right) / \ln \frac{[K^+]_o \cdot [Cl^-]_o}{[K^+]_i \cdot 56mM}$ , where  $V_{max} = 5$  mM/s.
- The renal distal tubule was modeled by Lewin et al. (2012), and formulated  $J_{KCC2} = J_{scale} \cdot 0.3 \frac{[K^+]_o \cdot [Cl^-]_o - [K^+]_i \cdot [Cl^-]_i}{k_K \cdot k_{Cl} \left( \left( 1 + \frac{[K^+]_o \cdot [Cl^-]_o}{k_K \cdot k_{Cl}} \right) \left( 1 + \frac{[K^+]_i}{k_K} \right) \left( 1 + \frac{[Cl^-]_i}{k_{Cl}} \right) + \left( 1 + \frac{[K^+]_i \cdot [Cl^-]_i}{k_K \cdot k_{Cl}} \right) \left( 1 + \frac{[K^+]_o}{k_K} \right) \left( 1 + \frac{[Cl^-]_o}{k_{Cl}} \right) \right)}$ , where  $k_K = 9.0$  mM and  $k_{Cl} = 6.0$  mM.
- Finally, Fraser and Huang (2004) based their model on previous experimental evidence. Their equation for KCC2 follows:  $J_{KCC2} = J_{scale} \cdot P_K \cdot P_{KCC2} ([K^+]_o \cdot [Cl^-]_o - [K^+]_i \cdot [Cl^-]_i)$ , where  $P_K$  and  $P_{KCC2}$  are the permeability constants for  $K^+$  and the transporter respectively, the latter of which was tuned as needed in my use.

$J_{scale}$  for each model was set such that the same steady state concentrations were achieved using any model with the other parameters kept constant.

### 2.1.4 Permeable ion concentrations

Intracellular concentrations of the permeable ions  $Na^+$ ,  $K^+$  and  $Cl^-$  were updated individually by summing transmembrane fluxes, including those generated by the ATPase and KCC2. Leak currents were calculated using the standard equivalent circuit or Ohmic formulation,  $I = g(V_m - E_{ion})$ , where  $I$  is the current generated via conductance  $g$  multiplied by the driving force (the difference between the membrane potential and ion reversal potential). The values for  $g_{Na}$ ,  $g_K$  and  $g_{Cl}$  were chosen as near-median values from a search of values across models on ModelDB (McDougal et al., 2017) and Ion Channel Genealogy (Podlaski et al., 2017) (Table 2.2).

Reference	Cell	$g_{Na}$	$g_K$	$g_{Cl}$	Generic $g_{leak}$
Quadrone and Knöpfel (1994)	vestibular	10	10		500
Gentiletti et al. (2017)	hippocampal	30.2	133	59.6	
Menon et al. (2009)	hippocampal	5	50		
Somjen et al. (2008)	general	10	10	100	
Miocinovic et al. (2006)	subthalamic	8.1			
Keener and Sneyd (2009)	squid axonal	10	367		
Gabbiani et al. (1994)	granule	11.7			
Amini et al. (1999)	midbrain dopaminergic	16.3	83.7	0	
Cruz et al. (2007)	leech S	120	36	0.3	
Kager et al. (2000)	pyramidal / hippocampal	20	70		200
Kager et al. (2007)	pyramidal / hippocampal	54.8	137	52.8	

**Table 2.2:** Conductance values from computational models and papers designed to parameterise computational models of neurons in the literature. Conductances reported in  $\mu\text{S}/\text{cm}^2$ .

The rates of change of the intracellular concentrations of the three permeant ions were given by the following equations, with the Nernst potentials for each ion  $E_{ion} = \frac{RT}{zF} \ln \left( \frac{ion_{out}}{ion_{in}} \right)$ , w indicating the cell volume, and  $\frac{dw}{dt}$  as described in (2.7) or (2.9).

$$\frac{d[Na^+}_i = -\frac{A_m}{F}(g_{Na}(V_m - E_{Na}) + 3J_p) - \frac{1}{w} \frac{dw}{dt} [Na^+]_i \quad (2.4)$$

$$\frac{d[K^+]}{dt} = -\frac{A_m}{F}(g_K(V_m - E_K) - 2J_p - J_{KCC2}) - \frac{1}{w} \frac{dw}{dt} [K^+]_i \quad (2.5)$$

$$\frac{d[Cl^-]}{dt} = \frac{A_m}{F}(g_{Cl}(V_m - E_{Cl}) + J_{KCC2}) - \frac{1}{w} \frac{dw}{dt} [Cl^-]_i \quad (2.6)$$

### 2.1.5 Volume

Because the osmotic flux of water is expected to be faster than ion fluxes, the volume of the cell was adjusted to preserve transmembrane osmotic balance at each time step. Change in compartment volume, w, was calculated by changing the previous volume proportional to the difference between intracellular and extracellular osmolarity,  $\Pi_i$  and  $\Pi_o$  respectively (Hernández and Cristina, 1998), where  $v_w$  is the partial molar volume of water,  $p_w$  the osmotic permeability of a biological membrane and SA the surface area:

$$\frac{dw}{dt} = v_w \cdot p_w \cdot SA \cdot (\Pi_i - \Pi_o) \quad (2.7)$$

For the calculations in Figure 3.6 C-E, where I allowed transmembrane differences in osmolarity to develop, I assumed that at rest the cylindrical cell had a radius of  $r_a$  and zero pressure across the membrane, and that the tension in the membrane followed Hooke's law such that the tension was proportional to the difference between the dynamic circumference of the cell and that of the resting state. From Laplace's law and with  $k_m$  the spring constant of the membrane (Sachs and Sivaselvan, 2015), the hydrostatic pressure follows:

$$H_p = \begin{cases} 4\pi k_m \left( 1 - \frac{r_a}{r} \right) & : r > r_a \\ 0 & : r \leq r_a \end{cases} \quad (2.8)$$

Equation 2.7 was thus reformulated:

$$\frac{dw}{dt} = v_w \cdot p_w \cdot SA \cdot \left( \Pi_i - \Pi_o - \frac{H_p}{RT} \right) \quad (2.9)$$

In order to simulate extreme conditions of constrained volume, a larger  $k_m$  was employed than is realistic (Dai et al., 1998). Intracellular ion concentrations were updated again after volume change at each time step. Volume changes were manifested in the cylindrical compartment as change in the radius, except in Figure 3.10 B, when a change in height was employed. In the single compartment experiments, the cell was initialised with diameter 10  $\mu\text{m}$  and length  $l$  of 25  $\mu\text{m}$ .

### 2.1.6 Anion flux

Impermeant anions were manipulated in the compartment in Figures 3.4, 3.5, 3.6, 3.7, 3.9, 3.10 and 3.11 through several mechanisms. Anions were added to the compartment at a constant rate dependent on  $A_m$  and could either have the same average intracellular X charge  $z = -0.85$  (Fig. 3.4 C, 3.6 C, 3.7 B, 3.9 B and 3.10), or a different charge (Fig. 3.5 C, D, 3.6 A and 3.9 C). In these cases, the number of moles of X in the compartment was increased. Alternatively, the charge of a species of intracellular X was changed slowly imitating a charge-carrying transmembrane reaction (Fig. 3.5 A, 3.6 A, 3.7 A and 3.11 C). In this case, the number of moles of intracellular X did not change and it was assumed charge imbalance was mopped up by the extracellular milieu. Finally, extracellular  $X^-$  was changed in Figure 3.4 D by removing as much  $Cl^-$  as  $X^-$  was added, thus maintaining osmolarity and electroneutrality in the extracellular space, while in Figures 3.4 E and F,  $X^0$  and KCl respectively were added directly to the extracellular environment over time, increasing osmolarity but maintaining electroneutrality.

## 2.2 Multi-compartment model

The single compartment dendrite model was incorporated in a multi-compartment model by allowing electrodiffusion to occur between individual compartments operating as described above. Compartments were initialised with a radius of  $0.5 \mu m$  and height of  $10 \mu m$  unless otherwise specified (e.g. in Fig. 3.11). In the model, compartments were linked linearly without branching; a total length of 10 connected compartments was used. The time step  $dt$  was decreased to  $10^{-3} ms$  for simulations in multiple compartments. Christopher Currin, a PhD student from the Raimondo Lab, helped to develop the object-oriented environment necessary for the multi-compartment model. Code was written in Python 3 and is available on GitHub (<https://github.com/kiradust/model-of-neuronal-chloride-homeostasis>).

### 2.2.1 Electrodifusion

The Nernst-Planck equation (NPE) was used to model one-dimensional electrodifusion, based on (Qian and Sejnowski, 1989). The NPE incorporates fluxes because of diffusion and drift (i.e. the movement of ions driven by an electric field). It has been shown to be more accurate than using  $J_{diffusion}$  or  $J_{drift}$  alone in small structures like dendrites (Qian and Sejnowski, 1989). The NPE for  $J$  the flux density of ion  $C$  is calculated:

$$J = -D \frac{zF^2}{RT} [C] \frac{dV_m}{dx} - DF \frac{D[C]}{dx} \quad (2.10)$$

where  $D$  is the diffusion constant of ion  $C$  (Table 2.1),  $z$  is its charge,  $[C]$  is its concentration and  $x$  is the distance along the longitudinal axis over which electrodifusion occurs. The NPE was implemented between compartments  $i$  and  $i+1$ , assuming the  $i \rightarrow i+1$  direction is

positive, using a forward Euler approach. The midpoints of the compartment heights were used to calculate  $dx$ , i.e.  $dx = \frac{l_i+l_{i+1}}{2}$ , and the concentrations of  $C$  in each compartment were averaged to obtain  $J_{drift}$ , making sure that  $J_{i \rightarrow i+1} = J_{i+1 \rightarrow i}$ , where the fluxes had units of mol/(s·dm<sup>2</sup>):

$$J_{i \rightarrow i+1} = -D \left( \frac{zF}{RT} \frac{([C]_i + [C]_{i+1})}{2} \frac{dV_m}{dx} + \frac{d[C]}{dx} \right) \quad (2.11)$$

The flux was multiplied by the smallest shared surface area between adjacent compartments (i.e. the circle at the end of the cylinder with smallest radius) and then divided by compartment volume to determine the flux in terms of molar concentration (M/s), and finally implemented numerically with a forward Euler approach. The implementation mirrored that in (Qian and Sejnowski, 1989) for non-branching dendrites, but was adjusted for compartments whose volumes can change:

$$C_{i \rightarrow i+1} = -\frac{dt}{l_i} D \left( \frac{zF}{RT} \frac{([C]_i + [C]_{i+1})}{2} \frac{(V_{m_i} - V_{m_{i+1}})}{dx} + \frac{([C]_i - [C]_{i+1})}{dx} \right) \quad (2.12)$$

### 2.2.2 GABA<sub>A</sub> receptors

GABA<sub>A</sub>Rs were added to the multi-compartment model and could be activated on command (a ‘pulse’) in any compartment desired, simulating a type A GABAergic inhibitory synaptic input. The receptor responses were based on the synaptic receptor-binding models of Destexhe et al. (1994). The model differentiated between receptor states when the neurotransmitter (here *GABA*) was released and began to bind to a portion of GABA<sub>A</sub>Rs, as well as when the signal was stopped and the neurotransmitter became unbound from the receptors.

Before a pulse, the initial fraction of bound receptors was given by  $r_{initial}$ . When a pulse commenced, the transmitter concentration in the nearby area of the receptors was assumed to be maximal, and hence  $GABA_{max}$  was set to 1 mM. At time  $t$  since the pulse had been activated, the fraction of bound receptors  $r$  was given by:

$$r_t = r_\infty + r_{initial} \cdot e^{-\frac{t}{\tau_r}} \quad (2.13)$$

where  $r_\infty = \frac{\alpha GABA_{max}}{\alpha GABA_{max} + \beta}$  and  $\tau_r = \frac{1}{\alpha GABA_{max} + \beta}$ , in which  $\alpha = 0.5 \text{ ms}^{-1}\text{mM}^{-1}$  and  $\beta = 0.1 \text{ ms}^{-1}$  are the forward and backward rate constants for transmitter binding respectively.

Pulses were generally on for 2 ms in my model. After a pulse, at time  $t_{end}$ ,  $[GABA]$  was set to 0 and then the fraction of bound receptors  $r$  was re-calculated:

$$r_{t-t_{end}} = r_{t_{end}} \cdot e^{-\beta(t-t_{end})} \quad (2.14)$$

The fraction of bound receptors at the appropriate timepoint from Equation 2.13 or 2.14 was multiplied in the Ohmic equation. It was assumed that the Cl<sup>-</sup> component of the

GABA reversal potential was responsible for the whole current generated by the pulse, i.e.  $I_{GABA} = g_{synapse} \cdot r_t(V_m - E_{GABA}) \approx g_{synapse} \cdot \frac{4}{5}r_t(V_m - E_{Cl^-})$ . The conductance  $g_{synapse}$  was set to 1 nS. The current  $I_{GABA}$  was converted to a change in moles of  $Cl^-$  per second in the compartment manipulated, which was finally calculated as a concentration and  $[Cl^-]_i$  was adjusted.

In Figure 3.11, the multi-compartment model was initiated with a morphology resembling a ‘ball-and-stick’ set-up (soma and dendrite). The 9 compartments making up the dendrite were each cylinders with radii of 0.5  $\mu m$  and heights of 10  $\mu m$ . The soma was a cylinder with radius 2  $\mu m$  and height 40  $\mu m$  — it had a volume 64 times greater than the volume in each of the compartments making up the dendrite. The synapse for each iteration was located in the second compartment of the dendrite, the same compartment that was first manipulated to either increase KCC2 strength or change the average charge of the compartment’s impermeant anions, following the methods described before for each process.

## 2.3 Systematic review

A literature search was performed to identify experimental studies that aimed to correlate a change in KCC2 expression with changes in  $[Cl^-]_i$ . The MEDLINE database was used and accessed via the PubMed online platform. Search terms included ‘chloride’, ‘ $Cl^-$ ’, ‘intracellular’, ‘KCC2’, ‘cotransporter’, ‘neuronal’, ‘GABA’ using appropriate Boolean operators. All 26 studies that demonstrated changes in KCC2 expression and  $E_{GABA}$  were considered for the meta-analysis. As there is a well described differential expression of KCC2 and NKCC1 at different stages of development, with KCC2 expression increasing and NKCC1 expression decreasing across development (Ben-Ari, 2002), only studies that used tissue older than postnatal day 7 were included (8 included data from younger animals). Other exclusion criteria included: reporting a significant change in NKCC1 (5 studies); use of non-rodent tissue (2 studies); no quantification of the change in KCC2 (2 studies).

Nine experiments from eight studies met all criteria and were included (Coull et al., 2003; Lagostena et al., 2010; Lee et al., 2011; Ferrini et al., 2013; Campbell et al., 2015; MacKenzie and Maguire, 2015; Mahadevan et al., 2015; Tang et al., 2015). However, one study did not report any change in  $V_m$  and hence was excluded from Figure 3.3 D (Mahadevan et al., 2015). Data used in regression can be seen in Table 3.1 and includes the analysis for regression against change in  $[Cl^-]_i$ . To accommodate varied experimental preparations and techniques influencing data quality and biases, a 34-point scoring system was designed to weight the studies (Table 2.3). A weighted least squares regression model was then used to correlate the percentage (%) change in KCC2 expression versus change in  $Cl^-$  driving force.

The literature review, data scraping and weighting score generated per experiment was validated by two separate investigators, myself and Dr Richard Burman. I wrote and implemented the regression model using Python 2. The code is available on GitHub (<https://github.com/kiradust/model-of-neuronal-chloride-homeostasis>).

Category		Score
<b>Experimental preparation</b>		
Region	<i>Cortical brain tissue</i>	2
	<i>Spinal cord tissue</i>	1
Technique used	<i>Acute tissue slice</i>	3
	<i>Organotypic tissue slice culture</i>	2
	<i>Dissociated cell culture</i>	1
<b>KCC2 expression data</b>		
Technique used to measure KCC2 expression	<i>RT-PCR</i>	3
	<i>Immunoblotting</i>	2
	<i>Immunohistochemistry</i>	1
Change in KCC2 expression	<i>Stated in-text</i>	2
	<i>Extracted from graphic</i>	1
Sample size	$\geq 21$	4
	10 – 20	3
	5 – 9	2
	$\leq 4$	1
<b>NKCC1 expression data</b>		
Technique used to measure NKCC1 expression	<i>RT-PCR</i>	3
	<i>Immunoblotting</i>	2
	<i>Immunohistochemistry</i>	1
Change in NKCC1 expression	<i>Stated in-text</i>	10
	<i>Extracted from graphic</i>	8
	<i>None</i>	0
Sample size	$\geq 21$	4
	10 – 20	3
	5 – 9	2
	$\leq 4$	1
<b>E<sub>GABA</sub> data</b>		
Technique used to measure E <sub>GABA</sub>	<i>Gramicidin perforated patch-clamp</i>	4
	<i>Whole-cell patch-clamp</i>	1
Change in E <sub>GABA</sub> expression	<i>Stated in-text</i>	4
	<i>Extracted from graphic</i>	1
Sample size	$\geq 21$	4
	10 – 20	3
	5 – 9	2
	$\leq 4$	1

**Table 2.3:** Scoring system used to weight studies for the least squares regression meta-analysis in Figure 3.3 D.

# Chapter 3

## Results

### 3.1 A single compartment model using the pump-leak formulation is suitable to test chloride homeostatic mechanisms

To compare the putative determinants of chloride homeostasis, a single compartment biophysical model was developed on the basis of the pump-leak formulation (Tosteson and Hoffman, 1960; Kay, 2017) (Fig. 3.1 A). The pump-leak model is a system of differential equations describing key cellular features: the  $\text{Na}^+/\text{K}^+$ -ATPase, passive transmembrane ionic flux of the major cellular ions based on their electrochemical gradient ( $\text{K}^+$ ,  $\text{Cl}^-$  and  $\text{Na}^+$ ), impermeant anions X with average charge z, and the membrane potential  $V_m$  are included (see Methods for details). I used a sodium-potassium ATPase with pump rate  $J_p$  modified by the transmembrane sodium gradient,  $J_p = p \cdot \left( \frac{[\text{Na}^+]_i}{[\text{Na}^+]_o} \right)^3$  (Equation 2.2, Methods), which is more accurate than simpler constant or linear models of the ATPase (Keener and Sneyd, 2009). Volume (w), osmolarity ( $\Pi$ ) and cation-chloride cotransporters, in this case KCC2, could be added to the model in a natural way. My KCC2 model had a conductance  $g_{\text{KCC}2}$  and driving force proportional to the difference in the Nernst reversal potentials of potassium and chloride  $J_{\text{KCC}2} = g_{\text{KCC}2}(E_K - E_{\text{Cl}})$  (Equation 2.3, Methods) (Doyon et al., 2016).

To justify that the pump-leak model was a sufficient testing ground for my comparison of mechanisms affecting the  $\text{Cl}^-$  driving force, it needed to replicate normal cellular conditions (Section 3.1.1). Aiding my evaluation, an analytical solution was found for the model that allowed me to readily calculate steady state values given a range of starting conditions (Section 3.1.2).

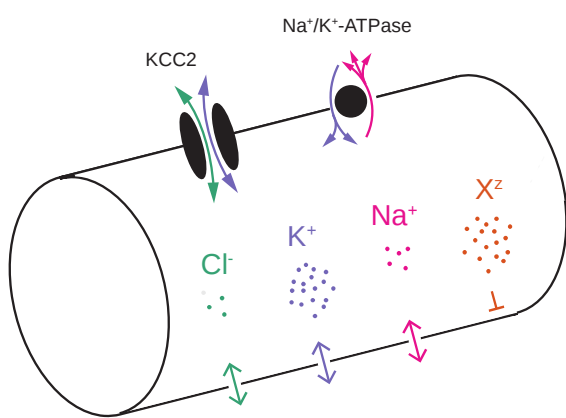
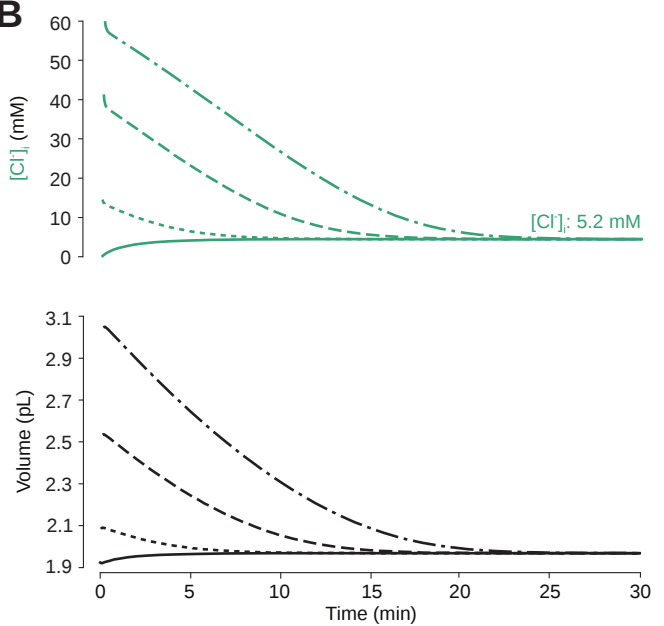
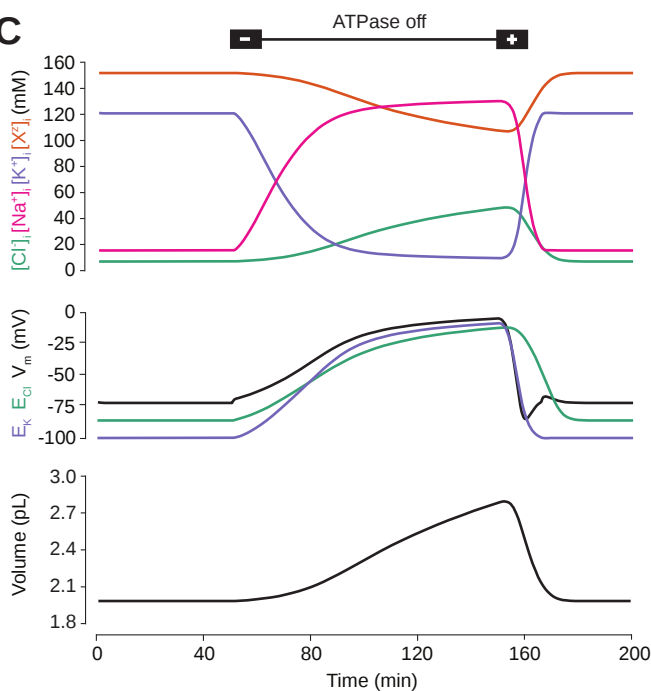
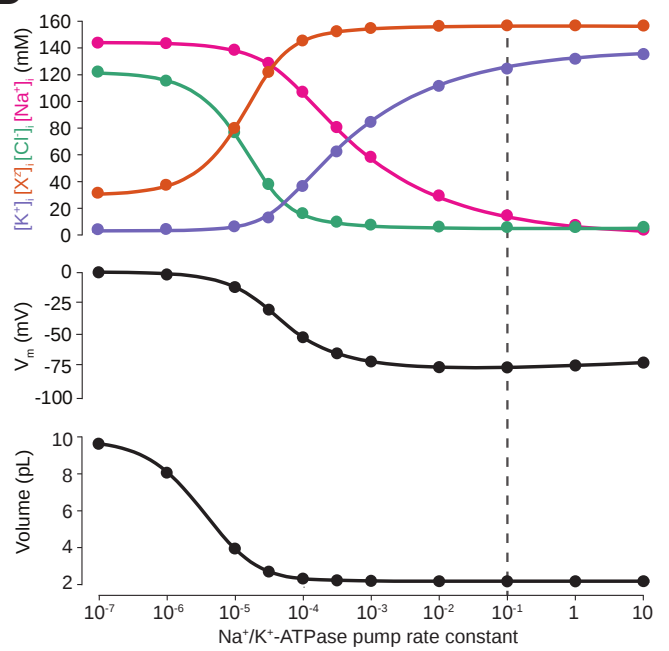
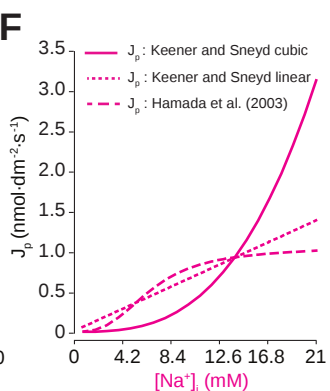
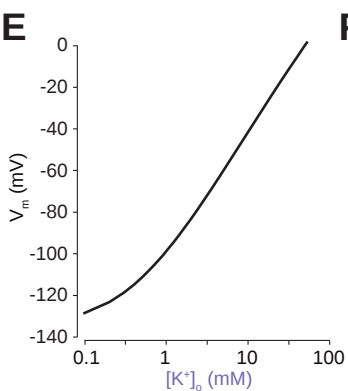
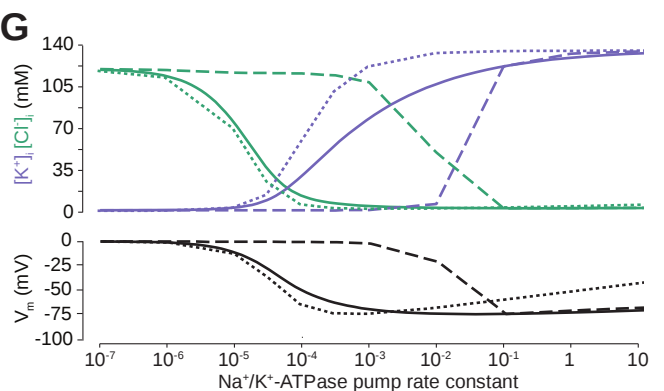
### 3.1.1 The pump-leak model demonstrates the importance of the $\text{Na}^+ \text{-K}^+$ ATPase in ionic homeostasis

The single compartment model that I developed included all relevant cellular parameters, based on the pump-leak formulation (Tosteson and Hoffman, 1960; Kay, 2017) (Fig. 3.1 A). Permeable ions could move across the cellular membrane via passive conductances according to each ion's respective electrochemical gradient. Impermeant ions had average charge  $z$  of -0.85 unless otherwise stated, as extrapolated from reasonable cellular ionic concentrations and osmolarity (Lodish et al., 2009; Raimondo et al., 2015). Active transport of  $\text{Na}^+$  and  $\text{K}^+$  by the  $\text{Na}^+/\text{K}^+$ -ATPase with a default pump rate constant of  $0.1 \text{ C}/(\text{dm}^2 \cdot \text{s})$  and cotransport of  $\text{Cl}^-$  and  $\text{K}^+$  by the cation-chloride cotransporter KCC2 with a non-zero conductance  $g_{\text{KCC}2}$  of  $20 \mu\text{S}/\text{cm}^2$  were also included (Doyon et al., 2016).

The model's default steady state had ion concentrations and membrane potentials that approximate those experimentally observed in mature neurons:  $\text{Cl}^-$  5 mM;  $\text{K}^+$  123 mM;  $\text{Na}^+$  14 mM;  $\text{X}^z$  155 mM; and a  $V_m$  of -72.6 mV (Jiang and Haddad, 1991; Tyzio et al., 2008). The model is robust in that initial values do not determine the steady state conditions. Regardless of initial starting concentrations of permeant or impermeant ions, cell volume or  $V_m$ , the model converged to the same stable fixed points for the ion concentrations and  $V_m$  without needing to include any means for 'sensing' ion concentration, volume or voltage.

---

**Figure 3.1 (facing page):** A biophysical model of ion dynamics based on the pump-leak mechanism demonstrates the importance of the sodium-potassium ATPase for setting transmembrane ion gradients including chloride. **(A)** A single cell compartment was modelled as a cylinder with volume changes equivalent to changes in cylindrical radius. Dynamics of membrane permeable potassium (purple,  $\text{K}^+$ ), sodium (pink,  $\text{Na}^+$ ) and chloride (green,  $\text{Cl}^-$ ) ions were included. Impermeant anions (orange,  $\text{X}^z$ ) had an average intracellular charge  $z$ . The KCC2 transporter moved  $\text{Cl}^-$  and  $\text{K}^+$  in equal parts according to the transmembrane gradient for the two ions. The sodium-potassium ATPase transported 3  $\text{Na}^+$  ions out for 2  $\text{K}^+$  ions moved into the cell. **(B)** Regardless of intracellular starting concentrations of the permeable ions, the model converged to identical steady state values for all parameters without needing to include any means for 'sensing' ion concentration, volume or voltage. I show the result for  $\text{Cl}^-$  as a time series of  $[\text{Cl}^-]_i$  (top panel) and volume (bottom panel). **(C)** The ATPase plays a key role in maintaining steady state ion concentration, membrane voltage ( $V_m$ ) and volume. Switching off the ATPase results in a continuous increase in cell volume (bottom panel), membrane depolarisation (middle panel) and ion concentration dysregulation (top panel) with colours per ion as in **A**. All cellular parameters recovered when the ATPase was reactivated. **(D)** The model's analytic solution showed exact correspondence with steady state values generated by numerical, time series runs (dots) for varying ATPase pump rates. Steady state values for the concentrations of the ions with colours as in **A** (top panel);  $V_m$  (middle panel) and volume (bottom panel). The dashed line indicates the default ATPase pump rate used in all simulations unless specified otherwise. **(E)** The pump-leak model replicates the classic membrane potential dependence on extracellular potassium,  $[\text{K}^+]_o$ . **(F)** Comparison of pump rate of different ATPase models against input sodium concentration. The cubic model by Keener and Sneyd (2009) (solid line) is the default model used. The Keener and Sneyd (2009) linear model (dotted line) and Hamada et al. (2003) method (dashed line) were normalised such that the same steady state concentration of  $\text{Na}^+$  ions (and indeed of all ions) was achieved using all models. These models do not scale pump rate as robustly with increasing sodium concentration as does the cubic model. **(G)** Comparison of  $\text{K}^+$ ,  $\text{Cl}^-$  and  $V_m$  for the cubic (solid line), linear (dotted line) and Hamada et al. (2003) (dashed line) models over varying constant pump rate. The linear model depolarises  $V_m$  at high pump rates while the Hamada et al. (2003) curve is shifted to the right.

**A****B****C****D****E****F**

In the case of permeable ions, initial concentrations also did not determine the final cellular volume. For example, despite initiating the model with different starting concentrations of  $\text{Cl}^-$  (1, 15, 40 and 60 mM respectively, Fig. 3.1 B), the  $[\text{Cl}^-]_i$  always converged to the same stable concentration of 5.2 mM, a typical baseline  $[\text{Cl}^-]_i$  for adult neurons, and volume always converged to 2.0 pL, a typical volume for hippocampal neurons (Ambros-Ingerson and Holmes, 2005).

Consistent with previous results (Xiao et al., 2002; Dierkes et al., 2006; Dijkstra et al., 2016), restricting the activity of the  $\text{Na}^+/\text{K}^+$ -ATPase in the model caused progressive collapse of transmembrane ion gradients, membrane depolarisation and cell swelling (Fig. 3.1 C). These effects were reversed when the pump was reconstituted. Indeed, the  $\text{Na}^+/\text{K}^+$ -ATPase sets the steady state concentrations of permeant and impermeant ions,  $V_m$  and volume (Fig. 3.1 D). When I increased the activity of the  $\text{Na}^+/\text{K}^+$ -ATPase in my model, the final steady-state concentration for  $\text{K}^+$  increased, while  $\text{Na}^+$  and  $\text{Cl}^-$  dropped to levels that approximate those observed in mature neurons (Fig. 3.1 D). At the same time, the final, stable-state membrane potential and cell volume also decreased. Interestingly, as has been observed previously (Fraser and Huang, 2004), beyond a certain level, further increases in the pump rate have negligible effects on volume and  $V_m$ .

In further support of the validity of my model as representative of normal neuronal biophysics, I was able to replicate the classic dependence of membrane potential on  $[\text{K}^+]_o$  (Fig. 3.1 E).  $V_m$  increased initially non-linearly with logarithmic increase in  $[\text{K}^+]_o$ , concurring with experimental results, rather than increasing only linearly, as would be expected with a simple Nernst potential model (Forsythe and Redman, 1988).

Other formulations of the ATPase and KCC2 were compared in time-dependent simulations and found to have no impact on the requirements for the biophysical model. I considered both a Hill equation-based experimentally-matched model by Hamada et al. (2003) and a linear model by Keener and Sneyd (2009), as opposed to the cubic model that I employed. Although these models had different kinetics (Fig. 3.1 F), when normalised to the same effective pump rate, they produced the same steady state values for ion concentrations, membrane potential and volume. In addition, when employing the models of the ATPase, the final steady state concentrations of the permeant ions were again not affected by their initial concentrations (Fig. 3.1 B).

Interestingly, the models produced slightly different steady states dependent on the pump rate constant, with the Hamada et al. (2003) model having a tighter range in which large changes in ion concentrations and membrane potential occurred, and the linear model also displaying a tight curve as well as progressive membrane depolarisation at high pump rates, as predicted by Keener and Sneyd (2009) (Fig. 3.1 G). The cubic model has the advantage of an analytical solution, which allowed me to rapidly explore the influence of various parameters on steady state values.

### 3.1.2 An analytical solution can evaluate steady state conditions of the pump-leak model

To quickly and extensively evaluate conditions at steady state, I wanted to find analytical solutions for the variables in the pump-leak formulation for a single compartment including KCC2 and the  $\text{Na}^+/\text{K}^+$ -ATPase: intracellular ionic concentrations ( $[\text{Na}^+]_i$ ,  $[\text{K}^+]_i$ ,  $[\text{Cl}^-]_i$ ,  $[\text{X}^z]_i$ ); and membrane voltage ( $V_m$ ). The steady state should occur in the presence of activity of both a pump-leak mechanism, that is the  $\text{Na}^+/\text{K}^+$ -ATPase, and  $\text{Cl}^-/\text{K}^+$ -extrusion. Allowing for an analytical solution inclusive of differences in osmolarity between the intracellular and extracellular environments, I derived the analytical solution such that  $\Pi_i = \Pi_o + N_{H_p}$ , where  $\Pi_i$  is the intracellular osmolarity and  $\Pi_o$  the extracellular. Thus  $N_{H_p}$  is equal to 0 when there is no osmotic difference across the cellular membrane, and non-zero otherwise.

The situation described ought to satisfy the following five equations at steady state (see Methods), in which the conductance of an ion is denoted  $g_{ion}$ , an ion's Nernst reversal potential as  $E_{ion}$ ,  $F$  the Faraday constant and  $A_m$  the ratio of surface area to volume. The first three equations describe the permeant ion concentrations' rates of change because of the sum of fluxes each experiences (electrochemical/'passive' for all three, secondary to the ATPase in the case of  $\text{Na}^+$  and  $\text{K}^+$ , and secondary to KCC2 in the case of  $\text{K}^+$  and  $\text{Cl}^-$ ; see Methods, Section 2.1.4):

$$-\frac{d}{dt}\left(\frac{F}{A_m}[\text{Na}^+]_i\right) = g_{\text{Na}}(V_m - E_{\text{Na}}) + 3J_p \quad (\text{A1})$$

$$-\frac{d}{dt}\left(\frac{F}{A_m}[\text{K}^+]_i\right) = g_K(V_m - E_K) - 2J_p - g_{\text{KCC2}}(E_K - E_{\text{Cl}}) \quad (\text{A2})$$

$$\frac{d}{dt}\left(\frac{F}{A_m}[\text{Cl}^-]_i\right) = g_{\text{Cl}}(V_m - E_{\text{Cl}}) + g_{\text{KCC2}}(E_K - E_{\text{Cl}}) \quad (\text{A3})$$

Charge neutrality is coded in (A4), which assumes that the constant extracellular charges always sum to zero and the variable intracellular charges should sum near zero at steady state:

$$0 = [\text{K}^+]_i + [\text{Na}^+]_i - [\text{Cl}^-]_i + z[\text{X}^z]_i \quad (\text{A4})$$

The transmembrane osmotic balance is coded in (A5).  $N_{H_P}$  can be non-zero when the contribution of membrane tension causes an osmotic difference to develop (Equation 2.9):

$$\Pi_o + N_{H_p} = \Pi_i = [\text{K}^+]_i + [\text{Na}^+]_i + [\text{Cl}^-]_i + [\text{X}^z]_i \quad (\text{A5})$$

I first solved the system for constant  $J_p$  at steady state, i.e. Equations A1, A2 and A3 set to 0, and then showed that a parametric solution exists for  $p$  such that the function mapping  $J_p$  to  $p$  is bijective. Thus I began by solving each of (A1), (A2) and (A3) for the reversal potential of the intracellular ion that they refer to, and then for the intracellular ions' concentration itself. I walk through the derivation below, which is an extension of the work on a similar system of equations by Keener and Sneyd (2009).

By rearrangement,

$$[Na^+]_i = [Na^+]_o \cdot e^{-\frac{FV_m}{RT}} \cdot e^{-\frac{3J_p F}{RT g_{Na}}} \quad (\text{A6})$$

and

$$E_{Cl} = \frac{g_{Cl} V_m + g_{KCC2} E_K}{g_{Cl} + g_{KCC2}} \quad (\text{A7})$$

Let  $\beta$  be equal to  $g_{KgCl} - g_{KCC2}G_{Cl} + g_{KgKCC2}$ . Substituting (A7) into (A2) for  $E_{Cl}$ , one can solve for  $E_K$  and  $[K^+]_i$ , hence enabling substitution back into (A7) in order to solve for  $[Cl^-]_i$ .

Thus,

$$E_K = V_m - 2J_p \frac{g_{Cl} + g_{KCC2}}{\beta}$$

and hence

$$[K^+]_i = [K^+]_o \cdot e^{-\frac{FV_m}{RT}} \cdot e^{\frac{F}{RT} \cdot 2J_p \frac{g_{Cl} + g_{KCC2}}{\beta}} \quad (\text{A8})$$

so then

$$[Cl^-]_i = [Cl^+]_e \cdot e^{\frac{FV_m}{RT}} \cdot e^{-\frac{F}{RT} \cdot \frac{2J_p \cdot g_{KCC2}}{\beta}} \quad (\text{A9})$$

Thus equations for all permeant intracellular ions in terms of constants and  $V_m$  are derived. An extension of these results means that one can find an equation for  $[X^z]_i$  in terms of  $V_m$  by rearranging the osmotic equilibrium equation (A5):

$$[X^z]_i = (\Pi_o + N_{H_p}) - [Na^+]_i - [K^+]_i - [Cl^-]_i \quad (\text{A10})$$

In order to solve for  $V_m$ , substitute (A10) into (A4), the equation that assures intracellular charge neutrality. Thus:

$$0 = z \cdot (\Pi_o + N_{H_p}) + (1 - z) \cdot ([K^+]_i + [Na^+]_i) - (1 + z) \cdot [Cl^-]_i \quad (\text{A11})$$

Before substituting in for the permeable intracellular ions, denote  $\theta = e^{-\frac{FV_m}{RT}}$ . Then with substitution of (A9), (A8) and (A6) and multiplication through by  $\theta$  Equation A11 becomes:

$$0 = (1 - z) \cdot \left( [K^+]_o \cdot e^{\frac{2J_p F \cdot (g_{Cl} + g_{KCC2})}{RT \cdot \beta}} + [Na^+]_o \cdot e^{-\frac{3J_p F}{RT \cdot g_{Na}}} \right) \cdot \theta^2 + z \cdot (\Pi_o + N_{H_p}) \cdot \theta - (1 + z) \cdot [Cl^-]_o \cdot e^{\frac{-2J_p F \cdot g_{KCC2}}{RT \cdot \beta}}$$

This quadratic equation can be solved in terms of  $\theta$  using the quadratic formula.

$$\theta = \frac{-z \cdot (\Pi_o + N_{H_p}) + \sqrt{z^2 \cdot (\Pi_o + N_{H_p})^2 + 4(1 - z^2) \cdot [Cl^-]_o \cdot e^{-\frac{2J_p F \cdot g_{KCC2}}{RT \cdot \beta}} \cdot \left( [Na^+]_o \cdot e^{-\frac{3J_p F}{RT \cdot g_{Na}}} + K_e \cdot e^{\frac{2J_p F \cdot (g_{Cl} + g_{KCC2})}{RT \cdot \beta}} \right)}}{2 \cdot (1 - z) \cdot \left( [Na^+]_o \cdot e^{-\frac{3J_p F}{RT \cdot g_{Na}}} + [K^+]_o \cdot e^{\frac{2J_p F \cdot (g_{Cl} + g_{KCC2})}{RT \cdot \beta}} \right)} \quad (\text{A12})$$

From this one can solve the system for any constants — at least those constants which give positive real solutions for  $\theta$  — and then use  $V_m = -\frac{RT}{F} \ln \theta$  to transform the solution

into the corresponding membrane voltage. Note that when  $z = -1$ , to avoid division by 0, the solution is found by substituting  $z = -1$  into (A11) and simplifying.

Finally, I extended the solution from the constant pump rate assumed above to a pump rate modulated by the sodium concentration, as used in the model. The sodium-dependent pump rate updated by  $J_p = p \cdot \left( \frac{[Na^+]_i}{[Na^+]_o} \right)^3$  cannot be solved purely analytically in the reals because it has the form of a *W-Lambert Function* (Corless et al., 1996). In this case, one might substitute different values of  $J_p$  into the solution above, and then use the function  $f(J_p, [Na^+]_i)$  defined by  $J_p = p \cdot \left( \frac{[Na^+]_i}{[Na^+]_o} \right)^3$  to solve for  $p$ .

$f$  rearranged with  $p$  as the subject of the formula resembles a parametric function. Were  $p$  an independent variable determining the ionic solutions of the analytic solution, each simulation beginning with constant  $p$  would have a unique steady state. To make this claim, the function mapping  $J_p$  and the steady state  $[Na^+]_i$  to  $p$  needs to be injective (more strictly,  $f : J_p \rightarrow p$  must be bijective). The reason for this constraint is that if ever a  $p$  is produced by more than one  $J_p$  and  $[Na^+]_i$ , there would be at least two possible steady states for the time series run with that pump rate constant, and thus an incomplete mapping between the constant pump rate solution and the cubic pump rate solution.

Indeed, the mapping between  $p$  and  $J_p$  is found to be bijective over the range over  $J_p$  used in my model, by numerical methods. This proves that the analytic solution derived here is sufficient for finding a parametric solution for the more accurate cubic pump rate ATPase model used in my thesis. In addition, there was a direct correspondence between time-dependent simulations until steady state and the analytical solution predictions at the same pump rates, confirming the validity of the solution (Fig. 3.1 D).

The solution implies that initial values of the intracellular ion concentrations do not affect the final steady state, since the solutions are not dependent on time-dependent concentration values (Fig. 3.1 B), but that the parameters  $\Pi_o$ ,  $N_{H_p}$ ,  $J_p$ , ionic conductances,  $z$  and extracellular concentrations may all contribute to steady state shifts. In subsequent analyses, this novel analytic solution allowed me to rapidly explore a large parameter space to determine how various cellular attributes might affect  $Cl^-$  homeostasis.

## 3.2 Chloride cotransport modulates chloride driving force

### 3.2.1 Membrane chloride conductance affects steady-state intracellular chloride concentration only in the presence of active cation-chloride cotransport

Using the analytic solution, I investigated how changes in baseline ion conductance for the major ions in my model ( $g_K$ ,  $g_{Na}$  and  $g_{Cl}$ ) affected  $Cl^-$  homeostasis. I calculated the steady-state values for the  $Cl^-$  reversal potential ( $E_{Cl}$ ) and potassium reversal potential ( $E_K$ ), resting membrane potential ( $V_m$ ) and volume ( $w$ ) while independently manipulating the conductance for each ion (Fig. 3.2). Increasing the baseline potassium conductance ( $g_K$ ) resulted in  $E_{Cl}$ ,  $E_K$  and  $V_m$  converging to similar steady-state values (Fig. 3.2 A)

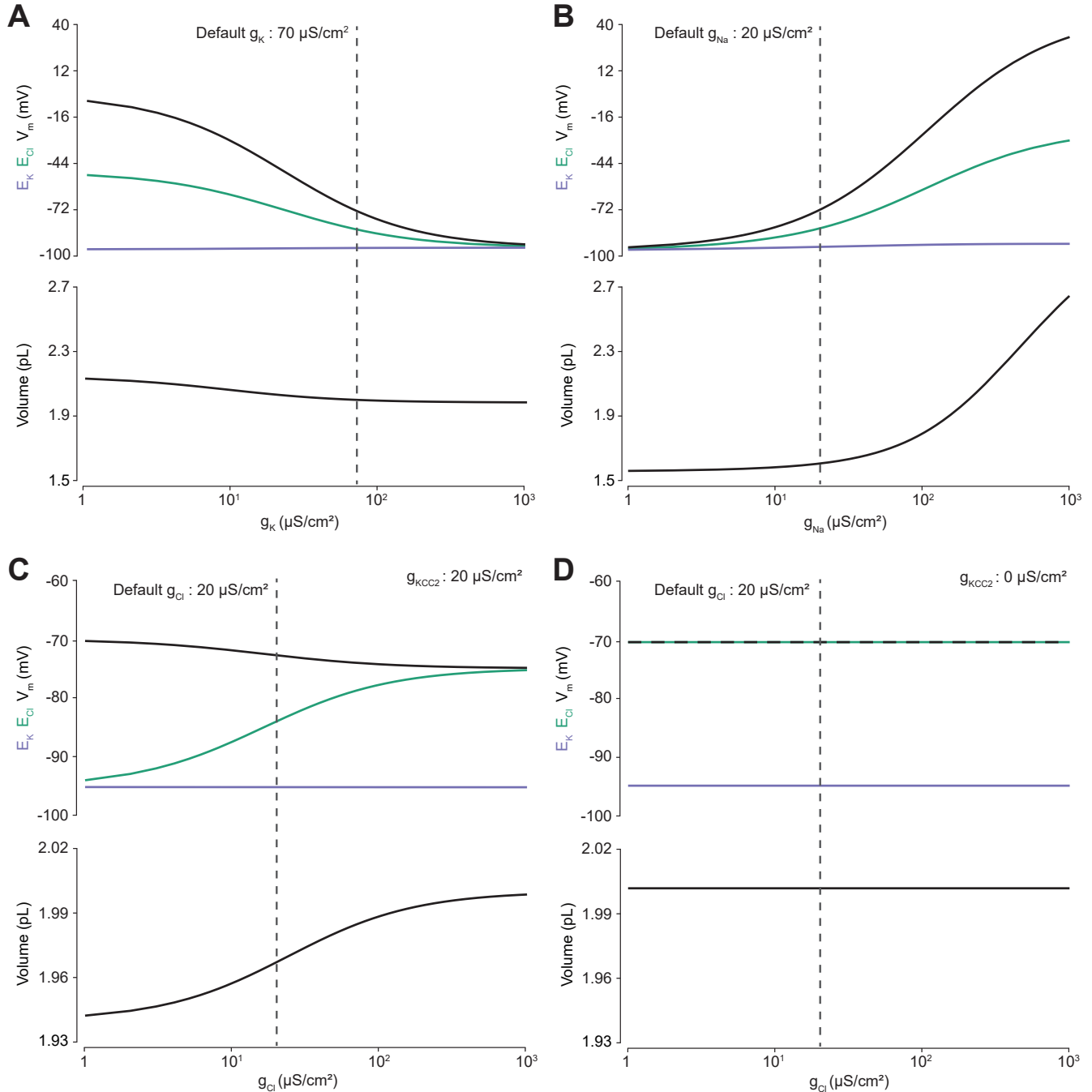


**Figure 3.2:** Membrane chloride conductance affects steady-state intracellular chloride concentration only in the presence of active cation-chloride cotransport. Steady state values for different ionic conductance were calculated using the model's analytic solution. **(A)** Steady state  $E_{\text{Cl}}$  (green),  $E_K$  (purple),  $V_m$  (black) and volume  $w$  (bottom panel) were calculated at different  $\text{K}^+$  conductances ( $g_K$ ). Increasing  $g_K$  resulted in a convergence of steady state  $E_{\text{Cl}}$ ,  $E_K$  and  $V_m$ . **(B)** Increasing  $\text{Na}^+$  conductance  $g_{\text{Na}}$  resulted in a progressive increase in steady state  $E_{\text{Cl}}$ ,  $E_K$  and  $V_m$  with accompanying cell swelling. **(C)** In the presence of active cation-chloride cotransport ( $g_{\text{KCC2}} = 20 \mu\text{S}/\text{cm}^2$ ), increasing  $\text{Cl}^-$  conductance shifted steady state  $E_{\text{Cl}}$  from  $E_K$  toward  $V_m$ . **(D)** In the absence of KCC2 activity,  $g_{\text{Cl}}$  had no effect on steady state parameters.  $E_{\text{Cl}}$  equals  $V_m$  in all instances. Dashed lines indicate the default values for  $g_K$ ,  $g_{\text{Na}}$  and  $g_{\text{Cl}}$ .

without significantly affecting cell volume. In contrast, increasing the baseline sodium conductance ( $g_{Na}$ ) beyond  $20 \mu\text{S}/\text{cm}^2$  resulted in a steady depolarisation of  $E_{Cl}$ ,  $E_K$  and  $V_m$  with accompanying cell swelling (Fig. 3.2 B).

The effect of manipulating  $\text{Cl}^-$  conductance ( $g_{Cl}$ ) depended on the activity of concurrent cation-chloride cotransport by KCC2 (Fig. 3.2 C). In the presence of active KCC2 at very low values of  $g_{Cl}$ , the steady state  $[\text{Cl}^-]_i$  is such that  $E_{Cl}$  approaches  $E_K$ . This follows because in the absence of alternative  $\text{Cl}^-$  fluxes, KCC2 utilises the transmembrane potassium gradient to transport  $\text{Cl}^-$  until  $E_{Cl}$  equals  $E_K$ . With increasing  $g_{Cl}$  however,  $E_{Cl}$  increases, moving away from  $E_K$  towards  $V_m$ , and at very high  $\text{Cl}^-$  conductances  $E_{Cl}$  and  $V_m$  approached similar values in my model. Without the activity of KCC2,  $g_{Cl}$  had no effect on steady state  $E_{Cl}$ ,  $E_K$ ,  $V_m$  or volume, with  $g_{Cl}$  able to be very low but greater than zero (Fig. 3.2 D). In this instance,  $E_{Cl}$  always equals  $V_m$  as the movement of  $\text{Cl}^-$  across the membrane is purely passive. Without the activity of KCC2, there can be no driving force for  $\text{Cl}^-$  flux at steady state ( $V_m - E_{Cl} = 0$ ). My model therefore behaved in a manner consistent with established theoretical predictions (Kaila et al., 2014).

### 3.2.2 Cation-chloride cotransport sets the chloride reversal and driving force for transmembrane chloride flux

Next, I used the single-cell model to explore how the activity of cation-chloride cotransport affects  $\text{Cl}^-$  homeostasis. Since  $\text{Cl}^-$  cotransport by KCC2 depends on the transmembrane gradient for  $K^+$ , which in turn is established by the  $\text{Na}^+/\text{K}^+$ -ATPase, I explored how the  $\text{Na}^+/\text{K}^+$ -ATPase pump rate affected  $E_{Cl}$  in the presence of KCC2 activity ( $g_{KCC2} = 20 \mu\text{S}/\text{cm}^2$ ). As depicted in Fig. 3.3 A, the  $\text{Na}^+/\text{K}^+$ -ATPase pump is a critical determinant of intracellular  $\text{Cl}^-$  homeostasis. Of interest, above a pump rate constant of  $10^{-3}$ , when cell volume is stable, many fold changes in pump rate have minimal effects on  $E_{Cl}$  and  $V_m$ . It therefore seems unlikely that neurons would adjust the  $\text{Na}^+/\text{K}^+$ -ATPase to modulate  $\text{Cl}^-$  driving force.

In my model, the activity of KCC2 was set by the conductance of KCC2 ( $g_{KCC2}$ ). Using the numerical formulation with the default values described in Figure 3.1 and 3.2, I steadily increased  $g_{KCC2}$  from  $20 \mu\text{S}/\text{cm}^2$  to  $370 \mu\text{S}/\text{cm}^2$  and tracked changes to  $E_{Cl}$ ,  $E_K$ ,  $V_m$  and volume. Increasing KCC2 activity over time caused a steady decrease in  $[\text{Cl}^-]_i$  of  $1.7 \text{ mM}$  to  $3.5 \text{ mM}$  reflected by the hyperpolarisation of  $E_{Cl}$  (Fig. 3.3 B).  $V_m$  decreased only modestly, resulting in an increase in the driving force for  $\text{Cl}^-$  flux that tracked the increase in  $g_{KCC2}$ . This effect saturates since  $E_K$  constitutes a lower bound on  $E_{Cl}$ . Importantly, increases in  $g_{KCC2}$  resulted in persistent changes to  $E_{Cl}$  and the driving force for  $\text{Cl}^-$ .

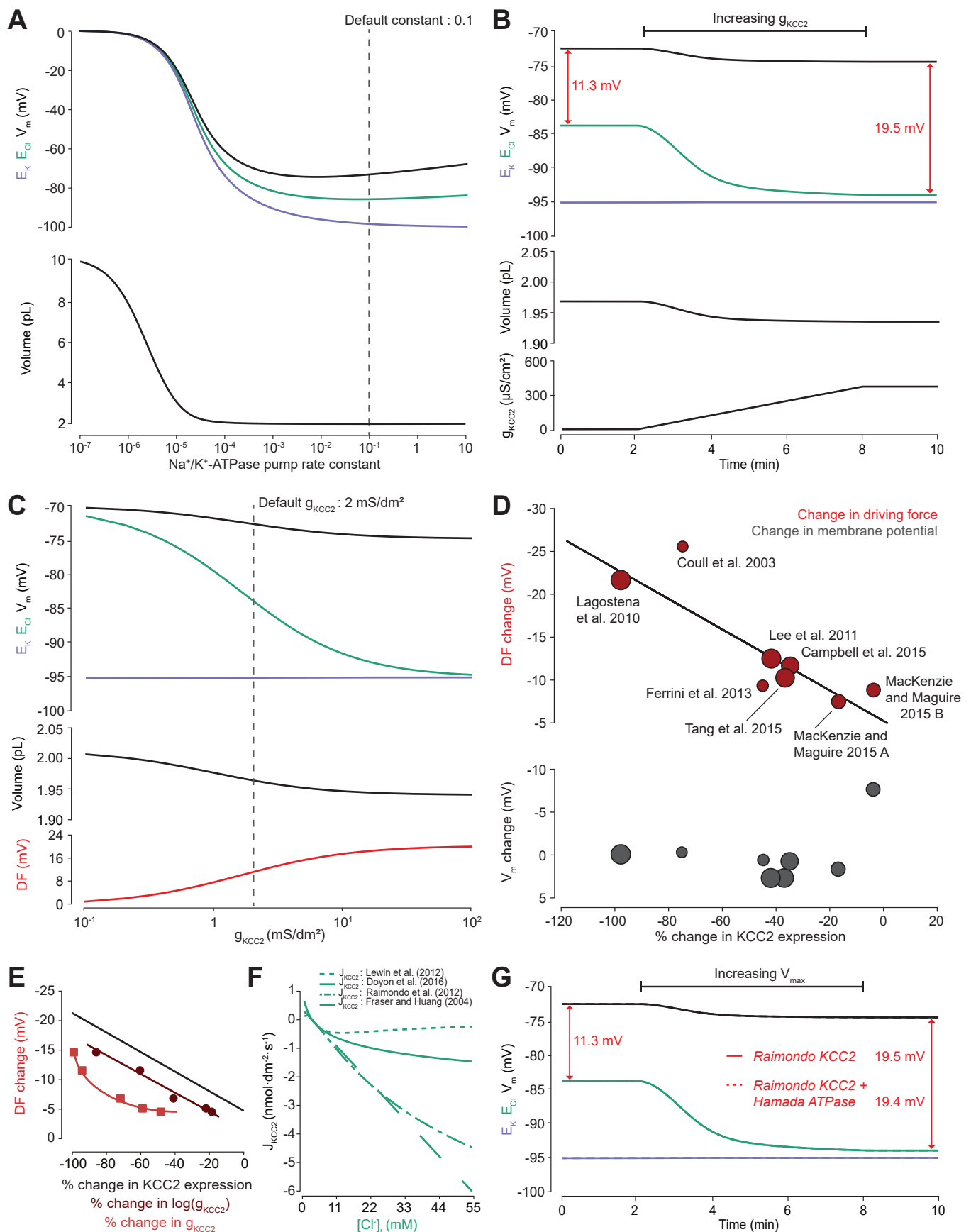
Using the analytic solution to my model I calculated how KCC2 activity affects steady state values of  $E_{Cl}$ ,  $E_K$ ,  $V_m$ ,  $w$  and  $\text{Cl}^-$  driving force (Fig. 3.3 C). In confirmation of my findings in Figure 3.2 D, with no KCC2 activity ( $g_{KCC2} = 0$ ),  $E_{Cl}$  equaled  $V_m$  and the  $\text{Cl}^-$  driving force was zero. As I increased  $g_{KCC2}$ , steady state  $E_{Cl}$  pulled away from  $V_m$  and approached  $E_K$ . This resulted in an increase in  $\text{Cl}^-$  driving force ( $V_m - E_{Cl}$ ) with steady state values of  $11.3 \text{ mV}$  at the chosen default value of  $g_{KCC2}$ . The results obtained with my

model are therefore fully consistent with the view that CCCs, in this case KCC2, establish the driving force for  $\text{Cl}^-$ .

I sought experimental data from the literature to determine whether changes in KCC2 activity correlate with alterations to steady-state  $[\text{Cl}^-]_i$ . I focused on changes in KCC2 expression level, as this is likely to be a strong predictor of changes in KCC2 activity. Indeed, in a meta-analysis of 7 studies and 8 experiments from my review of 26 studies, weighted for methodological biases and data quality, I observed a significant correlation ( $R^2 = 0.796, p < 0.001$ ) between the change in KCC2 expression and  $\text{Cl}^-$  driving force (Fig. 3.3 D and Table 3.1). Absolute changes in  $V_m$  were less than 2 mV in all but one study, meaning that the change in driving force could be ascribed to significant shifts in  $E_{\text{GABA}}$  ( $R^2 = 0.045, p < 0.001$ ). The outlier data point (showing a 8.45 mV change) was from a study of acute stress, where other factors could have transiently influenced  $V_m$  (MacKenzie and Maguire, 2015). The meta-analysis supports the prediction that cation-chloride cotransport by KCC2 is an important determinant of  $[\text{Cl}^-]_i$  ( $R^2 = 0.83, p < 0.001$ , 8 studies and 9 experiments) and driving force (Table 3.1).

---

**Figure 3.3 (facing page):** Cation-chloride cotransport sets the chloride reversal and driving force (DF) for transmembrane chloride flux. **(A)** Sufficient  $\text{Na}^+/\text{K}^+$ -ATPase activity is critical for steady state  $E_{\text{Cl}}$  (green),  $E_K$  (purple),  $V_m$  (black) and volume  $w$  (bottom panel), but these variables are relatively stable near the default pump rate (dashed line). **(B)** Increasing KCC2 activity in my model by increasing  $g_{\text{KCC2}}$  from  $20 \mu\text{S}/\text{cm}^2$  to  $370 \mu\text{S}/\text{cm}^2$  (bottom panel) resulted in a persistent decrease in  $E_{\text{Cl}}$ , a minimal decrease in  $E_K$ ,  $V_m$  and volume  $w$  (middle panel). This resulted in a permanent increase in the driving force for  $\text{Cl}^-$  via a change in  $E_{\text{Cl}}$  from -83.9 mV to -93.2 mV (red). **(C)** The steady state values for  $E_{\text{Cl}}$ ,  $E_K$ ,  $V_m$  (top panel), volume (middle panel) and  $\text{Cl}^-$  driving force (DF, bottom panel, red) at different KCC2 conductances. Increasing KCC2 activity resulted in a decrease in steady state  $E_{\text{Cl}}$  and DF.  $E_K$  represented a lower bound on  $E_{\text{Cl}}$  at high KCC2 conductances. **(D)** Meta-analysis of experimental studies demonstrates a correlation between KCC2 activity (% change) and  $\text{Cl}^-$ - DF (mV, top plot, red) but not membrane potential (mV, bottom plot, grey), confirming the role of KCC2 for establishing the neuronal  $\text{Cl}^-$  gradient in adult tissue. The data and scoring system used to generate the regression can be found in Tables 3.1 and 2.3. **(E)** Changing KCC2 “expression” in the analytical model (squares, pink), that is  $g_{\text{KCC2}}$ , does not cause a comparable shift in DF to that in the meta-analysis in **D** (black trend line), since the model produces a non-linear curve with smaller magnitude changes. However, when  $g_{\text{KCC2}}$  in my model is transformed using a log scale, a comparable shift is produced (circles, brown). **(F)** The pump rate velocity for different models of KCC2 were compared for differing intracellular chloride concentration. The equation employed in my model was based on Doyon et al. (2016) (solid line). The model of Lewin et al. (2012) (dotted line) was based on the renal distal tubule and had a diminished absolute velocity compared to my model. The models of Raimondo et al. (2012) and Fraser and Huang (2004) (dashed and dash-dotted lines respectively) had similar velocities across the range of concentrations and are both based on some experimental evidence.  $J_{\text{scale}}$  for each model was set such that the same steady state concentrations were achieved using any model with the other parameters kept constant (concurrent point). **(G)** Increasing KCC2 activity using the Raimondo et al. (2012) model by increasing  $V_{\text{max}}/J_{\text{scale}}$  resulted in a persistent decrease in  $E_{\text{Cl}}$  (green) and a minimal decrease in  $E_K$  (purple) and  $V_m$  (black), regardless of whether the cubic (solid lines) or Hamada et al. (2003) (dashed lines) ATPase model was employed. This resulted in a permanent increase in the driving force for  $\text{Cl}^-$  (red). The change in KCC2 strength was matched so that the final shift is similar to the usual shift in driving force gained using the standard KCC2 pump formulation in **B**. When the ATPase model of Hamada et al. (2003) was used in the experimental set up rather than the cubic ATPase model, the resulting driving force differed by only 0.1 mV from the usual value.



I compared the trend from my meta-analysis with the values expected from my KCC2 model's analytical solution (Fig. 3.3 E). Interestingly, my model behaved poorly when  $g_{KCC2}$  was used as a correlate for KCC2 expression, with shifts significantly lower and non-linear in trend. When the change in  $g_{KCC2}$  was instead considered on a logarithmic scale, the trend was closer to that generated by the experimental data. This result begs further consideration of KCC2  $\text{Cl}^-$  cotransport dynamics.

Alternate, parameterised models for KCC2 (Fraser and Huang, 2004; Raimondo et al., 2012; Lewin et al., 2012) had different kinetic rates for  $\text{Cl}^-$  transport (Fig. 3.3 F). Similar results for the time-dependent shift in driving force mediated by increasing KCC2 strength could be generated with these models, for example, when the model by Raimondo et al. (2012) with or without the alternative ATPase model by Hamada et al. (2003) was employed (Fig. 3.3 G).

### **3.3 Impermeant anions can only drive shifts in chloride driving force when average impermeant anion charge or osmolarity is altered, and even then the shifts are negligible**

#### **3.3.1 Altering the concentration of intracellular or extracellular impermeant anions, without changing the average charge of impermeant anions, does not affect the steady state gradient or driving force for chloride**

To determine the effect of impermeant anions on  $\text{Cl}^-$  homeostasis I first explored whether adjusting the concentration of impermeant anions ( $[X]_i$ ), while maintaining a constant average impermeant anion charge ( $z$ ), had any impact on  $E_{\text{Cl}}$ ,  $E_K$ ,  $V_m$  or volume. I initiated the full single-compartment model with different starting concentrations of impermeant anions (but the same average charge,  $z = -0.85$ ), and observed that regardless of the initial concentration of impermeant anions, over a period of minutes, the cell adjusted its volume to give an identical steady-state impermeant anion concentration (Fig. 3.4 A,  $[X]_i = 155 \text{ mM}$ ). Analytically, it can be shown that the number of moles of X determines completely the volume of the compartment, while the permeant ions alone cannot be used to predict steady state volume (Kay, 2017). Similarly, all initial impermeant anion concentrations resulted in identical steady state values of  $E_{\text{Cl}} (-83.8 \text{ mV})$ ,  $E_K (-95.1 \text{ mV})$  and  $V_m (-72.6 \text{ mV})$  (Fig. 3.4 B). This shows that simply adjusting the amount of impermeant anions within a cell has no persistent effect on  $[\text{Cl}^-]_i$ .

I then tested the effect of dynamically adding impermeant anions with the default average charge either intracellularly (Fig. 3.4 C) or extracellularly (Fig. 3.4 D). While impermeant anions are being added to the cell, the membrane potential hyperpolarises and  $E_{\text{Cl}}$  decreases, with  $[\text{Cl}^-]_i$  decreasing by 0.9 mM. However, following the cessation of impermeant anion influx,  $E_{\text{Cl}}$ ,  $E_K$ ,  $V_m$  and  $[X]_i$  return to steady state values due to compensatory changes to cell volume (Fig. 3.4 C). There are transient transmembrane fluxes of all ions

<b>Study</b>	<b>Region</b>	$\Delta\text{KCC2}$	$\Delta\text{NKCC1}$	<b>Weight</b>	$\Delta[\text{Cl}^-]_i$	$\Delta V_m$ (mV)	$\Delta DF$ (mV)
Lagostena et al. (2010)	hippocampus	↓ 98%	↓ 16%	36	↑ 118%	-0.9	-20.9
Lee et al. (2011)	hippocampus	↓ 42%	↑ 7%	35	↑ 72%	+2	-12
Campbell et al. (2015)	neocortex	↓ 37%	↑ 27%	34	↑ 59%	+2	-9.9
Tang et al. (2015)	spinal cord	↓ 35%	↓ 11%	31	↑ 56%	+0.2	-11.2
MacKenzie and Maguire (2015) A	hippocampus	↓ 17%	no data	24	↑ 37%	+1	-7.07
MacKenzie and Maguire (2015) B	hippocampus	↓ 4%	no data	23	↑ 2%	-8	-8.45
Mahadevan et al. (2015)	hippocampus	↓ 20%	no data	20	↑ 20%	no data	no data
Ferrini et al. (2013)	spinal cord	↓ 45%	no data	19	↑ 42%	0	-9
Coull et al. (2003)	spinal cord	↓ 75%	no data	18	↑ 151%	-1	-24.6
<i>R</i> <sup>2</sup> value	for $\Delta\text{KCC2}$				0.83	0.045	0.796
<i>p</i> -value					< 0.001	< 0.005	< 0.001

**Table 3.1:** Data from studies included in the meta-analysis and compared using statistical regression, which show that changes in the activity of KCC2 are associated with changes in Cl<sup>-</sup> driving force and intracellular Cl<sup>-</sup> concentration, but static V<sub>m</sub>. For each study, the shifts in the chloride gradient, membrane potential and driving force, and changes in KCC2 expression and NKCC1 expression were extracted, and these shifts were regressed against the percentage change in KCC2 expression. NKCC1 was assumed to be unlikely to alter chloride homeostasis as adult tissue only was considered (Ben-Ari, 2002), although studies reporting non-significant changes in NKCC1 expression were weighted higher than those that did not test NKCC1 expression (the scoring methodology is detailed in Table 2.3 in the Methods). However, when studies also reported significant expression changes in NKCC1 (or functional inhibition indicating that NKCC1 was contributing towards the disease-mediated shift in chloride concentration), they were excluded.

while anions are added into the cell, and in particular the inward flux of the cations  $\text{Na}^+$  and  $\text{K}^+$ , such that the sum  $[\text{X}]_i + [\text{Cl}^-]_i$  is not necessarily kept constant during impermeant anion addition. Impermeant ions (with default average charge) were added to the extracellular space, which is effectively an infinite bath in the model, while proportional decreases in  $[\text{Cl}^-]_o$  were applied to correct for the changes to charge and osmotic balance. Additions in the extracellular space, similarly, resulted in a temporary depolarisation of  $E_{\text{Cl}}$  and  $V_m$ , but no persistent shift in these parameters (Fig. 3.4 D). The addition of extracellular impermeant anions did however result in a small compensatory decrease in cell volume secondary to the large shifts in  $[\text{Cl}^-]_i$  required to maintain the proportion of  $[\text{Cl}^-]_i$  to  $[\text{Cl}^-]_o$  according to the Nernst potential.

In summary, there is no lasting effect on the reversal potential or driving force for  $\text{Cl}^-$  if only the concentration of a neuron's intracellular or extracellular impermeant anions is altered.

### **3.3.2 Changing the average charge of impermeant anions can drive substantial shifts in the reversal potential for chloride, but has negligible effects on chloride driving force**

I next sought to determine how changes in the average charge of the impermeant ions ( $z$ ) might influence the driving force on  $\text{Cl}^-$ . Such changes in average  $z$  could be associated with various cellular processes, including post-translational modifications of proteins that decrease their charge without changing the absolute number of protein molecules, or pH changes where for example a carboxyl group is protonated. To investigate this parameter, I modified the average  $z$  of intracellular impermeant anions from -0.85 to -1 and measured accompanying changes in  $E_{\text{Cl}}$ ,  $E_K$ ,  $V_m$  and cell volume (Fig. 3.5 A). I found that the shift to a more negative average  $z$  resulted in both a transient and persistent decrease in  $E_{\text{Cl}}$ ,  $E_K$  and  $V_m$ .  $[\text{Cl}^-]_i$  decreased transiently by 1.1 mM. Importantly, the shifts in  $E_{\text{Cl}}$  were accompanied by broadly matching shifts in  $E_K$  and  $V_m$ , which resulted in a small change in the driving force for  $\text{Cl}^-$  of < 0.2 mV. Both numerical and analytic calculation of steady state values for  $E_{\text{Cl}}$ ,  $E_K$  and  $V_m$  in my model showed that changing the average charge of impermeant anions, while substantially affecting  $E_{\text{Cl}}$ , had very small effects on the driving force for  $\text{Cl}^-$  (Fig. 3.5 B). By shifting  $z$  within reasonable ranges for mammalian neurons (Lodish et al., 2009; Raimondo et al., 2015) and assuming osmo- and electro-neutrality, only shifts of < 1 mV could be generated. In addition, although the absolute number of impermeant anions (moles) remained constant throughout the process of modifying  $z$ , cell volume shifted, and as a consequence modest alterations to the concentration of impermeant anions occurred as well.

Next, instead of adjusting the charge of existing anions in intracellular impermeant anions as described above, I directly added impermeant anions of differing valence to the cell (Fig. 3.5 C and D). This had the effect of both increasing the absolute quantity of impermeant anions and adjusting the average charge of impermeant anions. The 'addition' of impermeant anions in this way models the de novo synthesis of impermeant anion species,

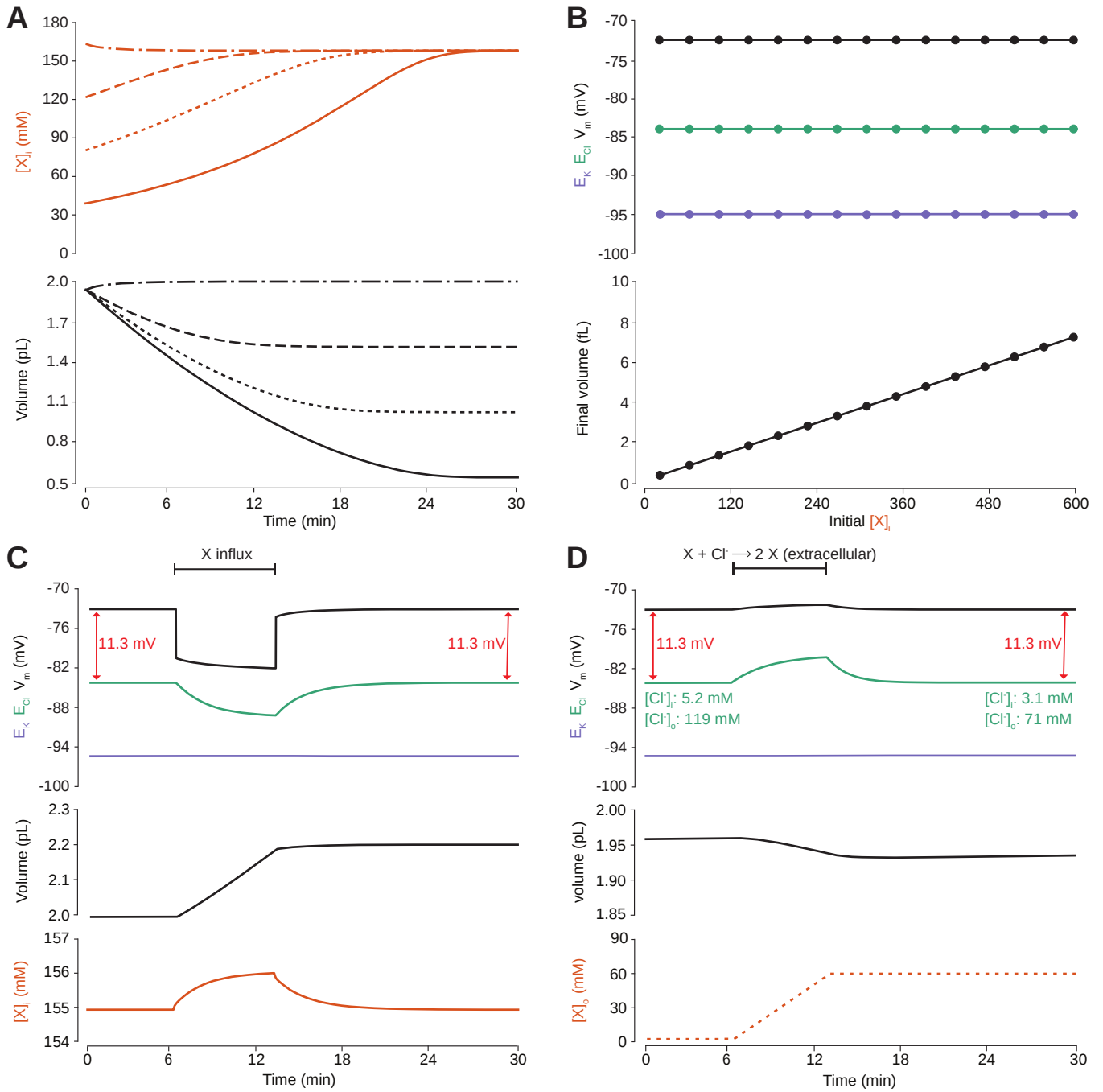


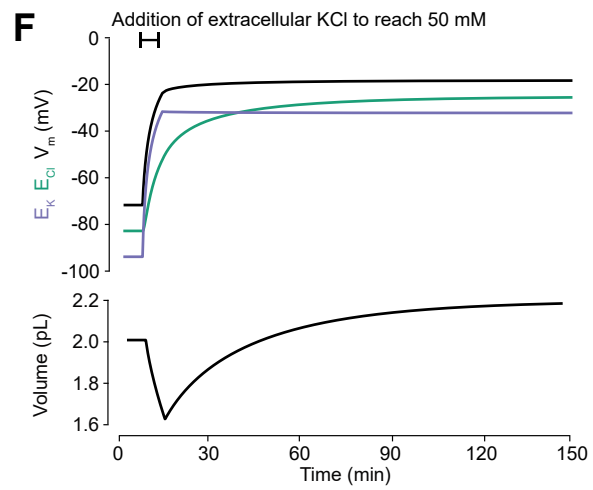
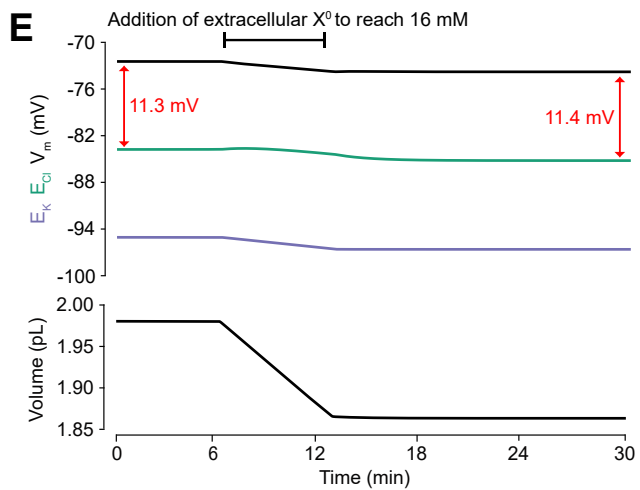
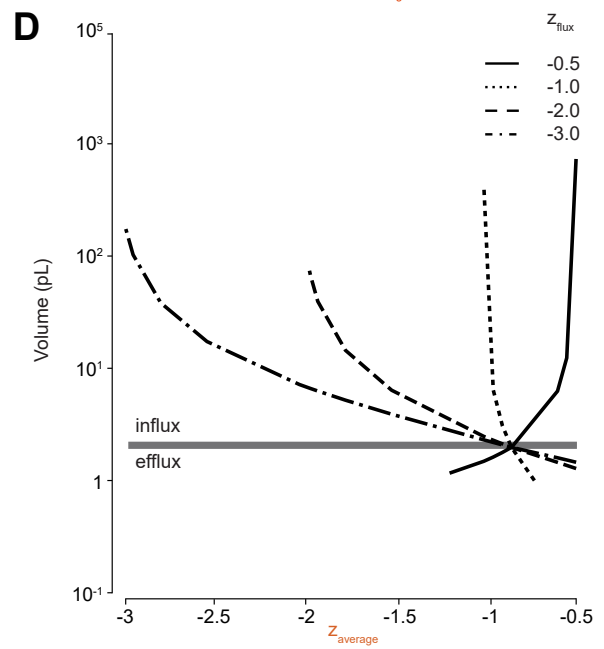
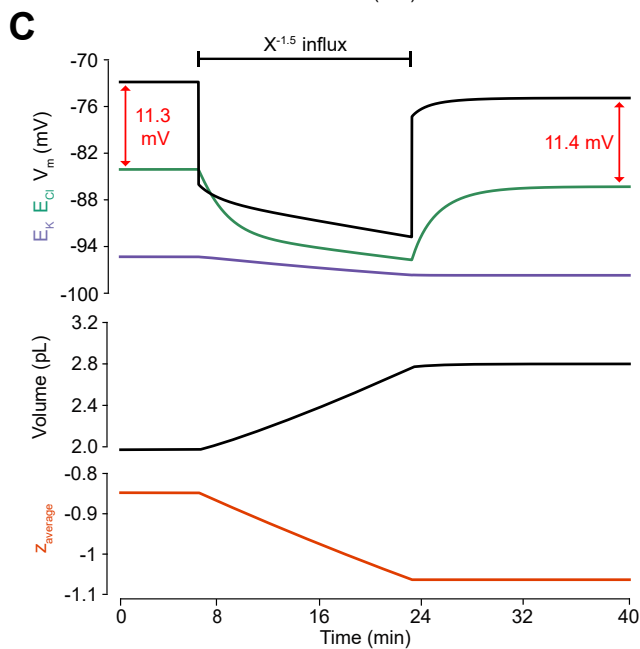
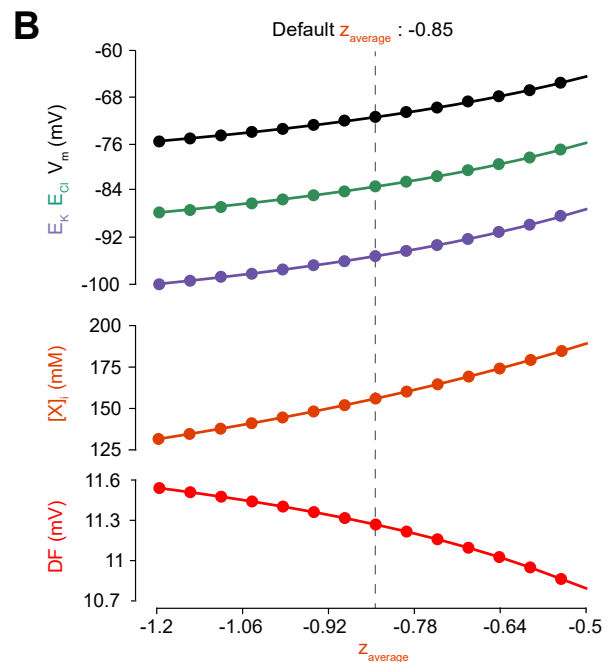
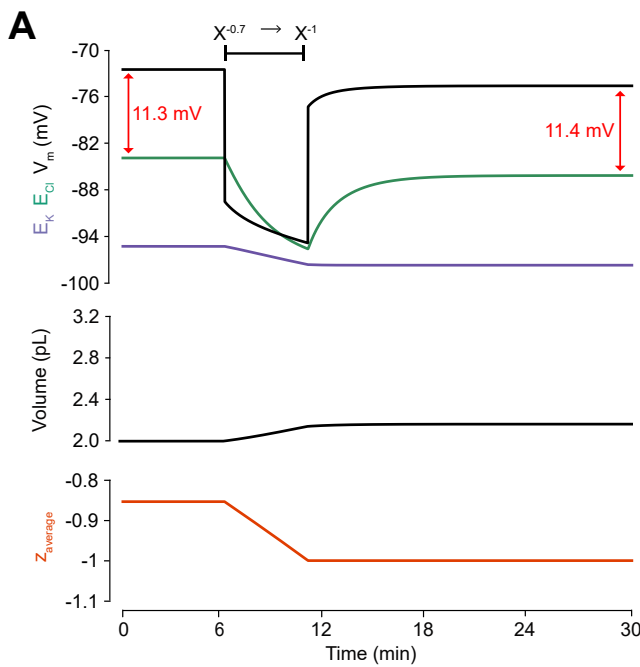
**Figure 3.4:** Adding intracellular or extracellular impermeant anions, without changing the average charge of impermeant anions, does not affect the steady state gradient or driving force for chloride. (A) Initiating the model with different starting concentrations of intracellular impermeant anions ( $[X]_i$ ) with the same average charge  $z$  (orange, top panel), led to compensatory volume changes (bottom panel) which resulted in identical steady state concentrations. (B) Steady state  $E_{Cl}$  (green),  $E_K$  (purple) and  $V_m$  (black) were identical regardless of initial  $[X]_i$ . Final volume however was a linear function of initial  $[X]_i$  (bottom panel). (C) Addition of impermeant anions of the same average charge ( $z$ ) caused transients shifts in  $E_{Cl}$  (green, top panel),  $E_K$  (purple),  $V_m$  (black) as well as  $[X]_i$  (orange, bottom panel) for the duration of the influx, and sustained increases in volume (black, middle panel). No persistent changes in  $E_{Cl}$ ,  $E_K$  or  $V_m$  were observed. (D) Similarly, the addition of extracellular impermeant anions in an osmoneutral manner and without affecting  $[X]_i$  causes transient shifts in the permeable ion gradients (top panel, colours as in C), and sustained changes in cellular volume (black, middle panel) as well as the extracellular X and extracellular and intracellular  $Cl^-$  concentrations.

or their active transport into the cell. This process also resulted in both transient and persistent changes to  $E_{Cl^-}$ ,  $E_K$  and  $V_m$ , which was dependent on the extent that average  $z$  was altered (in Fig. 3.5 C  $[Cl^-]_i$  decreased by 1.8 mM). Again, while the large additions of impermeant anions could substantially alter the  $Cl^-$  reversal potential, this had a negligible effect on the driving force for  $Cl^-$  because of matching shifts in  $V_m$ . Driving shifts in  $E_{Cl^-}$  in this manner also resulted in changes to cell volume (Fig. 3.5 D).

To explore the influences of altering average impermeant anion charge in the extracellular milieu around the biophysical cell model, I considered the scenario of introducing impermeant anions of a neutral charge to the extracellular environment, therefore increasing the average extracellular impermeant anion charge without compromising extracellular charge neutrality (Fig. 3.5 E). This would simulate the experimental manipulation of adding 16 mM mannitol, a membrane impermeant molecule, to the extracellular space. In this case, I observed shifts in  $E_{Cl^-}$  and a 0.3 mM decrease in  $[Cl^-]_i$ , but the changes to the driving force were still negligible ( $< 0.1$  mV). The volume of the cell decreased as ion and water flux balanced the osmolarity difference created by the increased osmoles in the extracellular milieu (from 297 to 313 mM). In contrast, introducing extracellular osmoles in the form of permeable ions, in this case 50 mM extracellular KCl, caused an initial decrease in cell volume from the high transmembrane osmotic difference generated during the osmoles' addition. This was followed by progressive cell swelling and depolarisation of ionic and membrane potentials while permeable ions equilibrated via intracellular flux (Fig. 3.5 F). The direction of KCC2 flux reversed from outwards to inwards immediately after the KCl had finished being added, and then the magnitude and direction of  $J_{KCC2}$  slowly stabilised to near its previous value over 120 minutes.

---

**Figure 3.5 (facing page):** Adjusting the average charge of impermeant anions shifts the chloride reversal potential with negligible effects on the driving force for chloride. **(A)** Decreasing the average charge of impermeant anions from -0.85 (the default value) to -1 (orange, bottom panel), without changing the absolute number of intracellular impermeant anions caused a persistent decrease in  $E_{Cl^-}$  (green, top panel),  $E_K$  (purple) and  $V_m$  with moderate increases in volume (middle panel) in my default single compartment model. Negligible changes in  $Cl^-$  driving force ( $\Delta DF = 0.16$  mV, red) were observed. **(B)** Analytic solution (solid lines) for different impermeant anion average charge ( $z$ ) exactly matches the steady state values from numerical, time series runs (dots) based on adjusting average  $z$  as in **A**. Steady state  $E_{Cl^-}$ ,  $E_K$ ,  $V_m$  (top panel) and  $[X]_i$  (middle) increased with increasing average  $z$ , while changes in average  $z$  resulted in very small changes in  $Cl^-$  DF (bottom, red). The vertical dashed line indicates the values at the chosen default average  $z$  of -0.85. **(C)** Influx of a species of impermeant anions with average charge -1.5 that decreased average  $z$  (bottom panel) from -0.85 to -1 and increased the number of impermeant anions also caused persistent decreases of  $E_{Cl^-}$ ,  $E_K$  and  $V_m$  as in **A**, but with larger increases in cell volume (middle panel). Again, very small persistent changes in  $Cl^-$  DF were observed. **(D)** Large volume shifts occur when average impermeant charge is changed via temporary anion species flux across the membrane. Repeating the methodology in **C** for ion species with different charges ( $z_{flux}$ ) demonstrates the effect of driving shifts in the average intracellular impermeant charge on cell volume. Generating even small shifts in average  $z$  by adding or removing impermeant anions can cause large changes in cell volume. **(E)** Addition of 16 mM impermeant extracellular X of zero charge that therefore increased the overall  $[X]_o$  charge caused a negligible decrease in  $E_{Cl^-}$ ,  $E_K$ ,  $V_m$ , DF (top panel) and cell volume (bottom panel). **(F)** Addition of 50 mM extracellular  $K^+$  and  $Cl^-$  caused the potentials to depolarise (top panel) with an initial decrease in cell volume followed by steady cellular expansion (bottom panel).



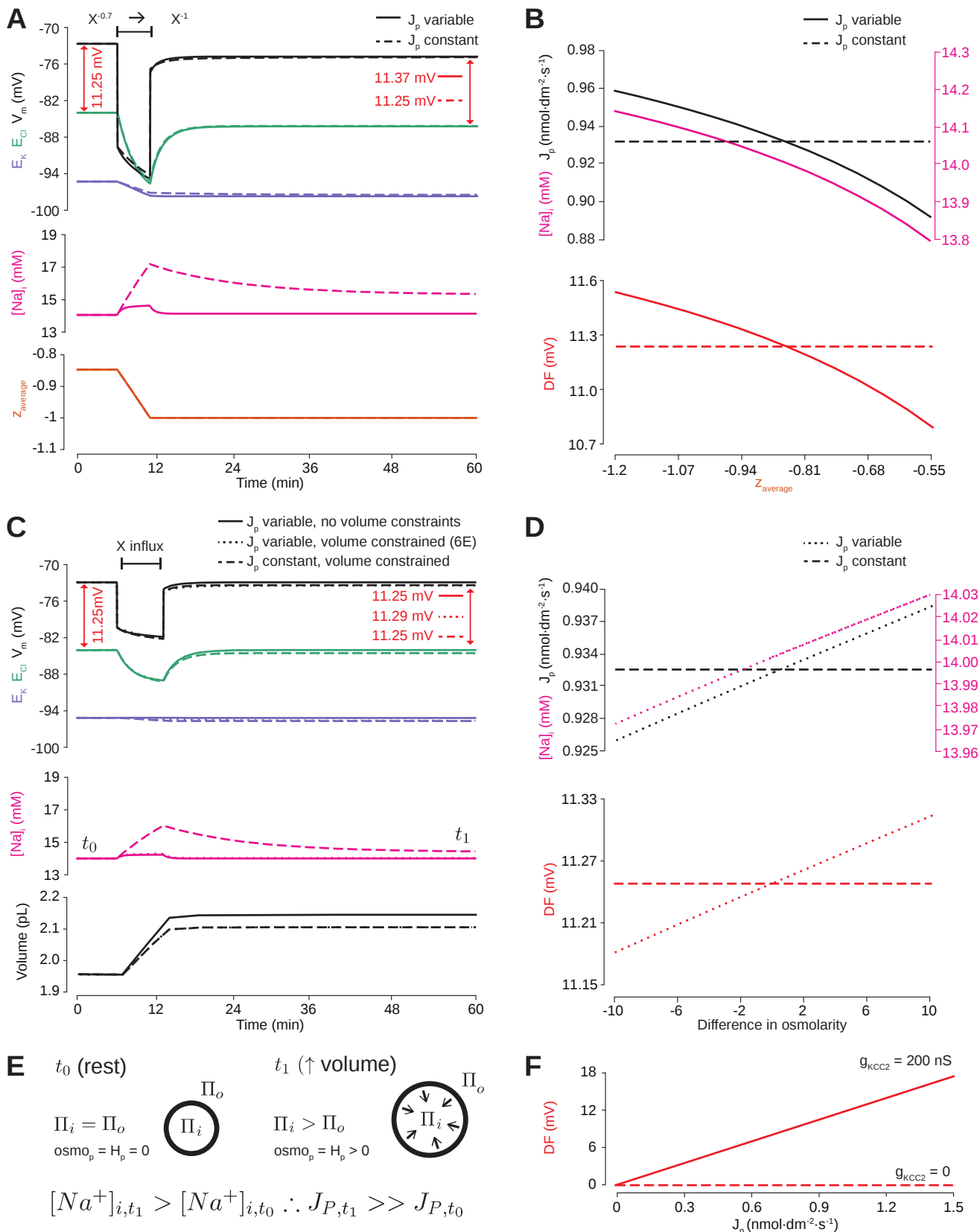
My single compartment model of  $\text{Cl}^-$  homeostasis demonstrates that the adjustment of average impermeant anion charge can significantly affect  $E_{\text{Cl}}$ , but this results in negligible changes to the driving force for  $\text{Cl}^-$ . This contrasts with the results shown earlier, where adjusting the activity of cation-chloride cotransport modulates both  $E_{\text{Cl}}$  and the driving force for  $\text{Cl}^-$  substantially.

### 3.3.3 Impermeant anions drive small shifts in chloride driving force by modifying the $\text{Na}^+/\text{K}^+$ -ATPase pump rate under conditions of active chloride cotransport

I next set out to determine how, and under what conditions, the modification of impermeant anions could potentially generate the very small persistent shifts in  $\text{Cl}^-$  driving force I observed in my models. First, I repeated the simulation performed in Figure 3.5 A by changing the average charge of impermeant anions in the cell, but under conditions where the  $\text{Na}^+/\text{K}^+$ -ATPase effective pump rate ( $J_p$ ) was either a cubic function of the transmembrane  $\text{Na}^+$  gradient (default condition), or was fixed at a constant value (Fig. 3.6 A). In the case where the pump rate was fixed, adjusting the average charge of impermeant anions generated no persistent change in  $\text{Cl}^-$  driving force (Fig. 3.6 A). Modifying impermeant anions caused a significant change in steady-state intracellular  $\text{Na}^+$  concentration when  $J_p$  was kept constant. However, small shifts in  $\text{Cl}^-$  driving force occurred only when the effective pump rate was variable, in which minor changes to  $[\text{Na}^+]_i$  caused significant changes to  $J_p$ , which in turn resulted in a small shift in  $\text{Cl}^-$  driving force.

---

**Figure 3.6 (facing page):** Impermeant anions drive small shifts in chloride driving force by modifying the  $\text{Na}^+/\text{K}^+$ -ATPase pump rate under conditions of active chloride cotransport. (A)  $E_{\text{Cl}}$  (green),  $E_K$  (purple) and  $V_m$  (black) (top panel),  $[\text{Na}^+]_i$  (pink, middle panel) and average impermeant anion charge  $z$  (orange, lower panel) over time in the default single compartment model. Changing the average  $z$  from -0.85 to -1 generated small, persistent  $\text{Cl}^-$  DF shifts (arrows, red) only when the effective ATPase pump rate ( $J_p$ ) was variable (solid line) and not when  $J_p$  was kept constant (dashed line). (B) Solving analytically across different values of  $z$  with either a variable  $J_p$  (solid lines) or a constant  $J_p$  (dashed line), demonstrates the direct relationship between  $\text{Na}^+$  (pink), effective pump rate ( $J_p$ ) (top panel) and  $\text{Cl}^-$  DF (lower panel, red). (C)  $E_{\text{Cl}}$  (green),  $E_K$  (purple) and  $V_m$  (black),  $[\text{Na}^+]_i$  (pink, middle panel) and cell volume (black, lower panel) over time in the default single compartment model. Impermeant anions of the same average charge of the cell were added. A volume constraint was incorporated by adding a hydrostatic force dependent on membrane tension (dashed lines), which resulted in an impermeable anion induced transmembrane osmotic differential. This caused a small change in  $\text{Cl}^-$  DF when  $J_p$  was variable (dashed line), but not when  $J_p$  was held constant (dotted lines). (D) Solving analytically across osmolarity differences demonstrates the direct relationship between  $\text{Na}^+$  (pink), effective pump rate ( $J_p$ ) (top panel) and  $\text{Cl}^-$  driving force (lower panel). Note the small changes in  $\text{Cl}^-$  DF. (E) Schematic explaining the mechanism through which impermeant anion induced cell swelling in the presence of volume constraints (i.e. membrane tension) result in steady states with equal but non-zero osmotic ( $osmop$ ) and hydrostatic pressures ( $H_P$ ), causing transmembrane osmotic differences ( $t_1$ ). This causes small changes in  $\text{Na}^+$ , and hence  $J_p$ . (F) All  $\text{Na}^+/\text{K}^+$ -ATPase pump rate-related shifts in the  $\text{Cl}^-$  DF require KCC2 activity; in the absence of activity (dashes), no shifts in driving force can occur.



There is a direct relationship between the average charge of impermeant anions ( $z$ ),  $[Na^+]_i$ , the effective  $Na^+/K^+$ -ATPase pump rate and  $Cl^-$  driving force. This relationship was abolished when the effective  $Na^+/K^+$ -ATPase pump rate was held constant by removing its dependence on  $Na^+$  (Fig. 3.6 B). In addition, even large variations in effective pump rate near the default value caused negligible shifts in  $Cl^-$  driving force of  $< 1$  mV. These results were consistent when using the experimentally-matched ATPase model by Hamada et al. (2003), with slight differences in final values of  $< 0.1$  mV (Fig. 3.7 A).

I then tested whether relaxing the condition of transmembrane osmoneutrality might also alter impermeant anion induced effects on  $Cl^-$  driving force. I modelled a situation in which increases in cell surface area beyond a certain ‘default’ or ‘resting’ surface area generated a hydrostatic pressure (membrane tension), which could balance an osmotic pressure difference of 10 mM between the intra- and extracellular compartments (see Fig. 3.6 C, schematic in Fig. 3.6 E and Equation 2.9 in the Methods). In this case, adding impermeant anions of default charge  $z$  resulted in constrained increases in cell volume, which were accompanied by persistent transmembrane differences in osmolarity and intracellular  $Na^+$  concentration. This was sufficient to generate small differences in driving force for  $Cl^-$  of  $< 0.1$  mV for reasonable increases in cell surface area (Nichol and Hutter, 1996; Dai et al., 1998). Again, this was entirely due to  $Na^+$  driven shifts in the  $Na^+/K^+$ -ATPase effective pump rate. By removing the dependence of  $Na^+/K^+$ -ATPase activity on  $Na^+$  concentration, addition of impermeant anions no longer generated persistent shifts in  $Cl^-$  driving force (Fig. 3.6 C).

Because the model is also directly dependent on  $[Na^+]_i$ , relaxing the condition of transmembrane osmoneutrality produced consistent results when employing the experimentally-matched ATPase model by Hamada et al. (2003), with minor differences of  $< 0.1$  mV in final driving force shifts noted (Fig. 3.7 C). I observed a direct relationship between transmembrane osmotic gradient,  $[Na^+]_i$ , the effective  $Na^+/K^+$ -ATPase pump rate and  $Cl^-$  driving force. This relationship was removed when the effective  $Na^+/K^+$ -ATPase pump rate was held constant, with no changes in  $Cl^-$  driving force seen despite the generation of the same shift in osmoneutrality (Fig. 3.6 D).

In summary, changes in  $Cl^-$  driving force generated by changing the ionic contributions to cellular charge (by altering the average charge of impermeant anions) or osmoneutrality (by increasing the contribution of hydrostatic pressure) are due to the alteration of the dynamics of active ion transport mechanisms in the cell. However, these effects are negligible in magnitude and cannot contribute significantly to setting physiologically observed  $Cl^-$  driving forces. It is worth reiterating that any non-zero  $Cl^-$  driving force is entirely dependent on the presence of active  $Cl^-$  cotransport. In my model, without any KCC2 activity, neither the  $Na^+/K^+$ -ATPase nor impermeable anions can shift  $Cl^-$  out of equilibrium (Fig. 3.6 F). In the absence of KCC2, there is no  $Cl^-$  driving force as  $E_{Cl} = V_m$ .

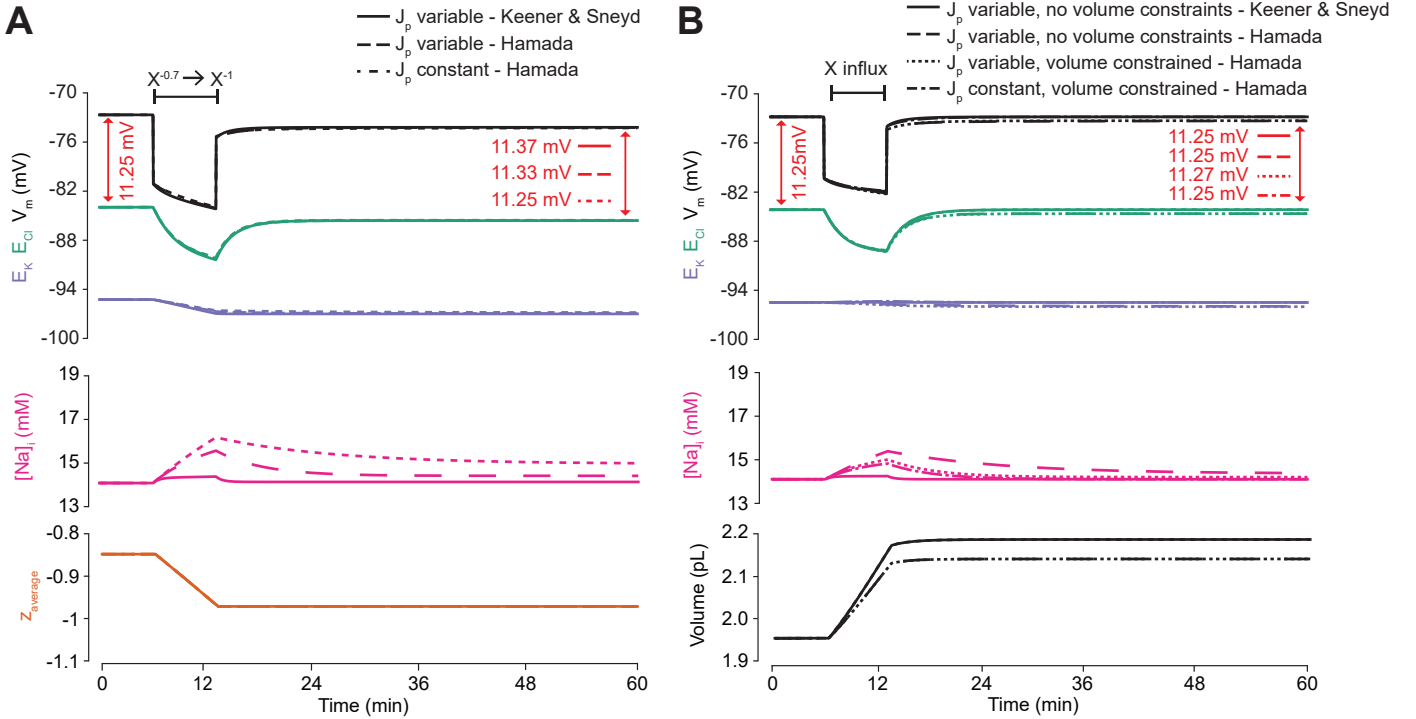


**Figure 3.7:** Alternative ATPase and KCC2 models with different kinetics have similar properties to my model’s ATPase when impermeant anions in the cell are changed, and are also dependent on the pump rate. **(A)** The experiment for Figure 3.6 A was repeated using the usual ATPase model (solid line) compared to the model of Hamada et al. (2003) and is consistent with the results using the standard cubic ATPase model.  $E_{Cl}$  (green),  $E_K$  (purple) and  $V_m$  (black) (top panel),  $[Na^+}_i$  (pink, middle panel) and average impermeant anion charge  $z$  (orange, lower panel) over time are shown in the default single compartment model. Changing the average  $z$  from -0.85 to -1 generated small, persistent  $Cl^-$  driving force shifts (arrows) only when the effective ATPase pump rate ( $J_p$ ) was variable (solid and dashed line) for both pump models, and not when  $J_p$  was kept constant (dotted line). **(B)** The experiment for Figure 3.6 C was repeated comparing the usual ATPase model (solid line) to the model of Hamada et al. (2003) and is consistent with the results using the standard cubic ATPase model.  $E_{Cl}$  (green),  $E_K$  (purple) and  $V_m$  (black) (top panel),  $[Na^+}_i$  (pink, middle panel) and cell volume (black, lower panel) over time are shown in the single compartment model. Impermeant anions of the same average charge of the cell were added. A volume constraint on the model of Hamada et al. (2003) was incorporated by adding a hydrostatic force dependent on membrane tension (dotted lines), which resulted in an impermeable anion induced transmembrane osmotic differential. This caused a small change in  $Cl^-$  driving force when  $J_p$  was variable (dotted line), but not when  $J_p$  was held constant (dash-dotted lines).

### **3.4 A multi-compartment model shows that local differences in chloride driving force can be achieved with cation-chloride cotransport by restricting chloride diffusion, but not with impermeant anions, which cause local swelling**

An important functional question is how  $\text{Cl}^-$  driving force might be modified at a local level within a neuron. I considered local persistent changes of  $\text{Cl}^-$  driving force for the case of active transmembrane  $\text{Cl}^-$  fluxes (Fig. 3.8) and impermeant anions (Fig. 3.9) by extending the single compartment model described above into a multi-compartment model or ‘virtual dendrite.’ This dendrite was 100  $\mu\text{m}$  in length and consisted of ten compartments, each of 10  $\mu\text{m}$  height and 1  $\mu\text{m}$  diameter. The compartments contained the same mechanisms and default parameterisation as the single compartment model described above. Compartmental volume was changed by altering the radius, while holding the height constant. In addition, all ions, except impermeant anions, could move between compartments by electrodiffusion (Fig. 3.8 A and Methods, Section 2.2.1).

#### **3.4.1 Changes in cation-chloride cotransport activity generate local differences in chloride reversal and driving force, which depend on cytoplasmic diffusion rates**

To explore the local effects of CCC activity, I increased  $g_{\text{KCC}2}$  from the default value of 20  $\mu\text{S}/\text{cm}^2$  to 60  $\mu\text{S}/\text{cm}^2$  in the second from top compartment of the virtual dendrite exclusively. This resulted in a persistent decrease in  $E_{\text{Cl}}$ , concurrent with a modest decrease in  $V_m$ , resulting in a permanent increase in  $\text{Cl}^-$  driving force and minimal change in compartment volume (Fig. 3.8 B). The spatial precision of this alteration depended strongly on the diffusion constant for  $\text{Cl}^-$ . With a  $\text{Cl}^-$  diffusion constant of  $2.03 \times 10^{-7} \text{ dm}^2/\text{s}$ , these alterations spread widely through the virtual dendrite. For example, the change in  $\text{Cl}^-$  driving force was 4.8 mV in the furthermost compartment (90  $\mu\text{m}$  apart) as compared to 5.9 mV in the compartment manipulated. When I decreased the  $\text{Cl}^-$  diffusion constant by one order of magnitude, the change in  $\text{Cl}^-$  driving force was 7.3 mV in the compartment in which KCC2 was adjusted, but only 1.8 mV in the furthermost compartment from the site of manipulation (Fig. 3.8 C). These findings suggest that local differences in cation-chloride cotransport activity can drive spatially restricted differences in  $\text{Cl}^-$  driving force under conditions of constrained  $\text{Cl}^-$  diffusion, however under conditions of typical ionic diffusion the effect of  $\text{Cl}^-$  transport by KCC2 is relatively widespread.

#### **3.4.2 Local impermeant anions do not appreciably affect the local driving force for chloride**

Following the last result, I considered whether changing impermeant anions in part of a dendrite could create a local area with a different  $\text{Cl}^-$  driving force compared to the rest of the cell. I first added impermeant anions of average charge ( $z$ ) exclusively to the second

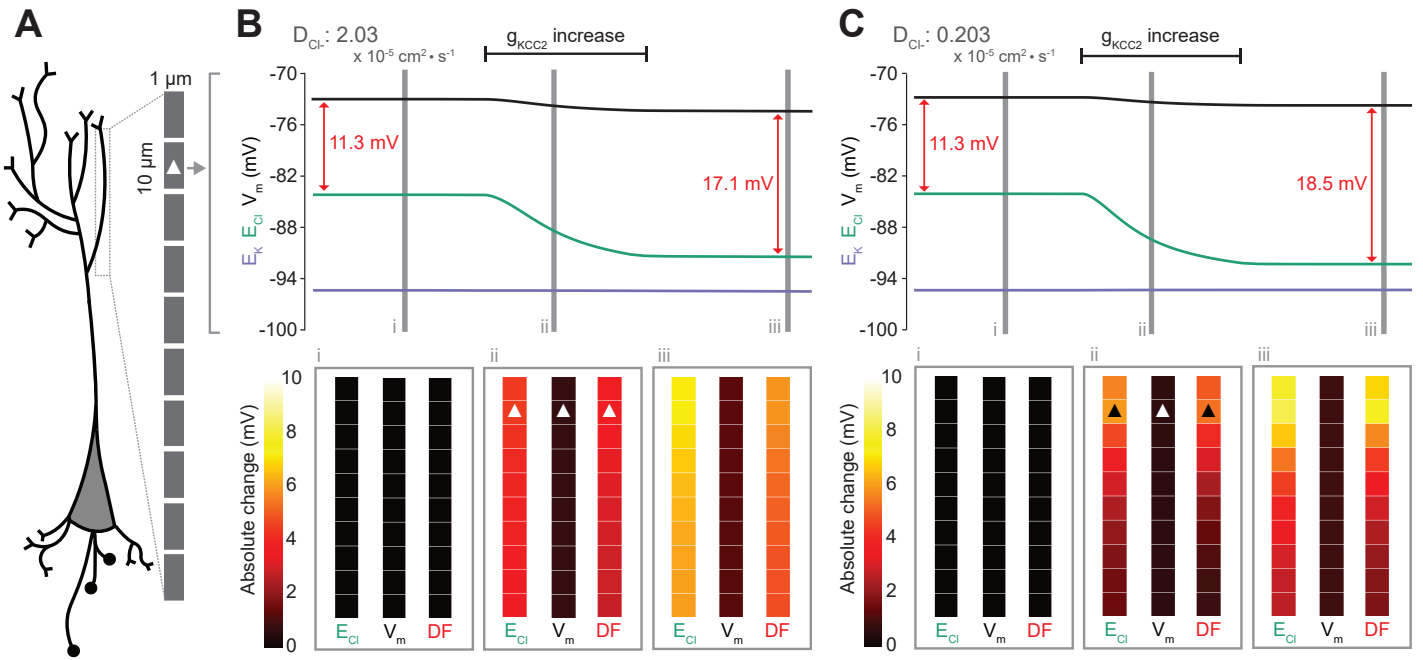


**Figure 3.8:** Local changes in KCC2 activity generate local differences in chloride reversal and driving force only under conditions of constrained chloride diffusion. **(A)** Schematic depicting the multi-compartment model representing a virtual dendrite of length 100  $\mu\text{m}$  and radius 0.5  $\mu\text{m}$ . The virtual dendrite consists of 10 compartments of initial height 10  $\mu\text{m}$ . Each compartment contains the same mechanisms and default parameterisation as the single compartment model. All ions, except impermeant anions, could move between compartments by electrodiffusion. **(B)** Top panel,  $E_{\text{Cl}}$  (green),  $E_K$  (purple),  $V_m$  (black) and calculated DF (arrows, red) from the second from top compartment (indicated with a white triangle) where the conductance of KCC2 was increased. The insets depict the diameter, and absolute change from baseline of  $E_{\text{Cl}}$ ,  $V_m$  and DF for all compartments before (i), during (ii) and after (iii) the activity of KCC2 was selectively increased. This resulted in  $E_{\text{Cl}}$  decreasing in all compartments with minimal changes to  $E_K$  and  $V$ . Consequently, the  $\text{Cl}^-$  DF (red) increased. In this case the diffusion constant for  $\text{Cl}^-$  ( $D_{\text{Cl}^-} = 2.03 \times 10^{-7} \text{ dm}^2/\text{s}$ ) resulted in  $E_{\text{Cl}}$  and DF changes being widespread across the virtual dendrite. **(C)** Reducing the  $\text{Cl}^-$  diffusion constant to  $0.2 \times 10^{-7} \text{ dm}^2$  resulted in a localised effect of compartment specific KCC2 activity increases on  $E_{\text{Cl}}$  and DF.

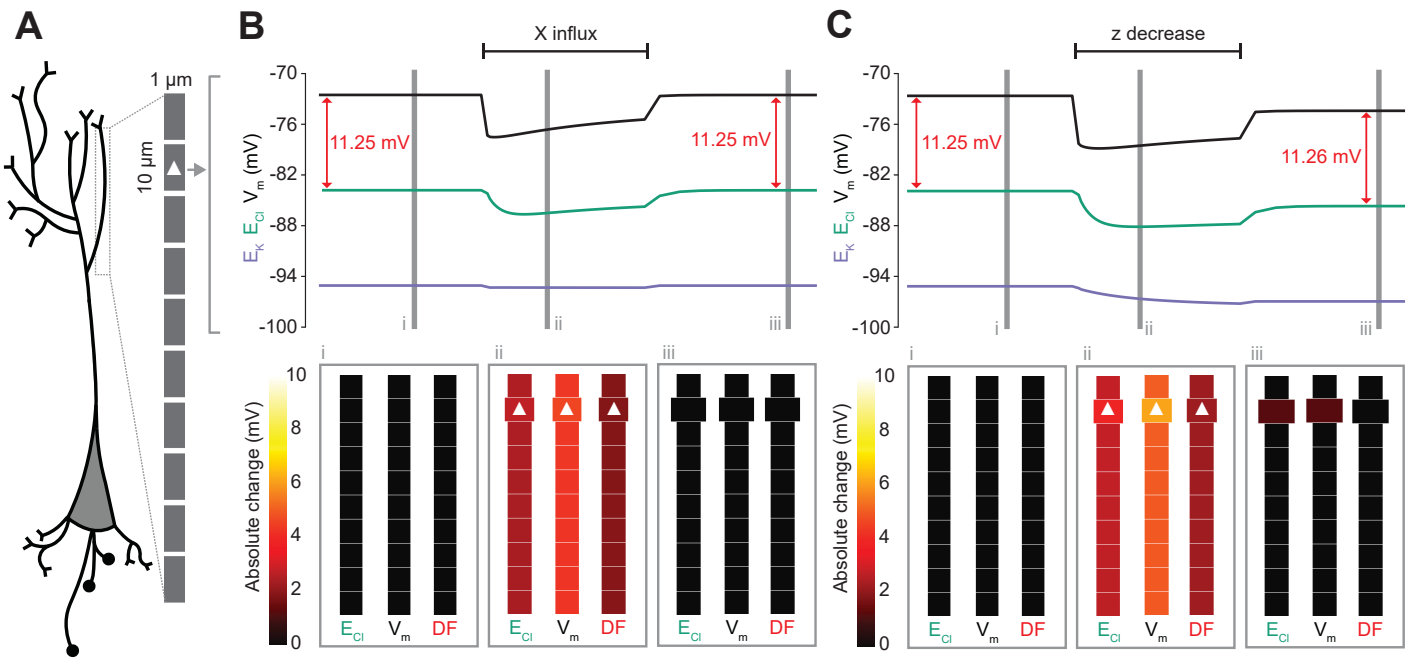


**Figure 3.9:** Local changes in impermeant anions do not establish the local driving force for chloride. **(A)** Multi-compartment model of a 10 compartment 100  $\mu\text{m}$  virtual dendrite as in Figure 3.8. **(B)** Top panel,  $E_{\text{Cl}}$  (green),  $E_K$  (purple),  $V_m$  (black) and calculated DF (arrows, red) within the compartment where additional impermeant anions were exclusively added (indicated with a white triangle). The insets depict the diameter, and absolute change from baseline for  $E_{\text{Cl}}$ ,  $V_m$  and DF for each compartment of the virtual dendrite before (i), during (ii) and after (iii) impermeant anions were added. The selective addition of impermeant anions of average  $z$  selectively to the second from top compartment only resulted in transient but non-permanent shifts in  $E_{\text{Cl}}$ ,  $V_m$  and the  $\text{Cl}^-$  DF in all compartments. The volume of the compartment where impermeant anion addition occurred increased permanently. **(C)** Traces and insets as in **B** showing the addition of impermeant anions of different charge in order to decrease average  $z$  in the second from top compartment specifically. Note that during addition of impermeant anions,  $E_{\text{Cl}}$ ,  $E_K$ ,  $V_m$  changed. However the only persistent changes were a local decrease in  $E_{\text{Cl}}$  and  $V_m$  in the compartment manipulated, with a negligible change in DF (0.01 mV). Again, impermeant anion addition resulted in an increase in the volume of the specific dendritic compartment manipulated.

compartment of the virtual dendrite while measuring the  $\text{Cl}^-$  reversal,  $V_m$  and  $\text{Cl}^-$  driving force (DF) in all compartments. During addition of the impermeant anions,  $E_{\text{Cl}}$  and  $V_m$  decreased with an accompanying decrease in  $\text{Cl}^-$  driving force. However, following cessation of impermeant anion influx, all parameters returned to baseline levels, except for the volume of that specific compartment, which showed a modest increase (Fig. 3.9 B). This suggests that local addition of impermeant anions of the same average charge as the intracellular impermeant anions has no local effect on  $\text{Cl}^-$  homeostasis but can affect the volume of the compartment concerned.

Next, I again added impermeant anions to the second compartment of the virtual dendrite, but this time I added impermeant anions with a more negative charge than average ( $z = -1$ ). This resulted in the average charge of impermeant anions in that specific compartment becoming more negative (Fig. 3.9 C). During the addition of the impermeant anions,  $E_{\text{Cl}}$  and  $V_m$  decreased across the dendrite, but with small accompanying shifts in  $\text{Cl}^-$  driving force. Following cessation of local impermeant anion influx, a persistent shift in  $E_{\text{Cl}}$  and  $V_m$  was observed specifically in the compartment manipulated. However, this generated a negligible, persistent change in  $\text{Cl}^-$  driving force (< 0.01 mV change in driving force for a compartment specific change in  $z$  from  $-0.85$  to  $-0.93$ ), only within that specific compartment of the virtual dendrite. Again, impermeant anion addition resulted in a permanent increase in the volume of the compartment.

These findings suggest that local impermeant anions can adjust the  $\text{Cl}^-$  reversal potential locally, but are not well-placed to cause significant, permanent shifts in the driving force for  $\text{Cl}^-$ . Electrodiffusion may further limit the degree to which changes in impermeant ion charge can modify driving forces through alterations in active ionic transport: the resulting permanent  $\text{Cl}^-$  driving force changes in the multi-compartment model are smaller than the shifts in the single compartment version (Fig. 3.9 C versus Fig. 3.6 B).

### **3.4.3 Addition of local impermeant anions generates volume changes and can model the growth of neuronal processes**

By simulating the influx of impermeant anions in my multi-compartment model of a virtual dendrite I noted that the local increase in impermeant anions results in a permanent increase in volume of the compartment manipulated. On the basis of this observation, I used the addition of impermeant anions to a virtual dendrite to grow a neuronal process (Fig. 3.10). The addition of impermeant anions to the apical compartment or virtual ‘growth cone’, resulted in an increase in the volume and radius of this compartment (Fig. 3.10 A). The addition of impermeant anions in this context can be thought of as representing the transport and tethering of actin to the growth cone. Following growth of the virtual growth cone, the cone’s volume was split between a cone of original dimensions and a new compartment which was added to the body of the now extended neural process. By repeating this process iteratively, I demonstrated how the addition of impermeant anions to the apical compartment of a multi-compartment model successfully recapitulates the growth of a neuronal process.

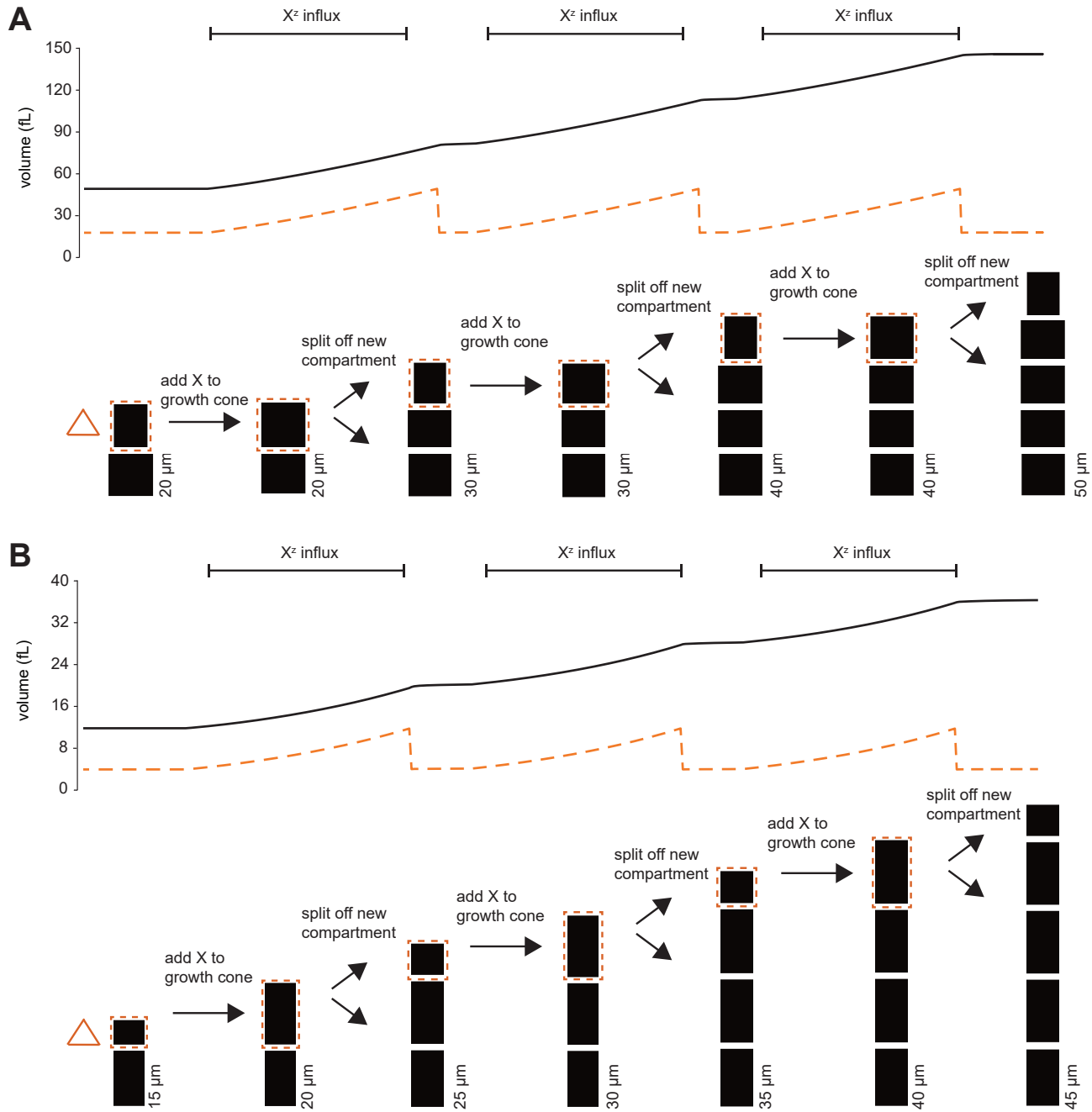


**Figure 3.10:** Addition of impermeant anions could be a mechanism dendritic growth. **(A)** Volume of a virtual dendrite (black) during periodic addition of impermeant anions to a virtual growth cone (dashed orange line) caused the volume of the growth cone to grow; it was then split into a new growth cone of original size and a compartment of height 10  $\mu\text{m}$ . This was repeated iteratively to grow a virtual dendrite. **(B)** Impermeant anion flux as in **A**, however with changes in volume manifested as changes in the height of the compartment rather than the radius. The growth cone is iteratively split into a growth cone of original size and a compartment of height 10  $\mu\text{m}$ .

Because the mechanism in my model and Figure 3.10 A invokes radial growth to compensate for changes in volume, the addition of new compartments could be thought of as a ‘budding off’ process involving volume and membrane rearrangement. To capture an alternative method of dendrite growth, I repeated the process of impermeant anion influx with volume change manifested as changes in the heights of the cylindrical compartments rather than the radii (Fig. 3.10 B). Here, the growth cone simply splits at a determined point once a maximum length is reached, and the two resultant compartments are then linked as separate components via electrodiffusion. No rearrangement or reformation of the membrane would be required for this mechanism, which still illustrates the potential ability of impermeant anions to grow neuronal processes.

### 3.4.4 Local driving force differences modulate the post-synaptic potential when GABA<sub>A</sub> receptors are activated at a synapse

My multi-compartment model has shown that local changes to CCCs can modulate Cl<sup>-</sup> driving force along a sequence of compartments. Meanwhile, local impermeant anion shifts do not significantly affect Cl<sup>-</sup> driving force, but can alter both V<sub>m</sub> and E<sub>Cl</sub> in the same direction in a specific compartment. The Cl<sup>-</sup> flux from GABA<sub>AR</sub>-mediated signalling is proportional to the Cl<sup>-</sup> driving force at the synapse. Therefore, the GABA<sub>AR</sub> inhibitory post-synaptic potential (IPSP) amplitude should not be able to be shifted by impermeant anions. However, the influence of electrodiffusion could alter the passage of Cl<sup>-</sup> flux initiated by a synaptic pulse, especially if there are large sub-cellular differences in V<sub>m</sub> or E<sub>Cl</sub>. I explored the possible impact of electrodiffusion on synaptic transmission by including a GABA<sub>A</sub> synaptic pulse in the multi-compartment model (Fig. 3.11).

A synapse was added to the second dendritic compartment in a ‘ball-and-stick’-style multi-compartment model. The dendrite was 9 compartments long and was attached to another much larger compartment representing the neuron’s soma (see Methods, Section 2.2.2). The synapse was activated for 2 ms and the maximal IPSP amplitudes in each compartment were compared, along with the E<sub>Cl</sub> and V<sub>m</sub> responses at the synapse and soma respectively (control, Fig. 3.11 A). Next, the synaptic pulse was activated in a model in which gKCC2 had been increased to 600  $\mu\text{S}/\text{cm}^2$  in the synaptic compartment, using the same process as in Figure 3.8 B. In this case, the larger initial driving force at the synapse resulted in a larger amplitude IPSP, which was carried through to the soma (Fig. 3.11 B).

To test whether a synaptic input could cause a difference in IPSP amplitude when impermeant anions had been altered, the charge on impermeant intracellular anions was made more negative in the synaptic compartment to reach an average charge of -1.2, using the method from Figure 3.5 A. This is different from the procedure in Fig. 3.9 C, in which impermeant anions were added directly, and was chosen to minimise the influence of a larger, diluting volume in the compartment on the Cl<sup>-</sup> flux from the activated synapse. In this case, the maximal IPSP amplitudes were similar to those of the control (Fig. 3.11 C). This suggests that the Cl<sup>-</sup> driving force determines the outcome of GABA<sub>A</sub> receptor activation even when there are different sub-cellular concentrations of Cl<sup>-</sup> in a dendrite.

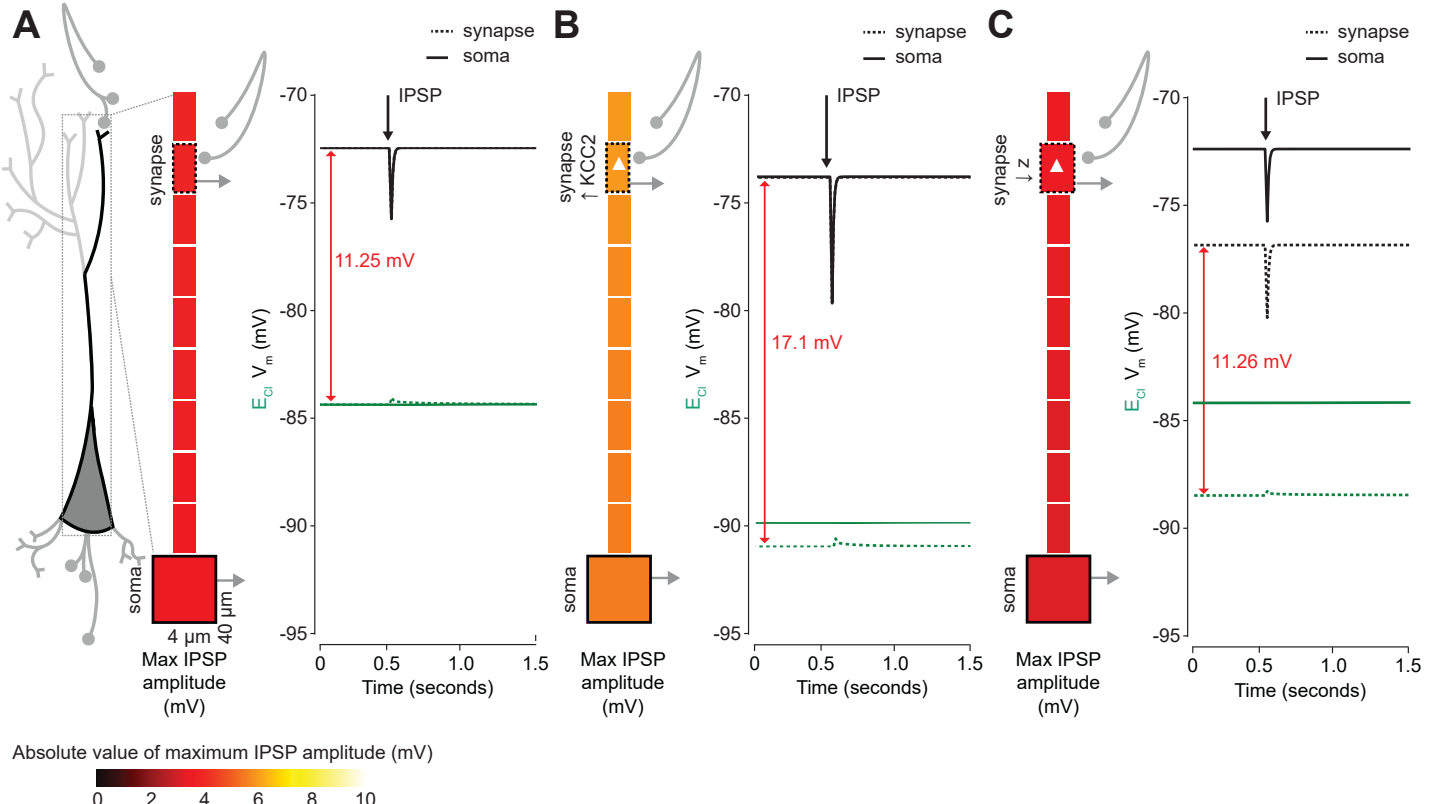


**Figure 3.11:** Local modification of dendritic KCC2 activity and not impermeant anions affects somatic IPSP amplitude in a multi-compartment model employing electrodiffusion. **(A)** A multi-compartment model initialised with a ball-and-stick morphology. The virtual dendrite consists of 9 compartments of initial height 10  $\mu\text{m}$  and radius 0.5  $\mu\text{m}$ , while the soma has height 40  $\mu\text{m}$  and radius 2  $\mu\text{m}$ . Each compartment contained the same mechanisms and default parameterisation as the single compartment model. All ions, except impermeant anions, could move between compartments by electrodiffusion. A synapse was added to the second from top dendritic compartment and was activated for 2 ms, causing an inhibitory post-synaptic potential in the compartment.  $E_{\text{Cl}}$  (green) and  $V_m$  (black) were compared for the IPSP at the synaptic compartment (dashed lines) and upon reaching the soma (solid lines). The initial  $\text{Cl}^-$  driving force for the synaptic compartment is shown in red. The cartoon figure of the model indicates the maximal absolute amplitude of the IPSP generated as compared to resting  $V_m$  in each compartment, corresponding to the colour bar at the bottom of the figure. **(B)** A synapse in a multi-compartment model configured as in **A** was activated after KCC2 strength was increased in the same synaptic compartment, following the methods of Figure 3.8 B. A larger IPSP amplitude than the one in **A** was generated and it resulted in a larger IPSP at the soma. **(C)** A synapse in a multi-compartment model configured as in **A** was activated after the average intracellular charge  $z$  was decreased in the same synaptic compartment, following the methods for the single compartment model in Figure 3.5 A. The IPSP generated had a similar magnitude to the control simulation's IPSP in **A** at the synaptic compartment and along the length of the dendrite to the soma.

# Chapter 4

## Discussion

### 4.1 My computational models provide novel insights into the relative importance of different cellular mechanisms underlying chloride homeostasis in neurons

The driving force for  $\text{Cl}^-$  is a fundamental parameter affecting the excitability of neuronal networks (Raimondo et al., 2017). Recently, impermeant anions, rather than cation-chloride cotransporters (CCCs), have been suggested as the primary determinants of the neuronal driving force for  $\text{Cl}^-$  (Glykys et al., 2014). I explored the determinants of the  $\text{Cl}^-$  driving force in neurons by deriving theoretical models based on biophysical first principles. I show that the  $\text{Na}^+/\text{K}^+$ -ATPase, baseline  $\text{K}^+$ ,  $\text{Na}^+$  and  $\text{Cl}^-$  conductances, average charge on impermeant anions, water permeability and CCCs are all likely contributory in setting neuronal  $[\text{Cl}^-]_i$ . My findings suggest that while impermeant anions can contribute to setting the  $[\text{Cl}^-]_i$  in neurons, they can only affect  $\text{Cl}^-$  driving force by modifying the activity of active transport mechanisms (i.e. the  $\text{Na}^+/\text{K}^+$ -ATPase). Under physiologically relevant conditions, impermeant anions do not alter the  $\text{Cl}^-$  driving force significantly. In contrast, CCCs are well placed to modulate  $\text{Cl}^-$  driving force and hence inhibitory signaling.

Previous theoretical models, which account for the dynamics of  $\text{Cl}^-$  ions, have been useful in determining how changes to the driving force for  $\text{Cl}^-$  are critical for controlling the effect of synaptic inhibition in the brain (Qian and Sejnowski, 1990; Staley and Proctor, 1999; Doyon et al., 2011; Jedlicka et al., 2011; Lewin et al., 2012; Mohapatra et al., 2016) While these models have included the  $\text{Na}^+/\text{K}^+$ -ATPase, the interacting dynamics of several ion species, CCCs (Doyon et al., 2011; Krishnan and Bazhenov, 2011), electrodiffusion (Qian and Sejnowski, 1989) and impermeant anions and volume regulation (Dijkstra et al., 2016), none have combined all of these mechanisms to explore how their combination determines the local driving force for  $\text{Cl}^-$ , as I sought to do.

Theoretical results like mine can both be informed by and confirmed with experimental data. This has great value, as theory can make sense of existing data, and may help predict future research avenues. Therefore, I searched for and designed experiments based on the predictions from my biophysical model. I discuss these with my findings below.

## 4.2 My model confirms the roles of fundamental cellular mechanisms in chloride homeostasis

### 4.2.1 The $\text{Na}^+/\text{K}^+$ -ATPase

My theoretical approach is based on the pump-leak formulation (Tosteson and Hoffman, 1960). It suggests that mammalian cells maintain their volume under osmotic stress generated by impermeant anions and the Donnan effect by employing active transport of  $\text{Na}^+$  and  $\text{K}^+$  using the  $\text{Na}^+/\text{K}^+$ -ATPase (Armstrong, 2003; Kay, 2017). A Donnan equilibrium, a true thermodynamic equilibrium requiring no energy to maintain it, is not possible in cells such as neurons which have pliant membranes (Sperelakis, 2012).

My model conforms to the pump-leak formulation: abolishing the activity of the  $\text{Na}^+/\text{K}^+$ -ATPase leads to cell swelling, progressive membrane depolarisation and rundown of ionic gradients, including that of  $\text{Cl}^-$  (Fig. 3.1 C and D). The  $\text{Na}^+/\text{K}^+$  ATPase is a fundamental cellular parameter that stabilises cell volume and determines all ionic gradients including that of  $\text{Cl}^-$  and hence must be considered in any attempt to model ion homeostasis. However, I show that above a certain level of  $\text{Na}^+/\text{K}^+$ -ATPase activity, even many-fold changes in pump rate have minimal effects on volume,  $E_{\text{Cl}}$  and  $V_m$  (Fig. 3.1 D), as hinted in kinetic and inhibitory studies (Hamada et al., 2003; Baker and Willis, 1972). This may explain recent experimental findings in which periods of  $\text{Na}^+/\text{K}^+$ -ATPase inhibition using ouabain caused modest changes to cell volume (Glykys et al., 2014). It therefore seems unlikely that neurons adjust the  $\text{Na}^+/\text{K}^+$ -ATPase as a means for modulating  $\text{Cl}^-$  driving force.

### 4.2.2 Passive ionic conductances

Baseline ion conductances are other important factors that affect  $\text{Cl}^-$  driving force. My model is consistent with recent experimental results that demonstrate that increased neuronal  $\text{Na}^+$  conductance (for example by activating NMDA receptors, or preventing closure of voltage-gated  $\text{Na}^+$  channels), leads to progressive neuronal swelling, membrane depolarisation and  $\text{Cl}^-$  accumulation (Rungta et al., 2015). These are the primary pathological processes in cytotoxic oedema (Liang et al., 2007). I also show that tonic neuronal  $\text{Cl}^-$  conductance only affects baseline  $[\text{Cl}^-]_i$  and driving force in the presence of CCCs. Without active  $\text{Cl}^-$  flux, which CCCs provide, there is no driving force for passive  $\text{Cl}^-$  flux and hence no mechanism for  $[\text{Cl}^-]_i$  changes resulting from selective modification of  $\text{Cl}^-$  conductance.

That active CCCs are required to generate a  $\text{Cl}^-$  driving force is consistent with both classic (Misgeld et al., 1985; Thompson and Gähwiler, 1989) and recent experimental findings using CCC inhibitors (Lee et al., 2011; Berglund et al., 2016). Furthermore, validation was sought from data by Wright et al. (2017), which was re-analysed by Dr Richard Burman of the Raimondo Lab. 1 mM furosemide was used to block the activity of KCC2 and the cell's response measured using gramicidin perforated patch-clamping (Fig. 4.1 A). As predicted by my model (Fig. 3.2 D and 3.6 F), the furosemide drove a significant shift in the  $\text{Cl}^-$  driving force towards 0 with little effect on  $V_m$  (Fig. 4.1 B and C).

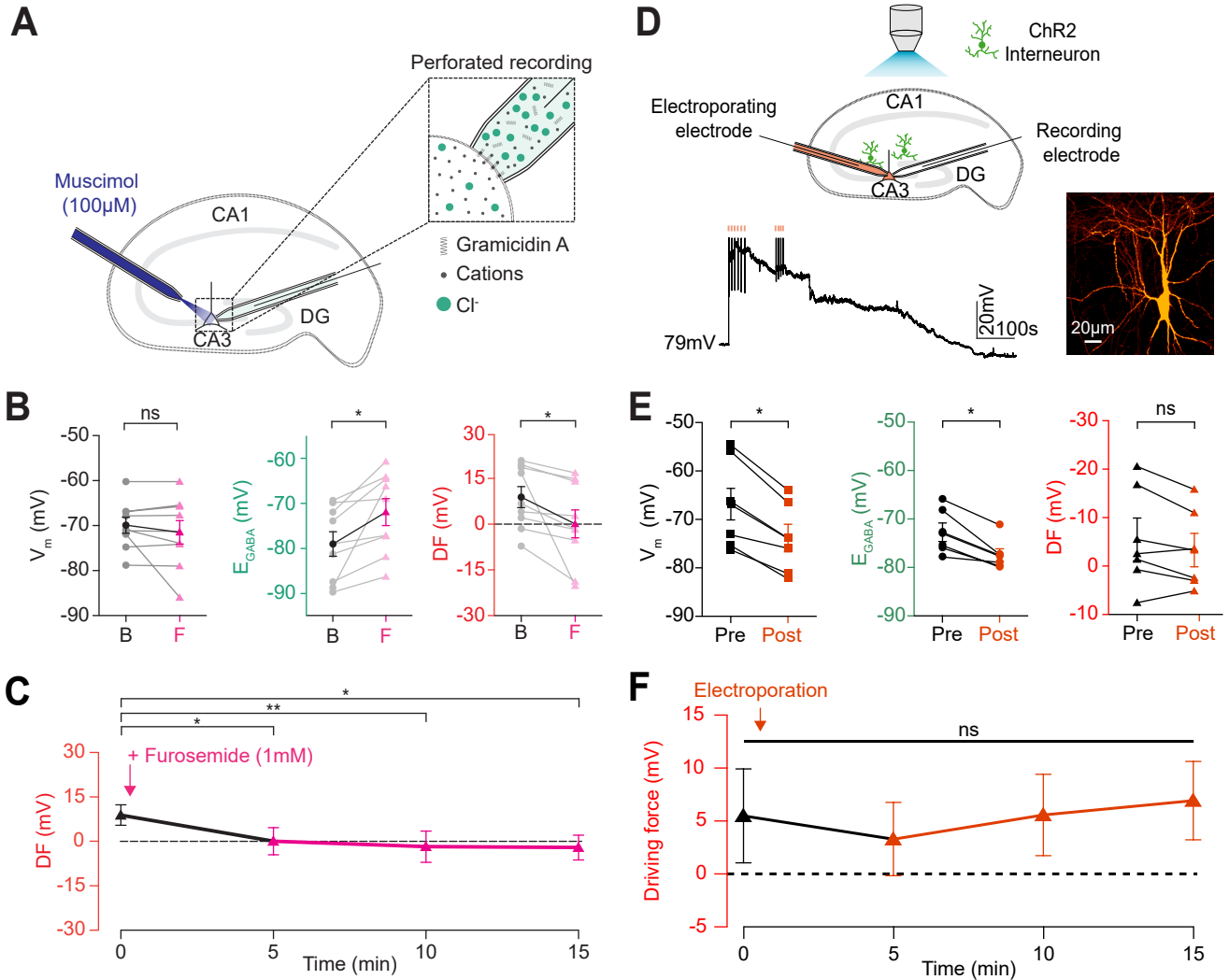


**Figure 4.1:** Experimental evidence confirms the role of cation-chloride cotransporters (CCCs) but not impermeant anions in setting the chloride driving force (DF). Left column (**A, B, C**), furosemide (CCC) experiment; right column (**D, E, F**), electroporation (impermeant anion) experiment. Modified from Düsterwald et al. (2017) (in review). (**A**) Schematic showing experimental setup for the furosemide experiment. Gramicidin perforated patch-clamp recordings were performed on CA3 pyramidal cells from rat hippocampal organotypic brain slices. Cl<sup>-</sup> permeable GABA<sub>A</sub> receptors were activated with muscimol (10  $\mu$ M). (**B**) Population data showing significant changes in  $E_{GABA}$  and DF but not  $V_m$  five minutes after furosemide application. (**C**) Changes in DF over time showed a significant increase from baseline once furosemide was introduced. (**D**) Top, schematic showing experimental setup for the electroporation experiment. Whole-cell recordings were made from CA3 pyramidal cells in mouse organotypic brain slices. Impermeant anions (orange) were delivered via electroporation of the negatively charged fluorescent dextran Alexa Flour 488 through a pipette positioned near the soma of the recorded cell. GABA<sub>A</sub>R currents were elicited via photo-activation of ChR2-expressing GAD2+ interneurons (green cells) in the presence of 5  $\mu$ M CGP-35348 to block GABA<sub>B</sub>Rs. Lower trace left, example current clamp recording showing  $V_m$  changes during electroporation of anionic dextran. Right, confocal image demonstrating cell-localised fluorescence of the anionic dextran electroporated (orange content). (**E**) Population data showing significant decreases in mean  $V_m$  and  $E_{GABA}$  but not DF five minutes after the electroporation of impermeant anions. (**F**) Changes in DF over time showed no significant change from baseline with or after impermeant anion electroporation. The point at which electroporation occurred is marked with an orange arrow. ‘ns’, nonsignificant; \*  $p < 0.05$ ; \*\*  $p < 0.01$ .

## **4.3 Cation-chloride cotransporters can modulate changes in chloride driving force in my biophysical model**

### **4.3.1 KCC2 activity modulates chloride driving force specifically, in agreement with experimental evidence**

In my model, elevating the activity of KCC2, the most active CCC in mature neurons (Ben-Ari, 2002), increases the driving force for  $\text{Cl}^-$  by shifting the reversal potential for  $\text{Cl}^-$  closer to that of  $\text{K}^+$ . Interestingly, large shifts ( $\approx 7 \text{ mV}$ ) in driving force were associated with very minor (1%) changes in volume or membrane potential. Elevating KCC2 activity in a compartment in a dendritic multi-compartment model resulted in increased  $\text{Cl}^-$  driving force and higher amplitude somatic inhibitory post-synaptic potentials compared to control when  $\text{GABA}_A$  receptors were activated (Fig. 3.11 B). As such, modulating KCC2 represents a specific means for manipulating the neuronal  $\text{Cl}^-$  driving force and  $\text{GABA}_A$  synaptic signalling (Fig. 4.2 A). This is consistent with traditional dogma and recent and previous experimental results (Kaila et al., 2014; Klein et al., 2018).

Furthermore, my meta-analysis of numerous experimental studies showed a strong correlation between change in KCC2 expression and  $\text{Cl}^-$  driving force, but not between KCC2 expression and  $V_m$  (Fig. 3.3 D). The outlier in the meta-analysis was from a study based on an acute stress state, which can cause transient dynamic shifts in multiple cellular parameters (Hewitt et al., 2009), and hence the association may have been obscured. My model compared favourably to the meta-analysis's trend when a logarithmic scale was chosen for  $g_{\text{KCC2}}$ , representing KCC2 'strength' or expression level (Fig. 3.3 E). Further consideration of the  $\text{Cl}^-$  dynamics from the additional expression of KCC2 proteins on the membrane of the same cell with unchanged surface area and volume is needed to explain why a logarithmic scale produced a better fit to the data. Additionally, the trends of alternative KCC2 models could be compared against the meta-analysis's line-of-best-fit.

NKCC1 was not included in my model because it is less abundant in adult neurons. Since NKCC1 also uses cation gradients established by the  $\text{Na}^+/\text{K}^+$ -ATPase to transport  $\text{Cl}^-$ , it should behave similarly to KCC2. Inclusion of NKCC1 in future work may enable better fitting of the model to data and improved understanding of CCCs' role in  $\text{Cl}^-$  regulation.

### **4.3.2 KCC2 can mediate volume shifts without explicitly cotransporting water**

Moderate transmembrane water movement occurred with KCC2 activity changes in the biophysical model, although water cotransport through CCCs was not explicitly incorporated (Delpire and Staley, 2014). These shifts occurred via the membrane's natural permeability to water (Fettiplace and Haydon, 1980; Hernández and Cristina, 1998) rather than specific water-permeable channels (aquaporins), which are thought not to be expressed in neurons (Andrew et al., 2007). The result implies that CCCs could indirectly mediate volume shifts secondary to their active flux of cations and  $\text{Cl}^-$ , but would not be responsive to osmotic

gradients themselves. For example, there are different steady state directions in volume shift in my model when adding extracellular impermeant anions, which increase osmolarity without affecting K-Cl cotransport, as opposed to permeable KCl, which switches the direction of K-Cl cotransport and increases osmolarity (Fig. 3.5 E and F). Notably, some of the experimental results implicating CCC water cotransport, for example cellular volume increase with extracellular KCl addition, can also be explained using my model, which does not require CCC-water coupled transport (Steffensen et al., 2018).

#### **4.3.3 KCC2 can only modulate local differences in chloride driving force under conditions of constrained electrodiffusion**

Using the multi-compartment model, which incorporated electrodiffusion, I found that local modification of KCC2 activity has a specific local effect on  $\text{Cl}^-$  driving force that is dependent on the characteristics of intracellular  $\text{Cl}^-$  diffusion (Fig. 3.8 C). Cytoplasmic  $\text{Cl}^-$  diffusion rates had to be reduced substantially before I observed local changes in  $\text{Cl}^-$  driving force driven by KCC2 (Qian and Sejnowski, 1989; Kuner and Augustine, 2000; Mohapatra et al., 2016; Savtchenko et al., 2017). While differences in KCC2 activity might generate a gradient for  $\text{Cl}^-$  driving force between large subcellular structures (i.e. dendrites versus soma), my modelling results call into question the idea of synapse-specific  $\text{Cl}^-$  regulation within the same cellular domain (Földy et al., 2011). However, previous modelling work has predicted that KCC2 ought to be more effective at local  $\text{Cl}^-$  regulation when mechanisms like dendritic spines and tortuosity, which slow-down  $\text{Cl}^-$  diffusion, are included (Mohapatra et al., 2016). The effect of these mechanisms could be explored in detail in future work.

### **4.4 Impermeant anions cannot appreciably modify the chloride driving force**

#### **4.4.1 Even under conditions of osmotic strain, impermeant anion concentration changes do not appreciably modify chloride driving force**

Glykys et al. (2014) used  $\text{Cl}^-$  imaging and various experimental manipulations to claim that  $[X]_i$  and  $[X]_o$  set  $[\text{Cl}^-]_i$  and the  $\text{Cl}^-$  driving force. From my theoretical analysis, I find that modifying the amount of impermeant anions inside or outside of neurons has no persistent effect on  $[\text{Cl}^-]_i$  or  $\text{Cl}^-$  driving force, unless I include mechanisms that allow a transmembrane osmotic pressure differential to develop that indirectly affects active transport mechanisms. Even in this case, under transmembrane pressure differentials that do not lyse the membrane (Nichol and Hutter, 1996),  $\text{Cl}^-$  driving force changes are negligible ( $< 1 \text{ mV}$ ) (Fig. 3.6 D). As proven by the congruence of the membrane stretch model that I employed (2.9) with my analytical solution, which includes transmembrane osmotic differences, the actual mechanism for the development of a pure osmotic pressure differential does not affect the steady state values except for volume.

In my model I assumed that water can pass through the neuronal membrane to equalise osmotic differences. Although it is thought that some neurons do not express aquaporin channels (Andrew et al., 2007), water can permeate through the phospholipid bilayer (Fet- tiplace and Haydon, 1980; Hernández and Cristina, 1998). Therefore, while differences in neuronal water permeability might affect the time taken to reach a steady state, the values at steady state themselves are likely to be similar.

Recent work has suggested that the viscoelastic properties of the cellular cytoskeleton could allow it to take up osmotic shifts created by impermeant anion movement, as if the cytoskeleton had properties like a sponge (Sachs and Sivaselvan, 2015). This would mean that one would not see volume shifts as large as predicted by my model, while allowing for big transmembrane osmotic differentials to exist without bursting the cell (Nichol and Hutter, 1996).

As discussed in Section 4.3.2, it has been suggested that water itself might contribute to the energetics of ion transport by CCCs, via coupled transport of water and ions (Delpire and Staley, 2014). If this were the case, impermeant anion induced changes to the trans- membrane osmotic gradient could generate changes to the  $\text{Cl}^-$  driving force via CCCs. However, this idea is controversial, and this exception aside, I conclude that  $[\text{Cl}^-]_i$  and the  $\text{Cl}^-$  driving force are not determined by the concentration of impermeant anions.

#### 4.4.2 Modification of impermeant anions' average charge can cause shifts in the chloride gradient, but cannot significantly shift the chloride driving force

My theoretical findings offer a potential explanation for recent experimental observations in which changes in  $[\text{Cl}^-]_i$  were noted with the addition of impermeant anions. I show that modifying the average charge on impermeant anions (i.e.  $z$  in  $[\text{X}^z]_i$ ), rather than their concentration, can affect  $[\text{Cl}^-]_i$  and  $E_{\text{Cl}}$  (Fig. 4.2 B and C). Relating this to prior experimental observations, Glykys et al. (2014) used SYTO64 staining of nucleic acids and perfusion of weak organic acids in conjunction with  $\text{Cl}^-$  imaging to suggest that  $[\text{Cl}^-]_i$  depends on internal impermeant anions ( $[\text{X}]_i$ ). If such a manipulation modifies the average charge on intracellular impermeant anions, and not concentration per se, this could account for the observed changes in  $[\text{Cl}^-]_i$ .

Glykys et al. (2014) did not measure  $V_m$  or the  $\text{Cl}^-$  driving force in these experiments. The clear prediction from my model is that any manipulation which changes the average charge of impermeant anions would not appreciably affect the  $\text{Cl}^-$  driving force because any impermeant anion driven change on  $E_{\text{Cl}}$  is matched by an equivalent effect on  $V_m$  due to accompanying shifts in cation concentrations. Although my multi-compartment model suggests that these shifts could cause differences in local  $[\text{Cl}^-]_i$  and  $V_m$  at adjacent regions in a dendrite, there is a negligible effect on the size of the inhibitory post-synaptic potential generated in adjacent compartments when a GABA<sub>A</sub> synapse is activated in this set-up (Fig. 3.11 C). In addition, the IPSP recorded at the soma following local dendritic modification of impermeant anions is almost identical to that recorded under control conditions. This

serves to confirm that local modifications of impermeant anions have a negligible effect on the properties of inhibitory synaptic transmission.

Experimental validation was sought for this prediction by Dr Richard Burman (Düsterwald et al., 2017), who used photo-activation of ChR2 expressing GABAergic interneurons and whole-cell patch clamp recordings of mouse organotypic CA3 hippocampal pyramidal neurons to measure  $V_m$ ,  $E_{GABA}$ , and driving force before and after addition of impermeant anions via single cell electroporation of fluorescently tagged anionic dextrans (Fig. 4.1 D). He showed that while  $E_{GABA}$  can be shifted by addition of impermeant anions using electroporation of membrane impermeant anionic dextrans,  $V_m$  is shifted in a similar direction resulting in an undetectable change in  $Cl^-$  driving force (Fig. 4.1 E and F). The results are qualitatively remarkably similar to my model's prediction of the effects of impermeant anion addition (Fig. 3.5 A).

#### 4.4.3 Impermeant anion-driven shifts in chloride homeostasis are secondary to alterations to active ionic transport kinetics

Given prior theoretical predictions (Kaila et al., 2014; Voipio et al., 2014; Savtchenko et al., 2017), it is interesting that my model reveals that changing impermeant anions could affect the  $Cl^-$  driving force at all. I found that the small ( $< 1$  mV) impermeant anion-driven changes in  $Cl^-$  driving force observed in my model were caused by indirect effects on  $Na^+$  concentration and hence  $Na^+/K^+$ -ATPase activity (Fig. 3.6). The impermeant anion-driven changes in  $Cl^-$  driving force are even smaller in the multi-compartment model ( $< 0.1$  mV), in which electrodiffusion allows local changes in  $Na^+$  to dissipate (Fig. 3.9 C).

When  $Na^+/K^+$ -ATPase activity was decoupled from the transmembrane  $Na^+$  gradient, I found that impermeant anions were unable to cause persistent shifts in  $Cl^-$  driving force in agreement with theory (Kaila et al., 2014; Voipio et al., 2014). It is important to note that these small, impermeant anion- $Na^+/K^+$ -ATPase-driven shifts in  $Cl^-$  driving force are dependent on the presence of cation-chloride cotransport in the form of KCC2 and would entail changes in energy use by the  $Na^+/K^+$ -ATPase. In other words, active transport mechanisms are again required to drive changes in  $Cl^-$  homeostasis.

These anion-based shifts also caused increases in cell volume, in agreement with the observations of Glykys et al. (2014). In the controlled environment of the brain, this side effect may be an additional disincentive for the use of anion modification to alter  $Cl^-$  homeostasis specifically. The volume changes may however reflect an important cellular function of impermeant anion transport: neurons could use the transport and tethering of impermeant anions to grow or modify the volume of particular neuronal compartments (Fig. 3.10).

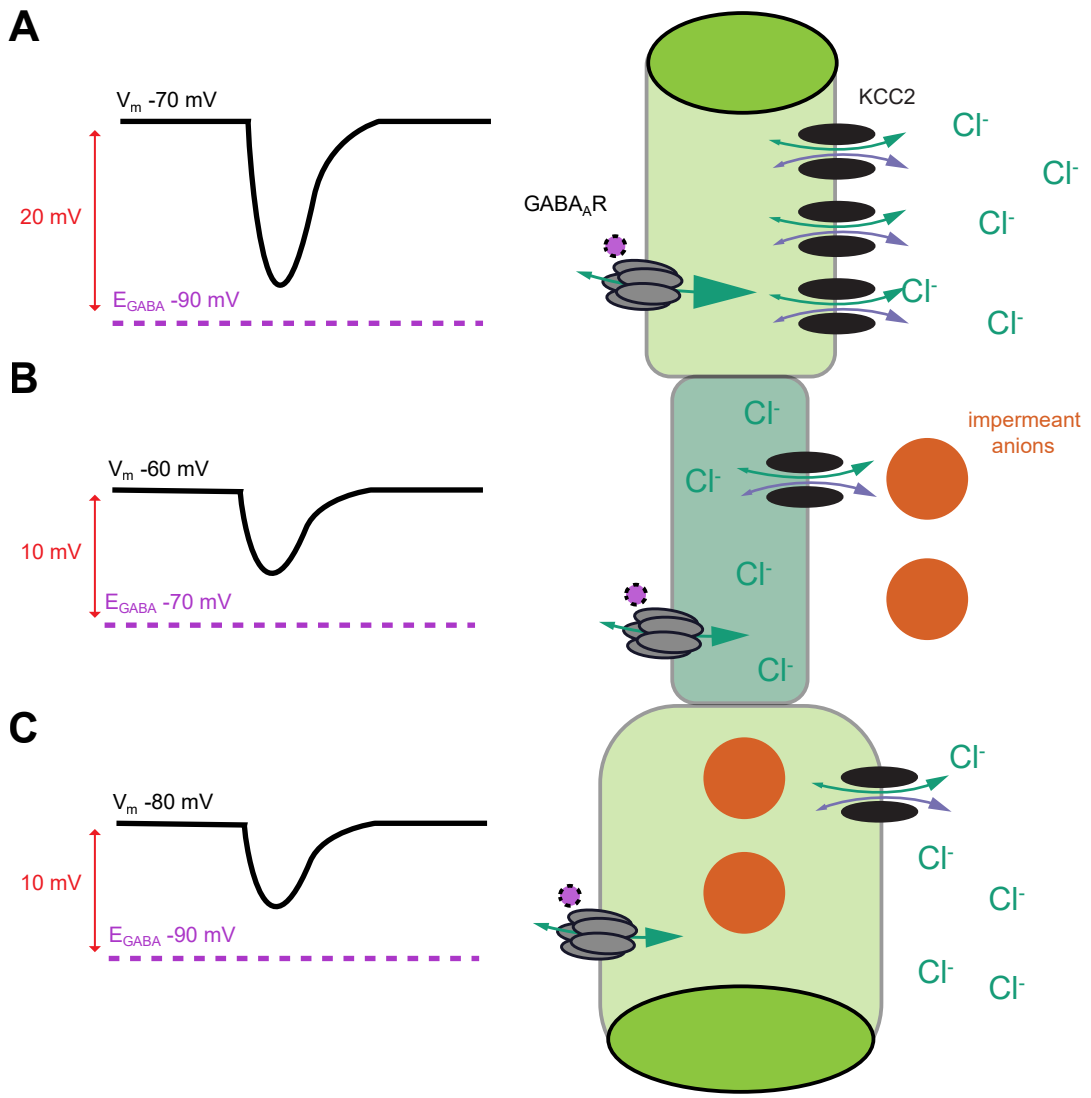


**Figure 4.2:** The respective influences of cation-chloride cotransporters and impermeant anions on chloride homeostasis — three possible cellular arrangements that all result in inhibitory GABA signalling. (A) Increased activity of the cation-chloride cotransporter KCC2 can drive changes in the Cl<sup>-</sup> driving force (red arrows) by reducing intracellular [Cl<sup>-</sup>]<sub>i</sub> and shifting  $E_{GABA}$  (purple) negatively, thus encouraging inward Cl<sup>-</sup> flux during GABA<sub>A</sub>R activation. Larger driving forces result in greater hyperpolarisations when GABA<sub>A</sub>Rs are activated. (B) Increased extracellular concentrations of impermeant anions (orange) cannot drive changes in driving force because increases in [Cl<sup>-</sup>]<sub>i</sub> and  $E_{GABA}$  are met with equal increases in  $V_m$  (black). Therefore, inward Cl<sup>-</sup> flux occurs at the usual magnitude during GABA<sub>A</sub>R activation. (C) Increased intracellular concentrations of impermeant anions also cannot drive changes in driving force because decreases in [Cl<sup>-</sup>]<sub>i</sub> and  $E_{GABA}$  are met with equal decreases in  $V_m$ . Therefore, inward Cl<sup>-</sup> flux again occurs at a typical magnitude during GABA<sub>A</sub>R activation.

#### 4.4.4 Outlook for future evaluation of impermeant anions' role in chloride homeostasis

Taken together, my modelling results about impermeant anions and how they might affect  $\text{Cl}^-$  homeostasis are congruent with prior *in vitro* experiments, which did not measure  $\text{Cl}^-$  driving force but did note changes in  $E_{\text{Cl}}$  (Glykys et al., 2014; Klein et al., 2018). These experiments were done in sliced brain tissue with extracellular environments resembling my model's — essentially infinite in volume with fixed ion concentrations. Variation between *in vitro* and *in vivo*  $\text{Cl}^-$  concentration measurements has been identified (Valeeva et al., 2016). It is important to expand future theoretical and experimental work to environments that more closely resemble the brain *in vivo*, i.e. extracellular protein matrices, glia, blood vessels, cerebrospinal fluid resorption mechanisms and small extracellular fluid-filled spaces between cells (Savtchenko et al., 2017; Lei et al., 2017).

Other conditions that might affect the neuronal  $\text{Cl}^-$  driving force and ought to be modelled include bicarbonate dynamics through  $\text{Cl}^-$  channels and pH buffering systems using carbonic anhydrase (Kaila et al., 2014), and local electrodiffusion in 3-dimensions (Savtchenko et al., 2017). The latter has implications for whether neurons might tune tortuosity and the distributions of  $\text{GABA}_A$  leak channels and CCCs to maintain different  $\text{Cl}^-$  driving forces in different dendrites or parts of dendrites. Further exploration of the spatiotemporal spread of chloride ions in inhibitory signalling incorporating other dynamics like voltage-gated channels is also warranted. Large-scale models of multiple cells to explore how  $\text{Cl}^-$  driving force is affected in disease processes like meningitis and stroke would also be useful.

### 4.5 Conclusion

In summary, my theoretical model, which was derived from well-established biophysical principles, is consistent with theoretical predictions, new experimental data and previous work (Glykys et al., 2014; Kaila et al., 2014; Klein et al., 2018). However, my model offers an alternative interpretation of previous anion-manipulation experiments, which did not consider the parameter most importance for GABAergic signalling, the  $\text{Cl}^-$  driving force (Glykys et al., 2014). My results confirm the utility of the pump-leak model for investigating mechanisms underlying  $\text{Cl}^-$  homeostasis in neurons. My model suggests that impermeant anions alone cannot shift  $\text{Cl}^-$  out of equilibrium across the neuronal membrane, either locally or cell-wide. Were neurons to alter impermeant anion concentrations or charge, the resting membrane potential would be modified with little effect on the  $\text{Cl}^-$  driving force or properties of  $\text{GABA}_A$ -mediated synaptic signalling. My work confirms the central importance of cation-chloride cotransport activity in determining the effects of inhibitory synaptic transmission in the nervous system. Finally, it highlights the value and ability of theory to learn from and inform experimental studies.



# References

- Alessi DR, Zhang J, Khanna A, Hochdörfer T, Shang Y & Kahle KT (2014). The WNK-SPAK/OSR1 pathway: master regulator of cation-chloride cotransporters. *Sci. Signal.* **7**, re3.
- Ambros-Ingerson J & Holmes WR (2005). Analysis and comparison of morphological reconstructions of hippocampal field CA1 pyramidal cells. *Hippocampus* **15**, 302–15.
- Amini B, Clark JW & Canavier CC (1999). Calcium Dynamics Underlying Pacemaker-Like and Burst Firing Oscillations in Midbrain Dopaminergic Neurons: A Computational Study. *Journal of Neurophysiology* **82**, 2249–2261.
- Andersen P, Dingledine R, Gjerstad L, Langmoen I & Laursen M (1980). Two different responses of hippocampal pyramidal cells to application of gamma-amino butyric acid. *J. Physiol.* **305**, 279–96.
- Andrew RD, Labron MW, Boehnke SE, Carnduff L & Kirov SA (2007). Physiological evidence that pyramidal neurons lack functional water channels. *Cereb. Cortex* **17**, 787–802.
- Armstrong CM (2003). The Na/K pump, Cl<sup>-</sup> ion, and osmotic stabilization of cells. *Proceedings of the National Academy of Sciences of the United States of America* **100**, 6257–6262.
- Arosio D & Ratto GM (2014). Twenty years of fluorescence imaging of intracellular chloride. *Front. Cell. Neurosci.* **8**, 258.
- Baker PF & Willis JS (1972). Inhibition of the sodium pump in squid giant axons by cardiac glycosides: dependence on extracellular ions and metabolism. *Journal of Physiology* **224**, 463–475.
- Balakrishnan V, Becker M, Lörhrke S, Nothwang HG, Güresir E & Friauf E (2003). Expression and Function of Chloride Transporters during Development of Inhibitory Neurotransmission in the Auditory Brainstem. *J. Neurosci.* **23**, 4134–4145.
- Barmashenko G, Hefft S, Aertsen A, Kirschstein T & Köhling R (2011). Positive shifts of the GABA<sub>A</sub> receptor reversal potential due to altered chloride homeostasis is widespread after status epilepticus. *Epilepsia* **52**, 1570–8.
- Ben-Ari Y (2002). Excitatory actions of GABA during development: the nature of the nurture. *Nat. Rev. Neurosci.* **3**, 728–39.
- Berglund K, Wen L, Dunbar RL, Feng G & Augustine GJ (2016). Optogenetic Visualization of Presynaptic Tonic Inhibition of Cerebellar Parallel Fibers. *Journal of Neuroscience* **36**, 5709–5723.

- Bertolini C, Murana E, Mosca L, D'Erme M, Scala F, Franciosi A, Catalano M, Limatola C, Bregestovski P, Di Angelantonio S & Ragozzino D (2012). Transient increase in neuronal chloride concentration by neuroactive aminoacids released from glioma cells. *Front. Mol. Neurosci.* **5**, 100.
- Blaesse P, Airaksinen MS, Rivera C & Kaila K (2009). Cation-chloride cotransporters and neuronal function. *Neuron* **61**, 820–38.
- Bormann J, Hamill OP & Sakmann B (1987). Mechanism of anion permeation through channels gated by glycine and gamma-aminobutyric acid in mouse cultured spinal neurones. *J. Physiol.* **385**, 243–286.
- Bragin DE, Sanderson JL, Peterson S, Connor JA & Müller WS (2010). Development of epileptiform excitability in the deep entorhinal cortex after status epilepticus. *Eur J Neurosci* **30**, 611–624.
- Campbell SL, Robel S, Cuddapah VA, Robert S, Buckingham SC, Kahle KT & Sontheimer H (2015). GABAergic disinhibition and impaired KCC2 cotransporter activity underlie tumor-associated epilepsy. *Glia* **63**, 23–36.
- Cesetti T, Ciccolini F & Li Y (2011). GABA Not Only a Neurotransmitter: Osmotic Regulation by GABA<sub>A</sub>R Signaling. *Front. Cell. Neurosci.* **6**, 3.
- Chen Q, Moulder K, Tenkova T, Hardy K, Olney JW & Romano C (1999). Excitotoxic cell death dependent on inhibitory receptor activation. *Exp. Neurol.* **160**, 215–25.
- Chen SR, Zhu L, Chen H, Wen L, Laumet G & Pan HL (2014). Increased spinal cord Na-K-2Cl cotransporter-1 (NKCC1) activity contributes to impairment of synaptic inhibition in paclitaxel-induced neuropathic pain. *J. Biol. Chem.* **289**, 31111–20.
- Conti L, Palma E, Roseti C, Lauro C, Cipriani R, de Groot M, Aronica E & Limatola C (2011). Anomalous levels of Cl<sup>-</sup> transporters cause a decrease of GABAergic inhibition in human peritumoral epileptic cortex. *Epilepsia* **52**, 1635–1644.
- Coombs JS, Eccles JC & Fatt P (1955). The specific ionic conductances and the ionic movements across the motoneuronal membrane that produce the inhibitory post-synaptic potential. *The Journal of physiology* **130**, 326–374.
- Corless RM, Gonnet GH, Hare DEG, Jeffrey DJ & Knuth DE (1996). On the Lambert W function. *Advances in Computational Mathematics* **5**, 329–359.
- Coull JAM, Boudreau D, Bachand K, Koninck PD, Prescott SA, Nault F, Koninck YD & Sik A (2003). Trans-synaptic shift in anion gradient in spinal lamina I neurons as a mechanism of neuropathic pain. *Nature* **424**, 938–942.
- Cruz GE, Sahley CL & Muller KJ (2007). Neuronal competition for action potential initiation sites in a circuit controlling simple learning. *Neuroscience* **148**, 65–81.
- Dai J, Sheetz MP, Wan X & Morris CE (1998). Membrane Tension in Swelling and Shrinking Molluscan Neurons. *The Journal of Neuroscience* **18**, 6681–6692.
- DeFazio RA, Keros S, Quick MW & Hablitz JJ (2000). Potassium-Coupled Chloride Cotransport Controls Intracellular Chloride in Rat Neocortical Pyramidal Neurons. *J. Neurosci.* **20**, 8069–8076.

- Delpire E & Staley KJ (2014). Novel determinants of the neuronal Cl<sup>-</sup> concentration. *J. Physiol.* **592**, 4099–114.
- Destexhe A, Mainen ZF & Sejnowski TJ (1994). An Efficient Method for Computing Synaptic Conductances Based on a Kinetic Model of Receptor Binding. *Neural Computation* **6**, 14–18.
- Di Angelantonio S, Murana E, Cocco S, Scala F, Bertolini C, Molinari MG, Lauro C, Bregestovski P, Limatola C & Raguzzino D (2014). A role for intracellular zinc in glioma alteration of neuronal chloride equilibrium. *Cell Death Dis.* **5**, e1501.
- Dierkes PW, Wüsten HJ, Klees G, Müller A & Hochstrate P (2006). Ionic mechanism of ouabain-induced swelling of leech Retzius neurons. *Pflugers Archiv European Journal of Physiology* **452**, 25–35.
- Dijkstra K, Hofmeijer J, van Gils SA & van Putten MJ (2016). A Biophysical Model for Cytotoxic Cell Swelling. *The Journal of Neuroscience* **36**, 11881–11890.
- Doyon N, Prescott Sa, Castonguay A, Godin AG, Kröger H & De Koninck Y (2011). Efficacy of Synaptic Inhibition Depends on Multiple, Dynamically Interacting Mechanisms Implicated in Chloride Homeostasis. *PLoS Computational Biology* **7**, e1002149.
- Doyon N, Vinay L, Prescott SA & De Koninck Y (2016). Chloride Regulation: A Dynamic Equilibrium Crucial for Synaptic Inhibition. *Neuron* **89**, 1157–1172.
- Düsterwald KM, Currin CB, Burman RJ, Akerman CJ, Kay AR & Raimondo JV (2017). Biophysical models reveal the relative importance of transporter proteins and impermeant anions in chloride homeostasis. *bioRxiv*.
- Dzhala VI, Talos DM, Sdrulla Da, Brumback AC, Mathews GC, Benke Ta, Delpire E, Jensen FE & Staley KJ (2005). NKCC1 transporter facilitates seizures in the developing brain. *Nat. Med.* **11**, 1205–13.
- Ellender TJ, Raimondo JV, Irkle A, Lamsa KP & Akerman CJ (2014). Excitatory effects of parvalbumin-expressing interneurons maintain hippocampal epileptiform activity via synchronous afterdischarges. *J. Neurosci.* **34**, 15208–22.
- Ferrini F, Trang T, Mattioli TAM, Laffray S, Del'Guidice T, Lorenzo LE, Castonguay A, Doyon N, Zhang W, Godin AG, Mohr D, Beggs S, Vandal K, Beaulieu JM, Cahill CM, Salter MW & De Koninck Y (2013). Morphine hyperalgesia gated through microglia-mediated disruption of neuronal Cl<sup>-</sup> homeostasis. *Nat. Neurosci.* **16**, 183–92.
- Fettiplace R & Haydon DA (1980). Water permeability of lipid membranes. *Physiological reviews* **60**, 510–50.
- Fiumelli H, Cancedda L & Poo Mm (2005). Modulation of GABAergic transmission by activity via postsynaptic Ca<sup>2+</sup>-dependent regulation of KCC2 function. *Neuron* **48**, 773–86.
- Földy C, Lee S, Morgan R & Soltesz I (2011). Regulation of fast-spiking basket cell synapses by the chloride channel CIC-2. *Nature Neuroscience* **13**, 1047–1049.
- Forsythe ID & Redman SJ (1988). The Dependence of the Motoneurone Membrane Potential on Extracellular Ion Concentrations Studied in Isolated Rat Spinal Cord. *Journal of Physiology* **404**, 83–99.

Fraser JA & Huang CLH (2004). A quantitative analysis of cell volume and resting potential determination and regulation in excitable cells. *The Journal of physiology* **559**, 459–78.

Friauf E, Wenz M, Oberhofer M, Nothwang HG, Balakrishnan V, Knipper M & Lörke S (2008). Hypothyroidism impairs chloride homeostasis and onset of inhibitory neurotransmission in developing auditory brainstem and hippocampal neurons. *Eur. J. Neurosci.* **28**, 2371–80.

Funk K, Woitecki A, Franjic-Würtz C, Gensch T, Möhrlen F & Frings S (2008). Modulation of chloride homeostasis by inflammatory mediators in dorsal root ganglion neurons. *Mol. Pain* **4**, 32.

Gabbiani F, Midtgaard J & Knöpfel T (1994). Synaptic integration in a model of cerebellar granule cells. *Journal of neurophysiology* **72**, 999–1009.

Galeffi F, Sah R, Pond BB, George A & Schwartz-Bloom RD (2004). Changes in intracellular chloride after oxygen-glucose deprivation of the adult hippocampal slice: effect of diazepam. *J. Neurosci.* **24**, 4478–88.

Ganguly K, Schinder AF, Wong ST, Poo Mm, Diego S & Jolla L (2001). GABA Itself Promotes the Developmental Switch of Neuronal GABAergic Responses from Excitation to Inhibition. *Cell* **105**, 521–532.

Gentiletti D, Suffczynski P, Gnatkovsky V & de Curtis M (2017). Changes of Ionic Concentrations During Seizure Transitions — A Modeling Study. *International Journal of Neural Systems* **27**, 1750004.

Gillen CM, Brill S, Payne JA & Forbush III B (1996). Molecular cloning and functional expression of the K-Cl cotransporter from rabbit, rat, and human. *J. Biol. Chem.* **271**, 16237–16244.

Glickfeld LL, Roberts JD, Somogyi P & Scanziani M (2009). Interneurons hyperpolarize pyramidal cells along their entire somatodendritic axis. *Nature Neuroscience* **12**, 21–23.

Glykys J, Dzhala V, Egawa K & Balena T (2014). Local impermeant anions establish the neuronal chloride concentration. *Science* pp. 670–676.

Glykys J, Dzhala V, Egawa K, Kahle KT, Delpire E & Staley K (2017). Chloride Dysregulation, Seizures, and Cerebral Edema: A Relationship with Therapeutic Potential. *Trends in Neurosciences* **40**, 276–294.

Goldman DE (1943). Potential, Impedance, and Rectification in Membranes. *J. Gen. Physiol.* **27**, 37–60.

Gray DJ & Wu SMS (1997). *Foundations of Cellular Neurophysiology*. MIT Press, Cambridge, Massachussets, 3<sup>rd</sup> edition.

Hamada K, Matsuura H, Sanada M, Toyoda F, Omatsu-Kanbe M, Kashiwagi A & Yasuda H (2003). Properties of the Na<sup>+</sup>/K<sup>+</sup> pump current in small neurons from adult rat dorsal root ganglia. *British Journal of Pharmacology* **138**, 1517–1527.

Hernández Ja & Cristina E (1998). Modeling cell volume regulation in nonexcitable cells: the roles of the Na<sup>+</sup> pump and of cotransport systems. *American Journal of Physiology - Cell Physiology* **275**, C1067–C1080.

- Hewitt Sa, Wamsteeker JI, Kurz EU & Bains JS (2009). Altered chloride homeostasis removes synaptic inhibitory constraint of the stress axis. *Nat. Neurosci.* **12**, 438–43.
- Hill T (1956). A. Fundamental studies. On the theory of the Donnan membrane equilibrium. *Discussions of the Faraday Society*.
- Hille B (2001). Ion Channels of Excitable Membranes.
- Hodgkin A & Katz B (1949). The effect of sodium ions on the electrical activity of the giant axon of the squid. *J. Physiol.* **108**, 37–77.
- Hyde TM, Lipska BK, Ali T, Mathew SV, Law AJ, Metitiri OE, Straub RE, Ye T, Colantuoni C, Herman MM, Bigelow LB, Weinberger DR & Kleinman JE (2011). Expression of GABA signaling molecules KCC2, NKCC1, and GAD1 in cortical development and schizophrenia. *J. Neurosci.* **31**, 11088–95.
- Jedlicka P, Deller T, Gutkin BS & Backus KH (2011). Activity-dependent intracellular chloride accumulation and diffusion controls GABA<sub>A</sub> receptor-mediated synaptic transmission. *Hippocampus* **21**, 885–98.
- Jiang C & Haddad GG (1991). Effect of anoxia on intracellular and extracellular potassium activity in hypoglossal neurons in vitro. *Journal of neurophysiology* **66**, 103–111.
- Kager H, Wadman WJ & Somjen GG (2000). Simulated Seizures and Spreading Depression in a Neuron Model Incorporating Interstitial Space and Ion Concentrations. *Journal of Neurophysiology* **84**, 495–512.
- Kager H, Wadman WJ & Somjen GG (2007). Seizure-like afterdischarges simulated in a model neuron. *Journal of Computational Neuroscience* **22**, 105–128.
- Kaila K, Lamsa K, Smirnov S, Taira T & Voipio J (1997). Long-lasting GABA-mediated depolarization evoked by high-frequency stimulation in pyramidal neurons of rat hippocampal slice is attributable to a network-driven, bicarbonate-dependent K<sup>+</sup> transient. *J. Neurosci.* **17**, 7662–7672.
- Kaila K (1994). Ionic basis of GABA<sub>A</sub> receptor channel function in the nervous system. *Prog. Neurobiol.* **42**, 489–537.
- Kaila K, Price TJ, Payne Ja, Puskarjov M & Voipio J (2014). Cation-chloride cotransporters in neuronal development, plasticity and disease. *Nat. Rev. Neurosci.* **15**, 637–654.
- Kay AR (2017). How Cells Can Control Their Size by Pumping Ions. *Frontiers in Cell and Developmental Biology* **5**, 1–14.
- Keener J & Sneyd J (2009). *Mathematical Physiology: Systems Physiology* Vol. 8/I Springer, New York, 2 edition.
- Klein PM, Lu A, Harper ME, McKown HM, Morgan J & Beenakker MP (2018). Tenuous inhibitory GABAergic signaling in the reticular thalamus. *The Journal of Neuroscience* **38**, 1232–1248.
- Krishnan GP & Bazhenov M (2011). Ionic dynamics mediate spontaneous termination of seizures and postictal depression state. *J. Neurosci.* **31**, 8870–82.
- Krnjević K & Schwartz S (1967). The action of gamma-aminobutyric acid on cortical neurones. *Experimental brain research.* **3**, 320–336.

- Kuner T & Augustine G (2000). A Genetically Encoded Ratiometric Indicator for Chloride: Capturing Chloride Transients in Cultured Hippocampal Neurons. *Neuron* **27**, 447–459.
- Lagostena L, Rosato-Siri M, D’Onofrio M, Brandi R, Arisi I, Capsoni S, Franzot J, Cattaneo A & Cherubini E (2010). In the adult hippocampus, chronic nerve growth factor deprivation shifts GABAergic signaling from the hyperpolarizing to the depolarizing direction. *J. Neurosci.* **30**, 885–93.
- Lee HHC, Deeb TZ, Walker JA, Davies PA & Moss SJ (2011). NMDA receptor activity downregulates KCC2 resulting in depolarizing GABA<sub>A</sub> receptor-mediated currents. *Nature Neuroscience* **14**, 736–743.
- Lei Y, Han H, Yuan F, Javeed A & Zhao Y (2017). The brain interstitial system: Anatomy, modeling, in vivo measurement, and applications. *Progress in Neurobiology* **157**, 230–246.
- Lewin N, Aksay E & Clancy CE (2012). Computational Modeling Reveals Dendritic Origins of GABA<sub>A</sub>-Mediated Excitation in CA1 Pyramidal Neurons. *PLoS One* **7**, 1–17.
- Liang D, Bhatta S, Volodymyr G & Simard JM (2007). Cytotoxic edema : mechanisms of pathological cell swelling. *Neurosurg Focus* **22**, 1–9.
- Lodish H, Berk A, Zipursky SL, Matsudaira P, Baltimore D & Darnell J (2009). Intracellular Ion Environment and Membrane Electric Potential In *Molecular Cell Biology*. New York, 4 edition.
- Luhmann HJ, Kirischuk S & Kilb W (2014). Comment on “Local impermeant anions establish the neuronal chloride concentration”. *Science* **345**, 1130–1130.
- MacAulay N, Hamann S & Zeuthen T (2004). Water transport in the brain: role of cotransporters. *Neuroscience* **129**, 1031–44.
- MacKenzie G & Maguire J (2015). Chronic stress shifts the GABA reversal potential in the hippocampus and increases seizure susceptibility. *Epilepsy Res.* **109**, 13–27.
- Mahadevan V, Dargaei Z, Ivakine EA, Hartmann AM, Ng D, Chevrier J, Ormond J, Nothwang HG, McInnes RR & Woodin MA (2015). Neto2-null mice have impaired GABAergic inhibition and are susceptible to seizures. *Frontiers in Cellular Neuroscience* **9**.
- McDougal RA, Morse TM, Carnevale T, Marenco L, Wang R, Migliore M, Miller PL, Shepherd GM & Hines ML (2017). Twenty years of ModelDB and beyond: building essential modeling tools for the future of neuroscience.
- Menon V, Spruston N & Kath WL (2009). A state-mutating genetic algorithm to design ion-channel models. *Proceedings of the National Academy of Sciences* **106**, 16829–16834.
- Miocinovic S, Parent M, Butson CR, Hahn PJ, Russo GS, Vitek JL & McIntyre CC (2006). Computational Analysis of Subthalamic Nucleus and Lenticular Fasciculus Activation During Therapeutic Deep Brain Stimulation. *Journal of Neurophysiology* **96**, 1569–1580.
- Misgeld U, Deisz RA, Dodt HU & Lux HD (1985). The Role of Chloride Transport in Postsynaptic Inhibition of Hippocampal Neurons. *Science* **1821**, 12–14.
- Mohapatra N, Tønnesen J, Vlachos A, Kuner T, Deller T, Nägerl UV, Santamaria F & Jedlicka P (2016). Spines slow down dendritic chloride diffusion and affect short-term ionic plasticity of GABAergic inhibition. *Scientific Reports* **6**, 23196.

Nichol JA & Hutter F (1996). Tensile strength and dilatational elasticity of giant sarcolemmal vesicles shed from rabbit muscle. *Journal of Physiology* **493**, 187–198.

Pallud J, Le Van Quyen M, Bielle F, Pellegrino C, Varlet P, Labussiere M, Cresto N, Dieme MJ, Baulac M, Duyckaerts C, Kourdougli N, Chazal G, Devaux B, Rivera C, Miles R, Capelle L & Huberfeld G (2014). Cortical GABAergic excitation contributes to epileptic activities around human glioma. *Sci. Transl. Med.* **6**, 244ra89.

Pathak HR, Weissinger F, Terunuma M, Carlson GC, Hsu FC, Moss SJ & Coulter DA (2007). Disrupted Dentate Granule Cell Chloride Regulation Enhances Synaptic Excitability during Development of Temporal Lobe Epilepsy. *Journal of Neuroscience* **27**, 14012–14022.

Payne JA (1997). Functional characterization of the neuronal-specific K-Cl cotransporter: implications for  $[K^+]$ <sub>o</sub> regulation. *Am J Physiol* **273**, C1516–C1525.

Pellegrino C, Gubkina O, Schaefer M, Becq H, Ludwig A, Mukhtarov M, Chudotvorova I, Corby S, Salyha Y, Salozhin S, Bregestovski P & Medina I (2011). Knocking down of the KCC2 in rat hippocampal neurons increases intracellular chloride concentration and compromises neuronal survival. *J. Physiol.* **589**, 2475–96.

Perkins KL (1999). Cl<sup>-</sup> accumulation does not account for the depolarizing phase of the synaptic GABA response in hippocampal pyramidal cells. *J. Neurophysiol.* **82**, 768–777.

Pfeffer CK, Stein V, Keating DJ, Maier H, Rinke I, Rudhard Y, Hentschke M, Rune GM, Jentsch TJ & Hubner Ca (2009). NKCC1-Dependent GABAergic Excitation Drives Synaptic Network Maturation during Early Hippocampal Development. *J. Neurosci.* **29**, 3419–3430.

Podlaski WF, Seeholzer A, Groschner LN, Miesenböck G, Ranjan R & Vogels TP (2017). Mapping the function of neuronal ion channels in model and experiment. *eLife* **6**.

Price TJ, Cervero F, Gold MS, Hammond DL & Prescott Sa (2009). Chloride regulation in the pain pathway. *Brain Res. Rev.* **60**, 149–70.

Qian N & Sejnowski TJ (1989). An Electro-Diffusion Model for Computing Membrane Potentials and Ionic Concentrations in Branching Dendrites, Spines and Axons. *Biological Cybernetics* **62**, 1–15.

Qian N & Sejnowski TJ (1990). When is an inhibitory synapse effective? *Proceedings of the National Academy of Sciences of the United States of America* **87**, 8145–8149.

Quadroni R & Knöpfel T (1994). Compartmental models of type A and type B guinea pig medial vestibular neurons. *Journal of neurophysiology* **72**, 1911–24.

Raimondo JV, Burman RJ, Katz AA & Akerman CJ (2015). Ion dynamics during seizures. *Frontiers in Cellular Neuroscience* **9**, 1–14.

Raimondo JV, Kay L, Ellender TJ & Akerman CJ (2012). Optogenetic silencing strategies differ in their effects on inhibitory synaptic transmission. *Nat. Neurosci.* **15**, 1102–4.

Raimondo JV, Richards BA & Woodin MA (2017). Neuronal chloride and excitability — the big impact of small changes. *Current Opinion in Neurobiology* **43**, 35–42.

- Rivera C, Li H, Thomas-Crusells J, Lahtinen H, Viitanen T, Nanobashvili A, Kokaia Z, Airaksinen MS, Voipio J, Kaila K & Saarma M (2002). BDNF-induced TrkB activation down-regulates the  $K^+-Cl^-$  cotransporter KCC2 and impairs neuronal  $Cl^-$  extrusion. *J. Cell Biol.* **159**, 747–52.
- Rivera C, Voipio J, Payne JA, Ruusuvuori E, Lahtinen H, Lamsa K, Pirvola U, Saarma M & Kaila K (1999). The  $K^+/Cl^-$  co-transporter KCC2 renders GABA hyperpolarizing during neuronal maturation. *Nature* **397**, 251–255.
- Rungra RL, Choi HB, Tyson JR, Malik A, Dissing-Olesen L, Lin PJC, Cain SM, Cullis PR, Snutch TP & Macvicar BA (2015). The cellular mechanisms of neuronal swelling underlying cytotoxic edema. *Cell* **161**, 610–621.
- Sachs F & Sivaselvan MV (2015). Cell volume control in three dimensions: Water movement without solute movement. *The Journal of General Physiology* **145**, 373–380.
- Savtchenko LP, Poo MM & Rusakov DA (2017). Electrodiffusion phenomena in neuroscience: a neglected companion. *Nature Publishing Group* **18**, 598–612.
- Somjen GG, Kager H & Wadman WJ (2008). Computer simulations of neuron-glia interactions mediated by ion flux. *Journal of Computational Neuroscience* **25**, 349–365.
- Sperelakis N (2012). Chapter 10 — Gibbs-Donnan Equilibrium Potentials. In *Cell Physiology Source Book*, pp. 147–151.
- Staley KJ, Brandi L Soldo & Proctor WR (1995). Ionic Mechanisms of Neuronal Excitation by Inhibitory GABA<sub>A</sub> Receptors. *Science* **269**, 977–981.
- Staley KJ & Mody I (1992). Shunting of Excitatory Input to Dentate Gym Granule Cells by a Depolarizing GABA<sub>A</sub> Receptor-Mediated Postsynaptic Conductance. *J. Neurophysiol.* **68**, 197–212.
- Staley K & Proctor W (1999). Modulation of mammalian dendritic GABA<sub>A</sub> receptor function by the kinetics of Cl and HCO<sub>3</sub> transport. *J. Physiol.* **519**, 693–712.
- Steffensen AB, Oernbo EK, Stoica A, Gerkau NJ, Barbuskaite D, Tritsaris K, Rose CR & MacAulay N (2018). Cotransporter-mediated water transport underlying cerebrospinal fluid formation. *Nature Communications* **9**, 2167.
- Stein V, Hermans-Borgmeyer I, Jentsch TJ & Hbner Ca (2004). Expression of the KCl cotransporter KCC2 parallels neuronal maturation and the emergence of low intracellular chloride. *J. Comp. Neurol.* **468**, 57–64.
- Szabadics J, Varga C, Molnár G, Oláh S, Barzó P & Tamás G (2006). Excitatory effect of GABAergic axo-axonic cells in cortical microcircuits. *Science* **311**, 233–235.
- Tang D, Qian AH, Song DD, Ben QW, Yao WY, Sun J, Li WG, Xu TL & Yuan YZ (2015). Role of the potassium chloride cotransporter isoform 2-mediated spinal chloride homeostasis in a rat model of visceral hypersensitivity. *Am. J. Physiol. Gastrointest. Liver Physiol.* **308**, G767–78.
- Thompson SM & Gähwiler BH (1989). Activity-dependent disinhibition. II. Effects of extracellular potassium, furosemide, and membrane potential on  $E_{Cl}$  in hippocampal CA3 neurons. *Journal of neurophysiology* **61**, 512–23.

- Thompson SM, Deisz RA & Prince DA (1988). Relative Contributions of Passive Equilibrium and Active Transport to the Distribution of Chloride in Mammalian Cortical Neurons. *J. Neurophysiol.* **60**, 105–124.
- Tosteson D & Hoffman J (1960). Regulation of cell volume by active cation transport in high and low potassium sheep red cells. *The Journal of general physiology*.
- Tyzio R, Nardou R & Ferrari D (2014). Oxytocin-mediated GABA inhibition during delivery attenuates autism pathogenesis in rodent offspring. *Science* **343**, 675–680.
- Tyzio R, Minlebaev M, Rheims S, Ivanov A, Jorquera I, Holmes GL, Zilberter Y, Ben-Ari Y & Khazipov R (2008). Postnatal changes in somatic gamma-aminobutyric acid signalling in the rat hippocampus. *Eur. J. Neurosci.* **27**, 2515–28.
- Uvarov P, Ludwig a, Markkanen M, Rivera C & Airaksinen MS (2006). Upregulation of the Neuron-Specific K<sup>+</sup>/Cl<sup>-</sup> Cotransporter Expression by Transcription Factor Early Growth Response 4. *J. Neurosci.* **26**, 13463–13473.
- Valeeva G, Tressard T, Mukhtarov M, Baude A & Khazipov R (2016). An Optogenetic Approach for Investigation of Excitatory and Inhibitory Network GABA Actions in Mice Expressing Channelrhodopsin-2 in GABAergic Neurons. *The Journal of neuroscience : the official journal of the Society for Neuroscience* **36**, 5961–73.
- Voipio J, Boron WF, Jones SW, Hopfer U, Payne Ja & Kaila K (2014). Comment on “Local impermeant anions establish the neuronal chloride concentration”. *Science* **345**, 1130.
- Wake H, Watanabe M, Moorhouse AJ, Kanematsu T, Horibe S, Matsukawa N, Asai K, Ojika K, Hirata M & Nabekura J (2007). Early changes in KCC2 phosphorylation in response to neuronal stress result in functional downregulation. *J. Neurosci.* **27**, 1642–50.
- Werman R, Davidoff RA & Aprison MH (1968). Inhibitory of glycine on spinal neurons in the cat. *Journal of Neurophysiology* **31**, 81–95.
- Williams JR, Sharp JW, Kumari VG, Wilson M & Payne JA (1999). The Neuron-specific K-Cl Cotransporter, KCC2: Antibody Development and Initial Characterization of the Protein. *J. Biol. Chem.* **274**, 12656–12664.
- Woodruff A, Xu Q, Anderson SA & Yuste R (2009). Depolarizing effect of neocortical chandelier neurons. *Frontiers in Neural Circuits* **3**, 15.
- Wright R, Newey SE, Ilie A, Wefelmeyer W, Raimondo JV, Ginham R, McIlhinney RJ & Akerman CJ (2017). Neuronal Chloride Regulation via KCC2 Is Modulated through a GABA<sub>B</sub> Receptor Protein Complex. *The Journal of Neuroscience* **37**, 5447–5462.
- Xiao A, Wei L, Xia S, Rothman S & Yu S (2002). Ionic mechanisms of ouabain-induced concurrent apoptosis and necrosis in individual cultured cortical neurons. *The Journal of Neuroscience* **15**, 4.
- Yeh BK & Lazzara R (1973). Reversal of Ouabain-Induced Electrophysiological Effects by Potassium Canrenoate in Canine Purkinje Fibers. *Circulation Research* **32**, 501–508.
- Zhang RW, Zhang SY & Du JL (2013). KCC2-dependent subcellular E<sub>Cl</sub> difference of ON-OFF retinal ganglion cells in larval zebrafish. *Frontiers in Neural Circuits* **7**, 103.